The Relation of Carbon Influxes and Core Carbon Concentrations in ASDEX Upgrade

Si-Woo Yoon

Max-Planck-Institut für Plasmaphysik
Experimentelle Plasmaphysik 4

The Relation of Carbon Influxes and Core Carbon Concentrations in ASDEX Upgrade

Si-Woo Yoon

Vollständiger Abdruck der von der Fakultät für Physik
der Technischen Universität München
zur Erlangung des akademischen Grades eines
Doktors der Naturwissenschaften (Dr.rer.nat.)
genehmigten Dissertation.

Vorsitzender: Univ.-Prof. Dr. P. Vogel

Prüfer der Dissertation: 1. Hon.-Prof. Dr. R. Wilhelm

2. Univ.-Prof. Dr. E. Nolte

Die Dissertation wurde am 26.6.2003 bei der
Technischen Universität München eingereicht und
durch die Fakultät für Physik am 16.9.2003 angenommen.

Abstract

Understanding the impurity behavior in a tokamak plasma is one of the major tasks on the route to the successful development of a fusion reactor. Carbon is the major impurity species in present tokamak plasmas including ASDEX Upgrade, since major parts of the first wall are covered with graphite. Carbon transport can be divided into three parts: the sources from the plasma wall interactions, the transport in the plasma edge region, and the core transport. In this thesis, the relation of carbon influxes to the core carbon concentrations is studied in ASDEX Upgrade plasma discharges.

Optical emission spectroscopy is used for the measurements of the carbon influxes, in addition to the deuterium influxes. The proportional constant between influxes and the photon intensities, i.e, the inverse photon efficiency, are derived from the collisional-radiative modeling (ADAS). The core carbon concentrations are calculated from the soft-X ray measurements of CVI with the assumption of coronal equilibrium. The two-dimensional plasma edge simulation code (B2.5) is utilized to interpret the spectroscopic measurements. A fit routine of B2.5 is developed to determine the transport coefficients at the outer midplane of ASDEX Upgrade, which are required for a self-consistent description of the edge plasma.

Based on the finding of this thesis, the carbon sources from the divertors are negligible to the main chamber source. This is concluded from both the analytic and the computational calculations and also from the experimental database of the standard H-modes in ASDEX Upgrade. Although the inner heat shield are tungsten coated, according to the radial magnetic scan experiments and Zeeman analysis, the carbon sources from the inner heat shield are dominant. The transport coefficients at the plasma boundary region are determined using the B2.5 fit routine. For carbon ions, an inward pinch is required to match the measurements. Finally, the effect of the edge localized mode on influxes is discussed.

Acknowledgements

I am indebted to my scientific advisor, Prof. Dr. Arne Kallenbach for his scientific guidance. He has enlightened me via valuable discussions and brilliant suggestions. If my thesis is something readable, it's mainly due to his patience and support throughout my graduate course.

I would like to thank my academic advisor, Prof. Dr. Rolf Wilhelm for his kindness to correct my thesis. I am grateful to Prof. Dr. K. Behringer for providing opportunity to work with the ASDEX Upgrade team.

I am also grateful to Dr. David Coster and Dr. Jeong Won Kim for their support and guidance for B2 code and the physics inside. I thank my colleague Dr. Roberto Pugno and Mr. Tomas Pütterich for their support and advice about the experimental works. I would like to thank Dr. Rudolf Neu, Dr. Ralf Dux, Dr. Hans Meister, Dr. Alex Geier for their useful discussions and suggestions. I thank Dr. Jürgen Gafert for his support for the Zeeman analysis. The special thank is to Frau. Gabriele Daube who helped everything about living in Garching.

Finally, I would like to express thanks to my family with all my heart, my son Dong-Hyun and my wife Sung-Hye who support me with endless love all the time, especially for my wife.

Contents

1

Introduction

1.1 Thermonuclear Fusion

The development of alternative energy resources is a high priority task for the present generation since the conventional energy sources, such as fossil fuels, nuclear fission, etc, are being depleted rapidly and also have negative effects on the environment and safety. Several renewable energy sources, for example, solar, wind, geothermal, etc have been proposed and are under intensive research investigation but their potentials are quite limited[1, 2]. It has therefore become a critical issue to develop a new abundant energy source which is safe, durable and environment-friendly. Nuclear fusion is a possible contender in this respect. Since the 1950s, extensive investigations on the nuclear fusion process as an alternative energy source have been devoted to this goal[3]. The most feasible fusion reaction, due to its highest fusion reaction rate, is the deuterium-tritium reaction in which the mass deficit between the reactants and the reaction products is transformed to the kinetic energy of the reaction products based on Einstein's mass-energy relation[3].

$$ {}_1^2D + {}_1^3T \rightarrow {}_0^1n(14.1MeV) + {}_2^4He(3.5MeV) \tag{1.1} $$

Due to the strong repulsive Coulomb barrier which prevents the fusion reaction, a high impact energy of the reactants is a prerequisite for high fusion rates and several methods have been proposed to this end. One approach is heating and sustaining a ionized gas, known as plasma, to high temperatures, typically above 10[keV], in order to overcome the prevailing Coulomb force and achieve the relevant reaction rate required for the reactor level.

1.2 Tokamak : A Toroidal Magnetic Plasma Confinement Device

For sustaining a high temperature plasma, research on the plasma confinement is a central issue and several approaches have been proposed. One of the most feasible is magnetic confinement. In this case, charged particles in an external magnetic field follow a helical gyro-orbit along the magnetic field line and therefore their orbits are confined to the field lines within an order of gyro-radius. Due to this characteristic, it is possible to confine the charged particles effectively in a closed magnetic field configuration. Tokamaks[1] and stellarators, as shown in fig 1.1, are the most common toroidal devices with helical magnetic fields, which are essential for the confinement property of a plasma[4].

As shown in fig 1.2, the toroidal magnetic field is inherently subject to the particle loss due to the radial drift ($v_{E\times B}$)[5], which is caused by the polarization from the toroidal magnetic geometry ($v^D_{e,i}$). $v^D_{e,i}$ is generated due to the curvature and the gradient of the magnetic field which are inevitable in toroidal magnetic configurations.

A simple way to avoid this radial drift is to introduce the poloidal component of the magnetic field, which results in the helical magnetic configuration. This poloidal field will short-circuit the upper and lower regions of the torus. The tokamak and stellarator differ in generating the closed helical magnetic field. This is shown in fig 1.1. In the case of the tokamak, the poloidal component of the magnetic field is generated by the toroidal electric current which is induced by a central solenoidal transformer or another non-inductive current drive method. One the other hand, in the case of the stellarator, the poloidal magnetic field is generated by a complicate winding of the external coils. The main advantage of a stellerator are the intrinsic capability to sustain steady-state plasma and the absence of a number of instabilities related to the plasma current in a tokamak[4]. However, the plasma parameter range so far demonstrated in stellerators is further away from reactor conditions compared to tokamaks. But the tokamak has been preferred so far mainly due to the simple coil geometry and its toroidal symmetric configuration. Several schemes for additional plasma heating methods have been developed including the ohmic dissipation of the toroidal plasma current. The high energy neutral beam injections and the external wave coupling are the most common high power heating techniques[3].

The plasma confinement by a magnetic field is not perfect due to the large radial transport processes which are mainly driven by micro-turbulence[6, 7] in the plasma. The radial transport leads to the high particle and heat loads to the surrounding materials and impurities can be introduced to the confined plasma. On the other hand, the presence of impurities in the core plasma leads to a decrease in the fusion

[1]The name "tokamak" consists of the first syllables of the Russian words: toroid, kamera(chamber), magnit(magnet), plus the first letter of the word katushka(coil)

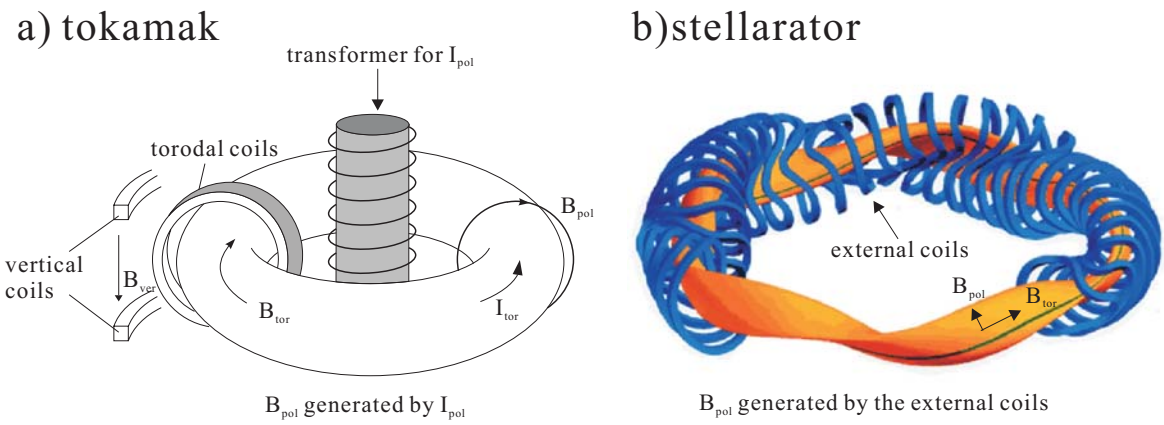

Figure 1.1: *The magnetic configurations of the tokamak(a) and stellarator(b)*

rate through decreasing plasma temperature and fuel dilution. Among the critical issues in realizing a reactor relevant tokamak, impurity control has been one of the most outstanding tasks to obtain a good global performance.

1.3 Divertors and Impurities

Energy and particle fluxes at the plasma boundary flow predominantly along open magnetic field lines slightly outside the last closed flux surface and are concentrated on wall components which can withstand such high power density. However, the confinement of plasma from the surrounding material is not perfect due to the transport processes which are dominated by micro-turbulence[6, 8] in the plasma causing energy and particle fluxes to radially reach the material surfaces. This can lead to degradation of the plasma facing components (PFCs) reducing their lifetime due to the plasma exposure and to impurity generation due to the various plasma-wall interactions, such as sputtering, arcing and evaporation. These impurities can penetrate efficiently into the confined plasma and thereby contaminate it. In present tokamaks, the limiter and divertor configurations, as shown in fig 1.3, are widely used magnetic configurations to localize and reduce these interactions.

Impurity control has been one of the key issues of tokamak operation because of its harmful effects on energy confinement such as the power losses from the impurity radiation in the confined plasma and the dilution of fusion reactants[9], in addition to the tritium co-deposition problem on the PFCs via hydrocarbon formations. Although impurity concentrations in tokamak plasmas have been strongly reduced by introduction of the divertor concept and wall conditioning, the stringent limits of the central impurity concentrations imposed by the optimized performance of a fusion device still require systematic efforts to understand and control the global impurity behavior.

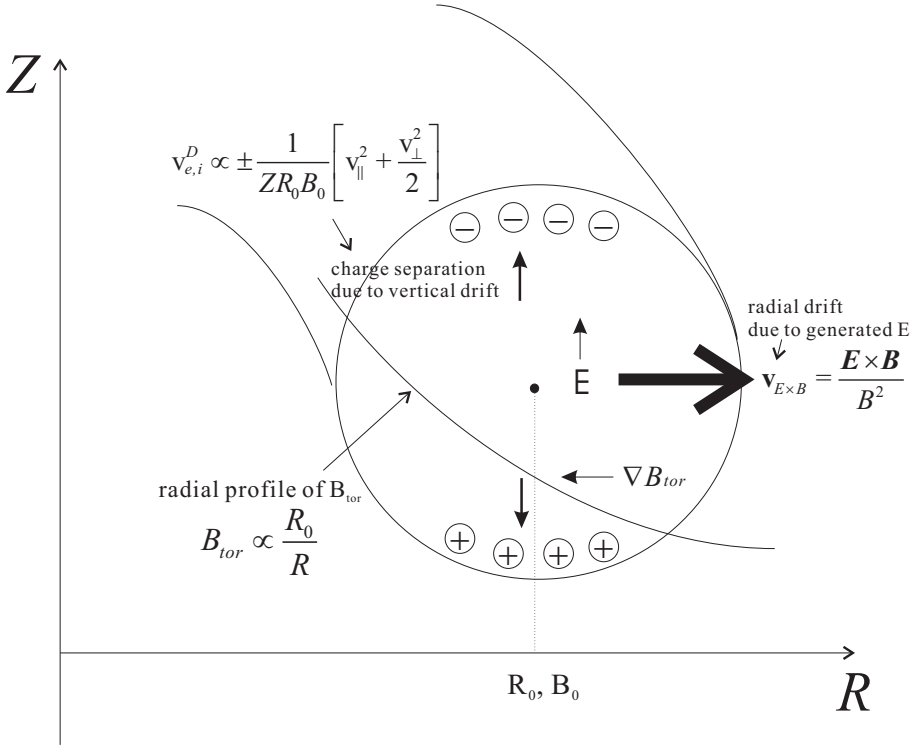

Figure 1.2: *The inherent radial drift ($v_{E\times B}$) due to the charge separation resulting from the toroidal drift ($v^D_{e,i}$). A poloidal magnetic field is necessary to prevent it by mixing the unfavorable charge separation poloidally.*

Among the major impurity species, carbon is the dominant and ubiquitous one in present tokamaks. This is mainly due to the extensive usage of graphite and carbon fiber composite (CFC), which have relatively good thermo-mechanical properties, as the plasma facing components. Besides, due to their high radiative potential at low electron temperature around 10 [eV], carbon ions are a very effective tool for the mitigation of excessive power loads on the divertor plates through the radiative cooling at the plasma boundary[10]. However, its further use as a wall material in reactor relevant tokamaks is questionable due to the relatively high chemical erosion rates and hence the short component lifetime. In addition, the co-deposition of tritium at the vessel via the formation of hydrocarbon layers[11] is a critical safety issue to be considered in deuterium-tritium fusion reactors. Although strong efforts have been devoted to understand the carbon behavior in tokamak plasmas, a quantitative description has not yet been available due to diagnostic limits, the complex pattern of carbon transport in the Scrape-Off Layer (SOL) and the subtle erosion mechanisms. Carbon is foreseen to be used in ITER[12] at the locations of the strike zones in the divertors, where the highest power flux densities are expected. Therefore, it is an important question to

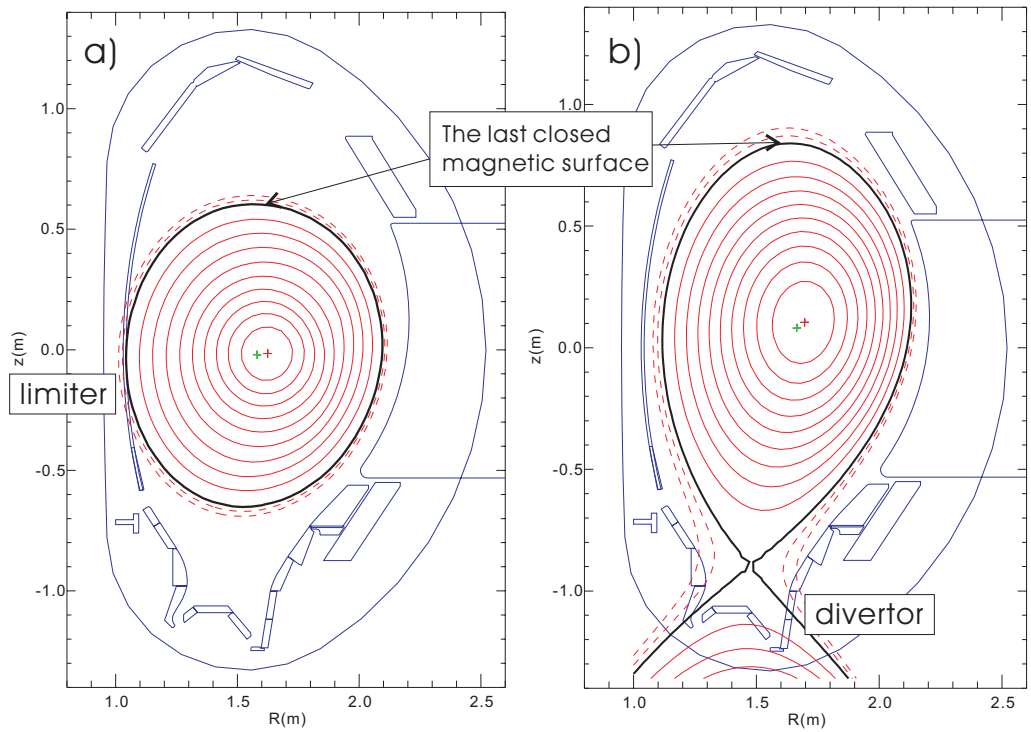

Figure 1.3: *The limiter(a) and the lower single null divertor(b) magnetic surface configurations in ASDEX Upgrade. The last closed magnetic surfaces are shown in bold line, which are defined for the limiter configuration by the contact of flux surface on the wall structure and by the magnetic null generated by external current. The scrape-off layer (SOL) regions, where the magnetic surfaces are drawn in dashed lines, are with open magnetic field lines. The region with the solid lines are the confined core plasma regions in a closed magnetic field configuration. The limiter configuration is used during plasma start-up and ramp down, while the high power flattop phases are in divertor geometry.*

understand the possible path for divertor carbon into the core plasma. This question is not easily answered in the present day machines, where carbon sources are present in the main chamber as well.

1.4 Previous Work and Motivation

Extensive research has been devoted to understand the impurity behavior in tokamak plasmas. The subject can be divided into three parts: impurity generation from the plasma surface interactions (such as erosion, arcing, evaporation), the transport in plasma boundary, perpendicular and parallel to the magnetic field, and the impurity transport in the plasma core region. According to the previous work on impurity transport in the core plasma[13, 14, 15], the impurity transport in this region is dependent on the neoclassical inward drift velocity[16] which is driven by a toroidal electric field on trapped particles. With increasing atomic number Z of an impurity species, a rising trend of accumulation in the plasma center is observed for conditions with peaked density profiles and moderate temperature gradients. In case of the low Z impurity species (such as, C, Si, B, etc) the accumulation in this region is negligible compared to the high Z impurities (W, Fe, Ni, etc). Hence, for low Z impurities, the core concentration is largely determined by the edge concentration in a typical discharge scenario. Therefore, this study is focussed on the edge processes which play the dominant role for the global carbon content. The carbon source and edge transport is studied experimentally and numerically.

The research on the impurity generation mechanisms and the influxes has been mainly directed so far on the sputtering yield and the influx measurements in the divertor region, where the plasma material interaction is strongly concentrated. Quantitative analysis of carbon transport in the plasma edge is often limited by several aspects. First, the carbon influxes are usually derived from the measured photon intensities of the specific carbon ions. Due to the nature of the spectroscopic methods, the measured intensities are inherently integrated along a line of sight, in which the plasma parameters, such as electron temperature (T_e) and density (n_e) are non-uniform. Besides, to derive the influxes from the photon intensities, the atomic data, in particular the photon efficiency, is required and it is a strongly sensitive function of T_e and n_e. The photon emission coefficient is also necessary for deriving carbon concentrations from the photon measurements. Therefore it is essential to reasonably know the variations of these parameters along the lines of sight, which is usually not available experimentally due to the limited capability of the diagnostics. Second, the transport of carbon in the plasma edge is quite complicated, which is hardly described in an analytic fashion. It is mainly due to the complex geometry and the various atomic processes (ionization, recombination, charge-exchange processes, etc). Furthermore, the interaction of carbon with background plasmas can important and energy and particle transport of the background plasma alone is also beyond the scope of analytic analysis. To this end, for the quantitative interpretation of spectroscopic data and reasonable prediction of the plasma parameters, a two-dimensional multi-fluid code, B2.5 package, is utilized, with available experimental data as the boundary conditions to the code.

1.5 Scope of This Work

The aim of this work is to gain a better understanding of carbon transport characteristics at the plasma edge region of ASDEX Upgrade[2] and to identify the dominant carbon sources. Due to the complex wall structure and the complicated particle transport in the edge of tokamak plasmas, the following methods are utilized:

- Optical emission spectroscopy[17] for characterizing the influxes of carbon and the background plasma at the main chamber wall and the divertors.
- Soft X-ray spectroscopy and the visible bremsstrahlung measurement for carbon concentrations in the core plasma.
- The two dimensional edge plasma transport code (B2.5) for interpretation of experimental data.

Via the above methods, the relation of carbon concentrations and influxes are analyzed.

In chapter 2, the general mechanism of carbon transport in ASDEX Upgrade is described in three parts. The various carbon generation mechanisms from the plasma surface interactions, such as physical and chemical erosion, will be described first. Then transport of carbon in parallel and perpendicular directions at the scrape-off layer region including divertor retention, and the perpendicular transport inside the separatix will be examined. Finally, the relative importance of these process to the global carbon content will be discussed.

In chapter 3, the spectroscopic (S/XB) methods and the related techniques to measure the carbon influxes and concentrations in ASDEX Upgrade are described in detail and the relevant diagnostics for the other plasma parameters in ASDEX Upgrade, which are essential for reliable simulations, are also described.

In chapter 4, the adaptation of the B2.5 edge plasma code with respect to interpreting spectroscopic data is presented and the development of the fit procedure for the transport coefficients of carbon and the background plasma is introduced.

In chapter 5, the relative effectiveness of the carbon sources at the various locations to enter the core plasma is analyzed from the experimental standard H-mode [3] database at ASDEX Upgrade and the results of combined simulations with spectroscopic data

[2]ASDEX Upgrade is a medium size fusion device. See Appendix C for the major plasma parameters and the technical data.

[3]The H-mode is a high confinement regime of plasma operation due to the formation of a edge transport barrier. The standard H-mode is a typical H-mode discharge which is repeated every operation day in ASDEX Upgrade. In contrast, the L-mode is a low confinement regime without the edge transport barrier.

will be described in detail. The contribution of Edge Localized Mode (ELM) [4]to carbon transport is also discussed utilizing time dependent simulations.

In chapter 6, the results are summarized and some open questions will be discussed. Additional information is given in the appendix.

[4]Edge Localized Mode. ELM is a periodic expulsion of plasma particles and energy from the confinement plasma into the scrape-off layer.

2

General Mechanisms of Carbon Transport in ASDEX Upgrade

Among the major impurity species, carbon is the dominant and ubiquitous impurity species in present tokamaks. A schematic view of the global carbon behavior in ASDEX Upgrade is shown in fig 2.1. The carbon behavior in tokamak plasmas can be largely divided into three subjects, as discussed in the previous chapter :

- the carbon sources and sinks at the plasma facing materials by the various plasma-material interactions, such as erosion and redeposition processes. The major carbon sources in ASDEX Upgrade are the divertor modules, the inner heat shield, and the outer protection limiters.

- transport in the open magnetic field at the plasma boundary region, in the perpendicular and parallel directions to the external magnetic field.

- perpendicular transport in the confined core region (closed magnetic field configuration). When no inward pinch is present, the radial profiles of carbon are flat because there is no carbon source in the core plasma.

In contrast to high Z impurities, the radial core carbon concentration profiles are flat in the operational scenarios with the flat background density profiles which are typical in conventional discharges. In these circumstances, carbon concentrations are determined largely by the edge concentrations (a few centimeter inside the separatix) and this is again determined by the edge transport processes and source strength of carbon. This study is focused on the sources and transport of carbon in this key region.

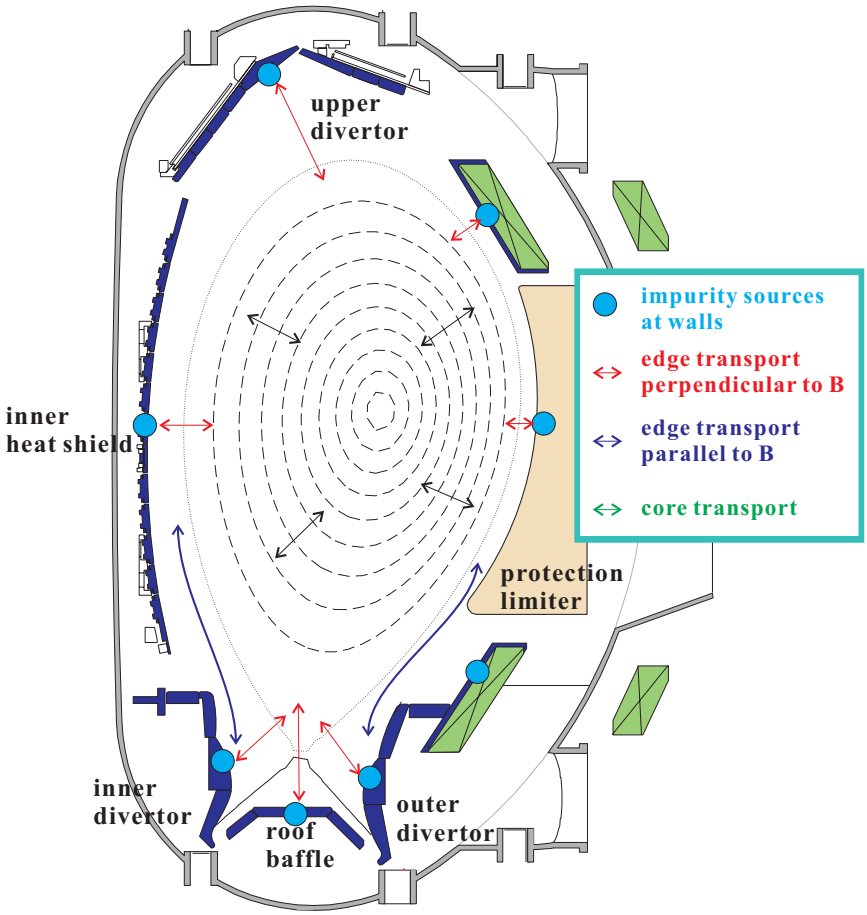

Figure 2.1: *Schematic view of carbon transport in ASDEX Upgrade. The major carbon sources from the surrounding materials and transport patterns are described including the redeposition process from the plasma to the wall and the perpendicular and the parallel transport (bidirectional). Ionization layers are located in the boundary region (open field line), except for highly stripped ionization stages.*

2.1 Release Mechanism of Carbon at the Plasma Facing Components

The main processes of carbon generation in typical discharges in a tokamak are the physical and chemical erosion at the plasma facing components. The major concern about the use of graphite as a plasma facing material is related to the enhanced erosion rate under hydrogen bombardment due to hydrocarbon formation. It has been the common idea that the dominant erosion process is highly localized at the divertor region and thus research has been focused mainly on the erosion measurements in this region. But recently it was also found that although the total carbon influx from the

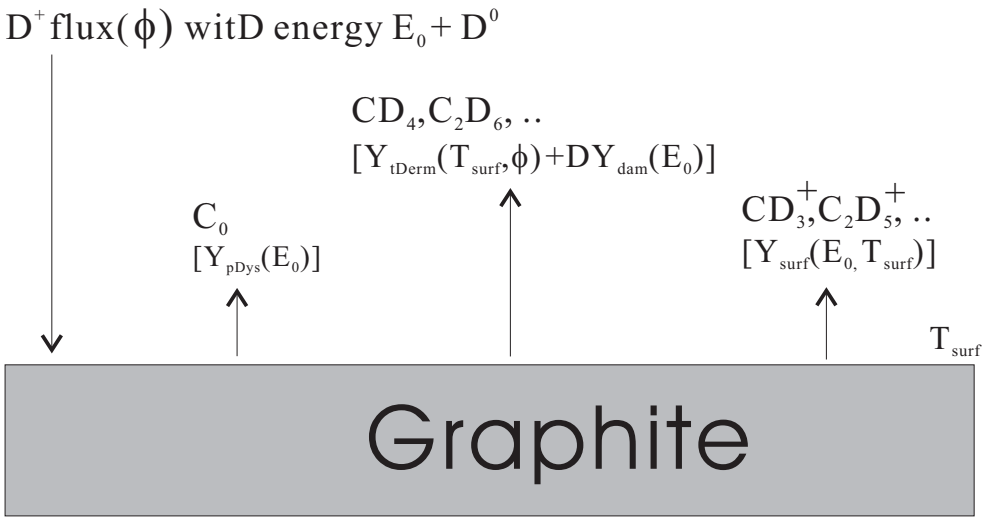

Figure 2.2: *Physical and chemical erosion of carbon from a graphite substrate with the surface temperature T_{surf}. Physical erosion is caused by momentum transfer to the graphite lattice, resulting in the ejection of a surface atom. Chemical erosion takes place via the formation of hydrocarbons, leading finally to the release of various C_xD_y species. This process depends on the flux density of impinging particles.*

main chamber is lower than the carbon influx in the divertors, it can be quite effective to penetrate into the confined plasma due to higher penetration probability. This will be discussed in detail in chapter 5.

As shown schematically in Fig 2.2, the total carbon erosion rate is the combined effect of physical and chemical sputtering. The following formula is given by Roth and coworkers[18, 19].

$$Y_{tot} = Y_{phys} + Y_{therm}(1 + D \cdot Y_{dam}) + Y_{surf} \tag{2.1}$$

where the total erosion yield Y_{tot} is the sum of the physical sputtering Y_{phys} and the chemical sputtering Y_{chem}. The detailed description of the formula will be given in the appendix D. The chemical sputtering part consists of: the reaction of thermalized ions, Y_{therm}, via hydrogenation of the carbon atoms to $CD_3 - C(sp^3)$, enhanced by the radiation damage of the graphite lattice, Y_{dam} (D is a parameter dependent on the bombarding hydrogen isotope) and the ion induced desorption of hydrocarbon radicals on the surface, Y_{surf}. This is illustrated in fig 2.2. According to Roth, the total carbon erosion yield of hydrogen bombardments on pure graphite is dependent on the energy of the incident hydrogen ions (E_0), the incident flux density (Γ_{H^+}), the ion mass and surface temperature (T). At low surface temperature (400K), Y_{surf} is the dominant process for Y_{chem}, while at high T (800K) Y_{therm} is dominant and the total chemical erosion rate increases at the low E_0 part. Typical plasma temperatures

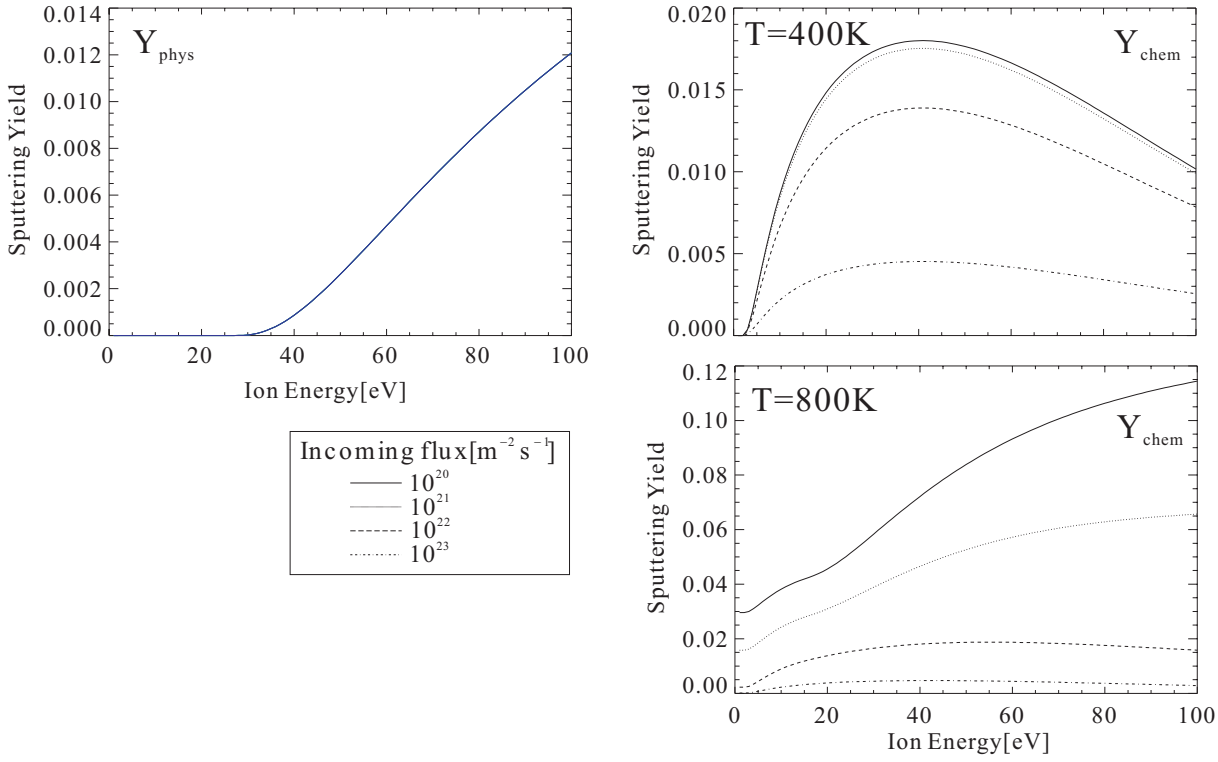

Figure 2.3: *Carbon erosion yields of deuterium ions on graphite substrates calculated from the Roth formula. Surface temperature is 400 K. Maxwellian distributions are assumed for the incident hydrogenic ions. At low surface temperature (400K), Y_{surf} is dominant, while at high T (800K) Y_{therm} is the dominant process for Y_{chem}.*

and the incoming flux density at PFCs in ASDEX Upgrade ranges from 1 to 20 [eV] and from 10^{21} to 10^{23} $[m^{-2}s^{-1}]$ and the variations of the sputtering yields on these parameters are shown in fig 2.3. It is important that in typical edge plasma conditions in ASDEX Upgrade, the ion energy with sheath acceleration[9] at the material surfaces (including the divertor and the protection limiter surfaces) are around 30[eV] which is the threshold of physical erosion[20]. Therefore according to Roth formula 2.1, the chemical erosion will be the dominant process in this plasma parameter range.

The direct application of formula 2.1 to the erosion rates on the plasma facing components in ASDEX Upgrade is questionable for several reasons. First, in case of the typical H-mode[21] discharges, there usually exist quasi-periodic magnetohydrodynamic instabilities, which are called Edge Localized Modes (ELMs) [22, 23]. T_e can be temporarily higher than the threshold of the physical erosion due to the excessive particle and heat loads during an ELM event. In addition, there is the effect of non-maxwellian fast ions on the erosion process during ELMs, which is difficult to quantify. Second, the structure of the carbon surface can be quite different from that of pure

graphite or carbon fiber composite due to successive erosion and re-deposition. Also in the case of ASDEX Upgrade, an increasing fraction of the inner heat shield has been coated with tungsten layers on top of bulk carbon tiles to decrease the global carbon content and to test the compatibility of a tungsten wall with plasma operation[24]. According to carbon influx measurements, the carbon intensities from these tungsten tiles are comparable to those of pure carbon tiles. This strongly suggests the existence of thin carbon layers on top of the tungsten coating caused by deposition. The Roth formula is probably inapplicable to these soft layers.

Therefore, in this study, the carbon source strength at the major plasma facing materials is determined experimentally by optical emission spectroscopy, which is discussed in detail in chapter 3.

2.2 Transport in the Scrape-off Layer Region

Due to the open magnetic field lines, impurity transport at the edge of tokamak plasmas is a complex and at least two-dimensional process, involving transport parallel and perpendicular to the external magnetic field lines and the complicated patterns of ionization and recombination processes. As shown in fig 2.1, carbon neutrals generated from the surface penetrate into the plasma edge, where they are ionized and therefore bound to the magnetic field. Subsequently, the impurity ions undergo collisions with other ions and get entrained by plasma drifts while they are ionized to higher states.

Understanding carbon transport in the SOL region is essential to relate the core carbon concentration with the localized carbon sources at the plasma facing components. In general, the evolution of the impurity density can be described by a continuity equation of the form

$$\frac{\partial n_f}{\partial t} + \nabla \cdot (n_f \mathbf{v}_f) = K^{ion}_{f-1} n_e n_{f-1} - K^{rec}_f n_e n_f \tag{2.2}$$

where f denotes the charge state of an impurity ion species, and n_e is the electron density. $K^{ion,rec}$ are the rate coefficients of ionization and recombination processes. To determine the particle flux (Γ_f), the momentum equation is required and this will be discussed in the next section.

2.2.1 Transport Parallel to the Magnetic Field Line

For the parallel impurity velocity, one can likewise solve a set of momentum conservation equations (in Appendix B) with generalized friction forces. However, a simpler, and often adequate description is to ignore the inertial terms in the impurity parallel momentum equations owing to the dominance of the friction force with the higher-density flowing hydrogen ions.

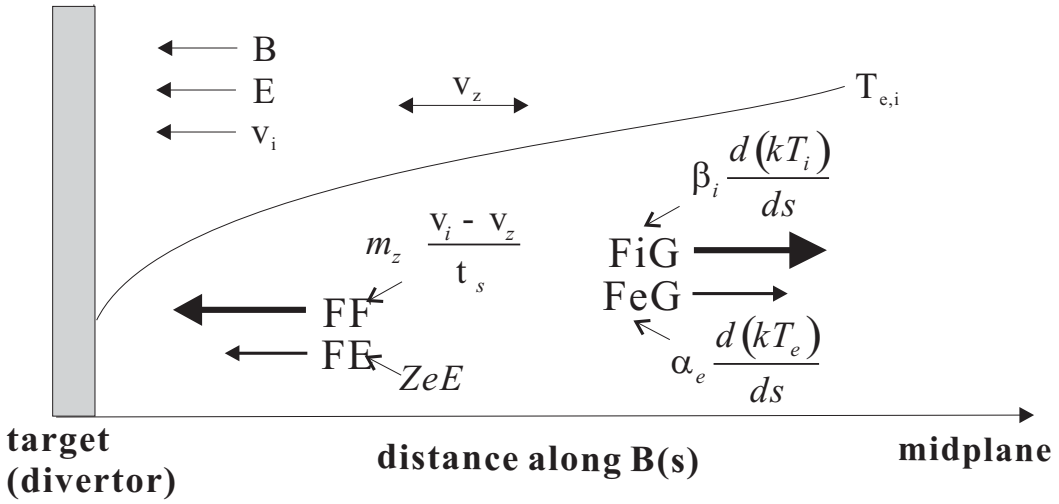

Figure 2.4: *Schematic of impurity transport parallel to the magnetic field. Penetration of impurity from the divertor to the main chamber is determined by parallel force balance mainly between the friction force (FF) and the ion temperature gradient force (FiG).*

$$F_z = -\frac{1}{n_z}\frac{dp_z}{ds} + m_z\left(\frac{v_i - v_z}{\tau_s}\right) + ZeE + \alpha_e\frac{d\left(kT_e\right)}{ds} + \beta_i\frac{d\left(kT_i\right)}{ds} + \sim \tag{2.3}$$

$$\tau_s = \frac{1.47\times10^{13} m_z T_i \left(T_i/m_i\right)^{1/2}}{\left(1+m_i/m_z\right) n_i Z^2 \ln\Lambda} \tag{2.4}$$

$$\alpha_e = 0.71Z^2 \tag{2.5}$$

$$\beta_i = \frac{3\left(\mu + 5\sqrt{2}Z^2\left(1.1\mu^{5/2} - 0.35\mu^{3/2}\right) - 1\right)}{2.6 - 2\mu + 5.4\mu^2} \tag{2.6}$$

where s is the distance measured in the parallel direction to the magnetic field from the divertor plate in the upper stream direction and the subscript i, z denote the background ion species and the impurity species with the charge state Z. The first term on the right hand side is the usual impurity pressure gradient force (FPG) and the second is the friction force (FF) on the impurity ions moving with fluid parallel velocity v_z exerted by the background ions moving with v_i where τ_s is the momentum exchange time of the impurity from Coulomb collisions between the impurity and plasma background ions. T_i is the ion temperature and m_i, m_z are the masses of the ion and the impurity species. $ln\Lambda$ is the Coulomb logarithm [3]. The third term is the electrostatic force (FE) exerted by the parallel electric field and the fourth (FeG) and fifth (FiG) are the temperature gradient forces by Coulomb collisions between the impurity, electron and

background ions: the cross-section for momentum transfer decreases strongly with the relative speed of the colliding particles. The coefficients for these forces, α_e and β_i, are given above and $\mu \equiv m_z/(m_z + m_i)$ is the relative mass. The higher order viscosity forces are neglected. In fig 2.4, the relative strength of the each term is shown with the force directions for the typical divertor plasma conditions. The controlling forces are usually the friction force towards the divertor and the ion temperature gradient force towards the upstream region. The electron temperature gradient force is smaller than the ion temperature gradient force partly due to the larger temperature gradient of ions compared to that of electrons, which is caused by the lower parallel thermal conductivity ($\chi_\parallel \propto 1/\sqrt{m}$), and partly due to the higher value of β_i (for $\mu \to 1$, $\beta_i \to 2.6Z^2$) than α_e. The electrostatic force exerted on the impurity species is weaker than the friction force in a typical divertor plasma.

From the force balance of the impurity species, the contribution of the divertor impurity sources to the main chamber, called divertor retention or leakage, and also for core plasma can be estimated. More generally, transport simulation codes can include the full parallel momentum equations for each charge state, including inertia, viscosity, and the impurity-impurity friction terms.

To assess the contribution of the divertor carbon sources to the core concentration, the divertor leakage is a main issue. The divertor leakage rate of carbon ions can be estimated analytically with the above one-dimensional parallel transport model along a flux surface, considering the force balance between the friction force and the ion temperature gradient force which are dominant factors in the force balance equation of impurities[9]. The carbon neutrals, including hydrocarbons from the divertors are neglected due to their relatively short ionization mean-free-path and therefore only ion transport is considered. Integrating equation 2.3 along a parallel magnetic field line, the following relation between the main chamber carbon flux and the divertor carbon flux can be derived.

$$\frac{\Gamma_\parallel^{main}}{\Gamma_\parallel^{div}} = \frac{2}{7}\beta_i \left(\frac{T_{main}}{T_{div}}\right)^{\frac{7}{2}} \frac{\lambda_{\parallel div}}{L} e^{-\frac{\Delta s}{\lambda_{\parallel div}}} \tag{2.7}$$

$$\lambda_{\parallel div} = 6.8 \times 10^{15} T_{div}^2 / \left(n_{div} Z^2\right) \tag{2.8}$$

where $\Gamma_\parallel^{main}/\Gamma_\parallel^{div}$ is the ratio of the parallel particle fluxes in the divertor and the main chamber, T_{div}, n_{div} and T_{main} are electron temperatures and density at the divertor and the main chamber. $\Delta s = (s_D - s_z)$ is the difference of the ionization fronts between the background plasma and the impurity along the magnetic field. Assuming $B_\theta/B_\phi = 0.1$, s_D along the field line can be approximated as

$$s_D \approx \frac{0.3}{10^{-20} n_e} \tag{2.9}$$

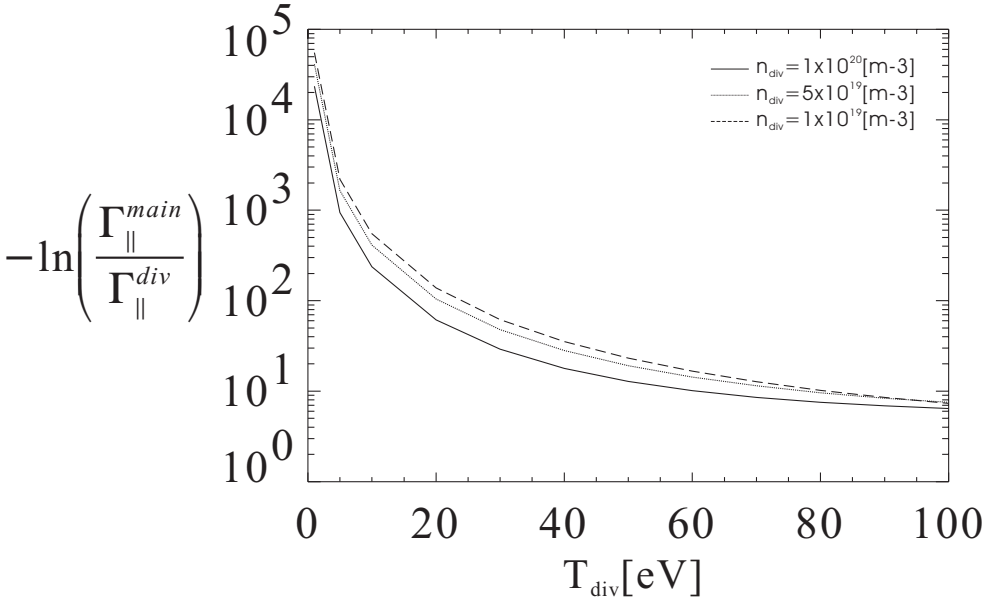

Figure 2.5: *The flux ratio between the divertor and the main chamber as functions of T_{div} and n_{div}). As T_{div} increases, the leakage $\Gamma_{\parallel}^{main}/\Gamma_{\parallel}^{div}$ increases largely due to the increased $\lambda_{\parallel div}$. But leakage level is negligible in this simple estimate.*

from Ref[25] using Monte-Carlo simulations. Z is the charge state of the impurity and $\lambda_{\parallel div}$ is the Roth-Fussmann friction length which is the characteristic decay length of the impurity density in the divertor[26]. Due to the ratio $\frac{\Delta s}{\lambda_{\parallel div}} \gg 1$, the exponential term is the dominant factor for the leakage. In fig 2.5, for a typical condition for ASDEX Upgrade and $C^{4+}(T_{div}[eV] = 1-100, T_{main}[eV] = 100, n_{div} = 1.-10.[m^{-3}] \times 10^{19}, \beta_i \simeq 34, Z = 4, L[m] = 30, s_z[m] = 0.15)$, the flux ratio between the divertor and the main chamber is shown. The dominant factor in the above formula is the exponential term on the right hand side and it is very sensitive on T_{div}. The leakage $(\Gamma_{\parallel}^{main}/\Gamma_{\parallel}^{div})$ is increased as the T_{div} increases due to the reduced collisionality. In this parameter range, the divertor leakage is negligible$(\Gamma_{\parallel}^{main}/\Gamma_{\parallel}^{div} \leq 10^{-8})$.

This implies, according to the above analytic formula, the influx of the divertors is effectively retained in the divertor region due to the strong friction force and the contribution of the divertor sources to the main chamber is negligible. But this is a simple model based on the 1-D parallel transport only, neglecting the radial transport and the toroidal geometry and the complicated ionization patterns. In addition, this model treats ion fuelling only and no direct neutral fuelling to the core plasma is considered. For a better estimate of the divertor retention, full two-dimensional simulations are necessary which will be discussed in chapter 5.

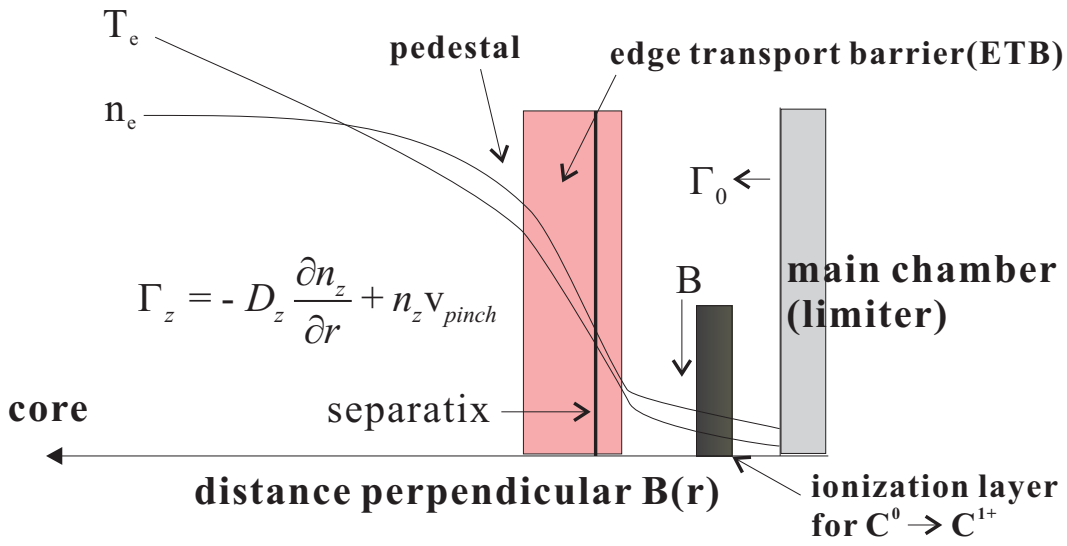

Figure 2.6: *Schematic of the impurity transport perpendicular to the magnetic field, i.e., along the radial direction in the plasma edge region. Penetration of the impurity from the limiter is determined by radial diffusion coefficient (D_z) and inward pinch velocity (v_{pinch}), in addition to the ionization pattern of carbon neutrals generated from the plasma facing components.*

2.2.2 Transport Perpendicular to the Magnetic Field Line

It is essential to understand the radial transport of carbon species for relating the core carbon concentration with the given carbon source strength at the material surfaces. As shown in fig 2.6, the neutrals generated at the material surface can penetrate into the core plasma through diffusion and convection after ionization. Typically, the impurity transport, also for the background plasma, can be described with the fluid radial transport equation described in the previous section assuming the anomalous transport ansatz[27].

$$\Gamma_z = -D_z \frac{\partial n_z}{\partial r} + n_z v_{pinch} \tag{2.10}$$

where Γ_z, D_z, v_{pinch} are particle flux, diffusion coefficient, and anomalous pinch velocity of carbon. In general, the radial impurity density profile are determined mainly by the radial ionization pattern of carbon neutrals and the radial transport coefficients in the scrape-off layer.

In the H-mode case as shown in fig 2.6, it is known that a strong transport barrier exists around the separatix connected to a reduced fluctuation level of the local micro-turbulence[28]. As a consequence, T_e and n_e profiles are quite steep in this region. In the same manner, the core carbon concentration is more or less controlled by the reduced radial transport in this narrow transport barrier. The transport in the plasma

edge is anomalous in a sense that the transport level is larger than the neoclassical level caused by particle collisions in the curved magnetic field geometry. If the enhanced transport is mainly due to the local $E \times B$ drift of the fluctuating fields[8], then it is expected to be independent of mass and charge. Hence, for transport simulations, typically the same transport coefficient is assumed for the impurity and the background plasma. In chap 4, the determination of the radial transport coefficients for H-mode will be described in more detail using a two-dimensional code along with the measurements.

3

Measurements of Carbon Influxes and Concentrations

In this chapter, the principle of the influx measurement a the plasma edge region will be discussed. Also, the experimental setup of the influx measurement will be presented with the additional diagnostics used in this study.

3.1 Principle of Spectroscopic Measurements of the Influxes

The particle flux emerging from a material surface can be calculated from optical emission spectroscopic measurements. From a absolute intensity of a line integrated spectral line, for example CII (426nm), the particle flux of the corresponding species can be derived through the ionization process in this region, as discussed in references[29, 30]. In this chapter, a heuristic derivation of the relation between the particle and photon fluxes will be given. One-dimensional slab geometry is assumed for simplicity. In fig 3.1, a schematic diagram is shown for atomic processes in the case of carbon. When deuterium flux is incident on a wall material, plasma wall interaction processes generate the influx of carbon molecules and atoms (see chap.2). When these neutrals penetrate into the plasma to a certain T_e and n_e, they are ionized to ions and emit line radiation excited by the ambient electrons. When the ratio of the ionization and excitation is known via rate coefficients and a collisional-radiative model, the source of ions can be estimated and thereby the influx of the ions is obtained.

3.1.1 Description of Line Integrated Photon Fluxes

When a specific line emission from the excited state k to m is considered, the photon emissivity (ϵ_{km}) in z ionization stage of the transition from the state k to m is obtained

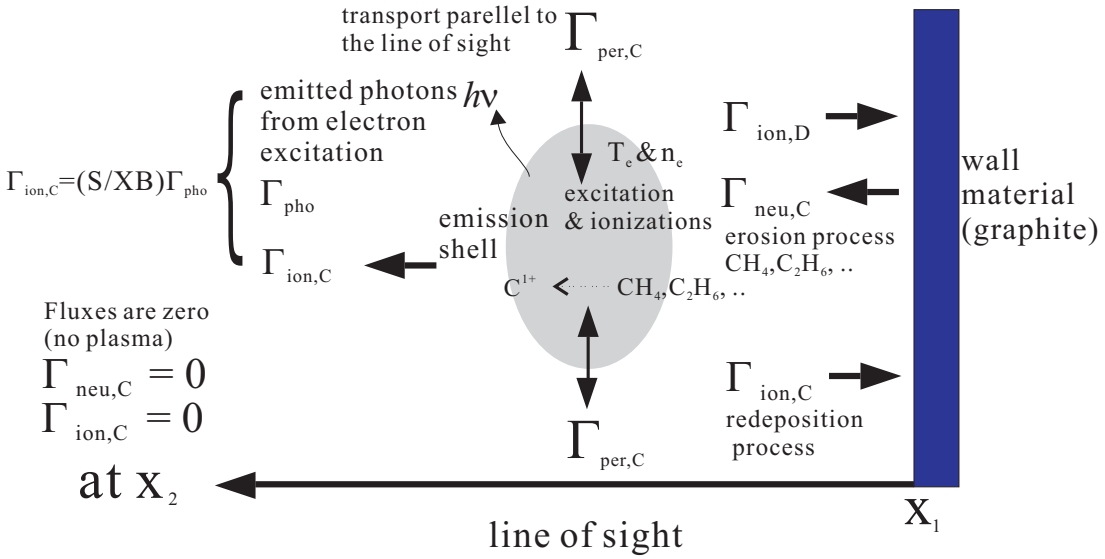

Figure 3.1: *A schematic illustration of the slab geometry for S/XB (inverse photon emissivity) derivation. From the known ratio of ionization ($\Gamma_{ion,C}$) and excitation (Γ_{pho}), $\Gamma_{ion,C}$ is derived from Γ_{pho}. The re-deposition process is also taken into account.*

from the Einstein coefficient A_{km} :

$$\epsilon_{km} \;=\; n_{zk} \cdot A_{km} \tag{3.1}$$

Using the population balance relation and neglecting cascade correction, the emission can be related to the ground state population:

$$n_e \cdot n_z \cdot X_{0k} \;=\; n_{zk} \cdot \sum_i A_{ki} \tag{3.2}$$

where X_{0k} is the excitation rate of the transition from the ground state to k state. In equilibrium, the line integrated emissivity can be expressed from equation 3.3 in terms of the excitation rate and the branching ratio as follows.

$$\Gamma_{pho,km} = \int_{x_1}^{x_2} \varepsilon_{km} dx = \int_{x_1}^{x_2} n_e \cdot n_z \cdot X_{0k} \cdot A_{km} / \textstyle\sum_i A_{ki} dx \tag{3.3}$$

where $\Gamma_{pho,km}$ is the line integrated photon flux. The integration starts from the wall (x_1) and ends at x_2, where the fluxes vanish, as shown fig 3.1. $B_{km} = A_{km} / \sum_i A_{ki}$ is called the branching ratio which corresponds to the fraction of the observed transition (k to m) in the total radiative decay transitions out of the upper level k.

3.1.2 The Relation of Photon and Particle Flux

Particle balance of an ion species in an ionized state can be casted in a conservative form, neglecting the recombination processes, which is a relevant assumption for the low ionization state of impurities in typical plasma edge conditions[31, 32], using the continuity equation.

$$\frac{\partial n_a}{\partial t} + \nabla \cdot (\mathbf{\Gamma}_{a,par}) = -S_a \cdot n_e \cdot n_a + S_{a-1} \cdot n_e \cdot n_{a-1} \tag{3.4}$$

where n_a, $\mathbf{\Gamma}_{a,par} = n_a \cdot \mathbf{v_a}$, S_a are density, particle flux and ionization rate of a ionization state. From this equation, the relation between the particle flux and ionization rate can be derived. In steady-state, summing up equations for the ionization state from 0 to z and integrating along the line of sight leads to,

$$\sum_{a=0}^{z} \int_{x_1}^{x_2} \left(\nabla_{\parallel} \cdot \mathbf{\Gamma}_{a,par} + \nabla_{\perp} \cdot \mathbf{\Gamma}_{a,par} \right) dx = \int_{x_1}^{x_2} \left(-S_z \cdot n_e \cdot n_z \right) dx \tag{3.5}$$

where the divergence is divided into parallel and perpendicular components along the line of sight direction. After the integration, using $\Gamma_{a,par}$ at x_2 =0, and using the definition for the effective particle flux, $\Gamma_{z,net}$ can be formulated as

$$\Gamma_{z,net} \equiv \Gamma_{neu,par}(x_1) + \sum_{a=1}^{z} \Gamma_{a,par}(x_1) - \sum_{a=0}^{z} \int_{x_1}^{x_2} \nabla_{\perp} \cdot \mathbf{\Gamma}_{a,par} dx = \int_{x_1}^{x_2} S_z \cdot n_e \cdot n_z dx \tag{3.6}$$

The definition of $\Gamma_{z,net}$ includes neutral and ion particle flux ($1 \leq z \leq z$) and the effect of transport perpendicular to the line of sight. When the excitation and the ionization have the same spatial distribution along the line of sight, i.e.,

$$\begin{aligned} X_{0k} &= X_0 f(x) \\ S_z &= S_0 f(x) \end{aligned} \tag{3.7}$$

where X_0 and S_0 are the constants, the relation between $\Gamma_{pho,km}$ and $\Gamma_{z,net}$ can be derived as shown below.

$$\frac{\Gamma_{z,net}}{\Gamma_{pho,km}} = \frac{\int_{x_1}^{x_2} S_z \cdot n_e \cdot n_z dx}{\int_{x_1}^{x_2} n_e \cdot n_z \cdot X_{0k} \cdot B_{km} dx} = \frac{S_0}{X_{0k} \cdot B_{km}} \tag{3.8}$$

The physical meaning of $\Gamma_{z,net}/\Gamma_{pho,km}$ is counts of ionization event per photon emission and is sometimes called inverse photon efficiency. This simple relation shows if a reliable value of S/XB is given from a atomic database, the particle flux from the surface can be derived from the photon flux measured experimentally. This approach is valid only where recombination can be neglected.

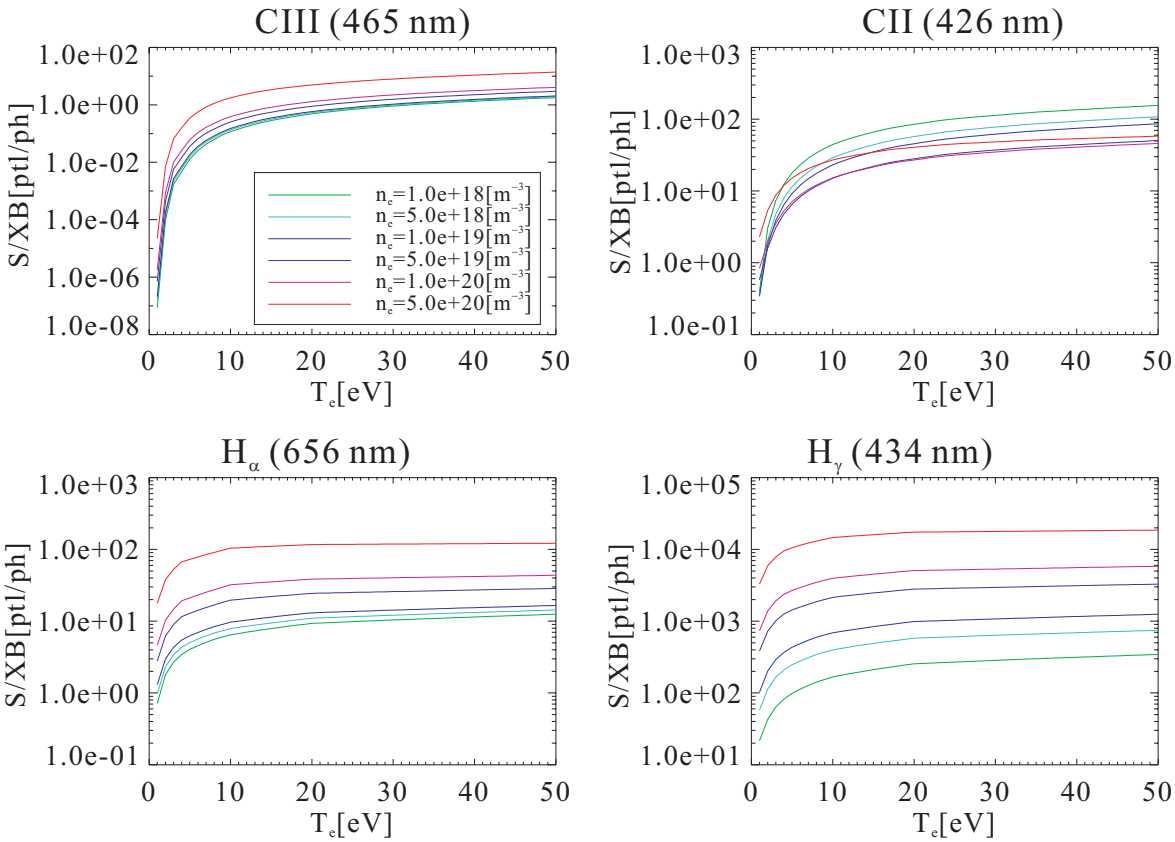

Figure 3.2: *S/XB variations on T_e and n_e from ADAS (2002)[33]*

3.1.3 ADAS: a Collisional Radiative Model for Atomic Data Evaluations

In the boundary plasma region where this method is normally applied, estimation of S/XB from the simple coronal or the local thermodynamic equilibrium models can be erroneous, since both models may be invalid in the ranges of electron density and temperature in this region. Therefore, a full collisional radiative calculation without any adhoc assumptions on ionization equilibrium is necessary to obtain the reliable value of S/XB and the other atomic data. In this study, the ADAS system (Atomic Data and Analysis Structure)[34] is utilized to obtain S/XB. ADAS is a general atomic database and code package for detailed collision-radiative modelling. It calculates the relative abundance of the each charge state solving the rate equations including the various atomic processes. According to the database, as shown in fig 3.2, T_e and n_e at the emission shell are prerequisite for the reliable estimation of particle influxes, due to the relatively strong dependence of S/XB on local T_e and n_e. Unfortunately, the accuracy of this method is often hampered due to the inhomogenity of T_e and n_e along

the line of sight. S/XB is a local parameter which is a function of T_e and n_e and due to the line of sight integration through an inhomogeneous plasma, the determination of S/XB has an error associated with it inherently. But when the emission shell is quite localized compared to the characteristic length of T_e and n_e variations, then the above effect can be negligible .

For a better treatment of the effect of the line integration, the edge plasma simulation code can be applied. Using the outputs of this code, which include T_e, n_e, Γ_z (particle flux), the line integrated photon emissivity can be calculated directly using the photon emission coefficients. This will be described further in detail in chapter 4.

3.2 Experimental Setup for Measurements of the Influxes

In this section, various detectors and lines of sight installed for the flux measurements are described. Only detectors in the visible range are addressed since measurements in ultra violet range are less suitable under tokamak conditions due to the difficulties in absolute calibration. With the help of a central quartz fiber switch board, all available lines of sight can be coupled to each detector system. Three letter identifiers of the systems refer to the diagnostic names in the ASDEX Upgrade shotfile database. Calibration procedures and the details of measurement systems are described in the appendix A.

3.2.1 Visible Survey Spectrometers (VSL, VSM)

These spectrometers are mini-spectrometers which are installed in PCs with the PCI interface. These are multiple diode array detectors with gratings. These cover the whole visible spectrum range (350-900 nm) with low spectral ($\Delta\lambda/pixel \sim 1nm$) and temporal resolutions (5-100ms). These spectrometers are routinely coupled to divertor lines of sight and are used for the influx measurements in inner and outer strike point modules.

3.2.2 High and Low Resolution Spectrometers (CDL, CDH)

These systems are mainly connected with the main chamber lines of sight. CDL is a one-meter Czerny-Turner spectrometer and CDH is a Fastie-Ebert spectrometer equipped with an Echelle grating system, respectively. These spectrometers are coupled to image intensifiers and programmable CCD camera (1024x1024 pixels)[35] for detection of the photon intensity. CDL has a spectral resolution around 0.014 nm depending on the wavelength and is routinely used for measuring CII (426.5nm), CD (430.5nm), and D_γ (434.5nm) simultaneously. Due to high spectral resolution (0.001nm) of CDH in

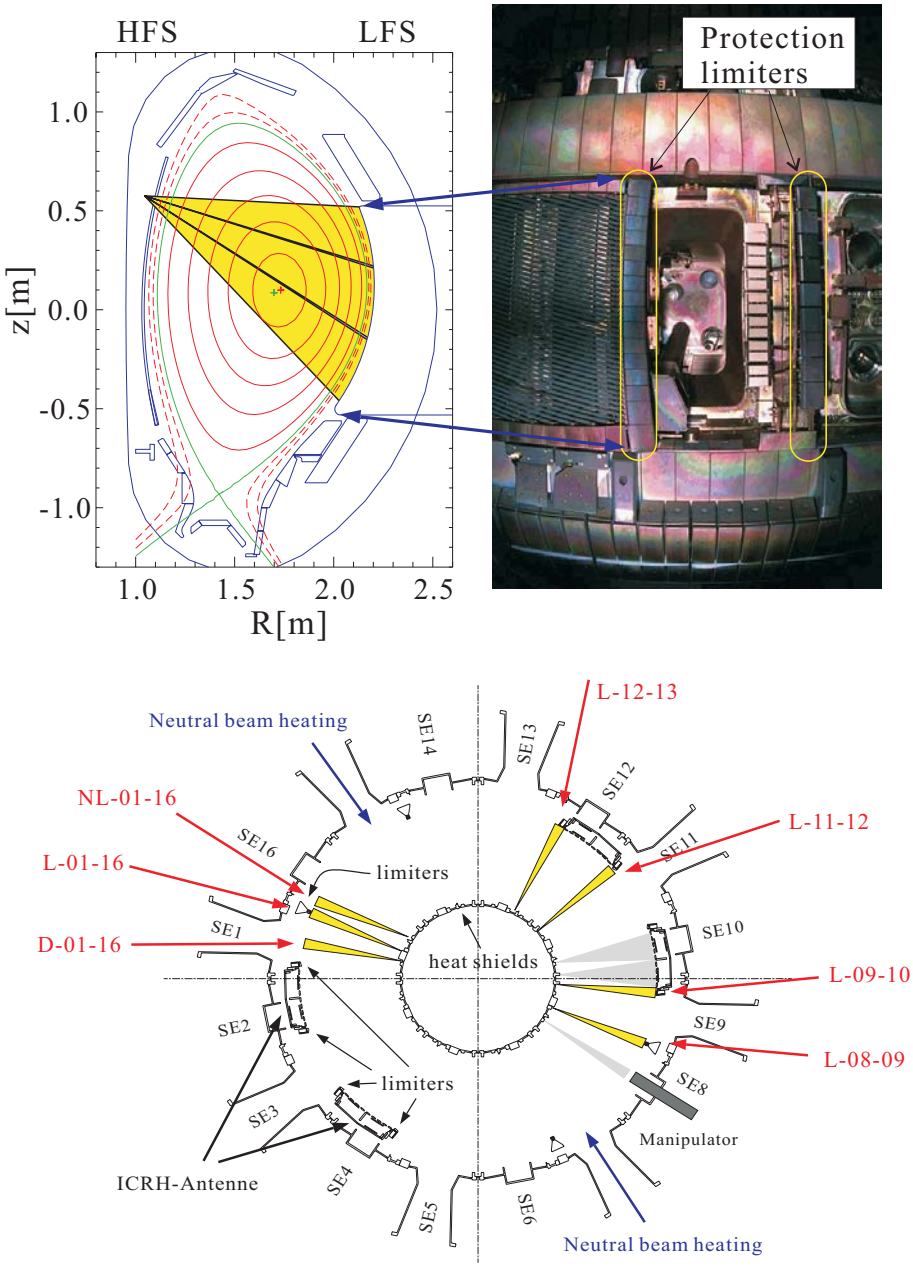

Figure 3.3: *The lines of sight for limiter spectroscopy. The poloidal and toroidal views are shown. The protection limiters are shown in the photo. These lines of sight cover the whole limiter area (L-...) and the area in-between (NL-..., D-...) the limiters. For each system, for example, L-01-16, three lines of sight (upper, middle, and low) are available as shown at the poloidal view.*

the visible range, it is used for Zeeman analysis, and thereby can determine separate contributions of high and low magnetic field sides in ASDEX Upgrade.

3.2.3 Photomultipliers (DIV)

Two detector lines, each equipped with 16 channel photomultipliers have narrow-bandwidth (FWHM $\sim$ 1-2 nm) interference filters in each line. These photon counting systems have a maximum temporal resolution of 50 μs. Due to the high temporal resolution to resolve fast events, the phtomultipliers can be used to investigate Edge Localized Modes(ELM's), which are the quasi-periodic bursts of plasma particles and energy at the edge region of tokamak.

3.2.4 Limiter Spectroscopy (LVS)

Figure 3.4 illustrates the lines of sight for the influx measurements of the low field side including the protection limiters and the area in-between the limiters. To cover all limiter surfaces, these lines of sight are available for each fiber head and have no optics attached and therefore cover large areas compared to the other lines of sight (with the opening of the fiber guides). In fig 3.3, the lines of sight connected to the spectrometer are shown. Since the photon fluxes in the main chamber are generally smaller compared to the divertor region, these lines of sight are mostly detected with a dedicated detector equipped with a CCD camera and a mechanical shutter. This system has an improved signal to noise ratio compared to detectors with an image intensifier, but a slower temporal resolution.

3.2.5 The Installed Lines of Sight

For high spatial resolution of each line of sight (LOS), the optical quartz fibers installed at the divertors and the main-chamber are focused like pencil-beams with a concave mirror in front of the fiber heads, as shown in Fig 3.4 and 3.5. The other ends of the fibers are connected to a switching board with the use of flexible connections of the fibers and the detectors. Focusing the lines of sight, except for the limiter lines of sight, results in local intensity measurements with a diameter of 1 cm on the spots. The main plasma facing components are covered, including the inner heat shield, protection limiters, and inner and outer divertors.

3.2.6 Spectroscopic Measurements of the Carbon Concentrations inside the Separatix (COM)

To monitor carbon and oxygen concentrations inside the separatix, grazing-incidence Bragg crystal detectors are used[36, 37]. These equipments consist of a grid collimator,

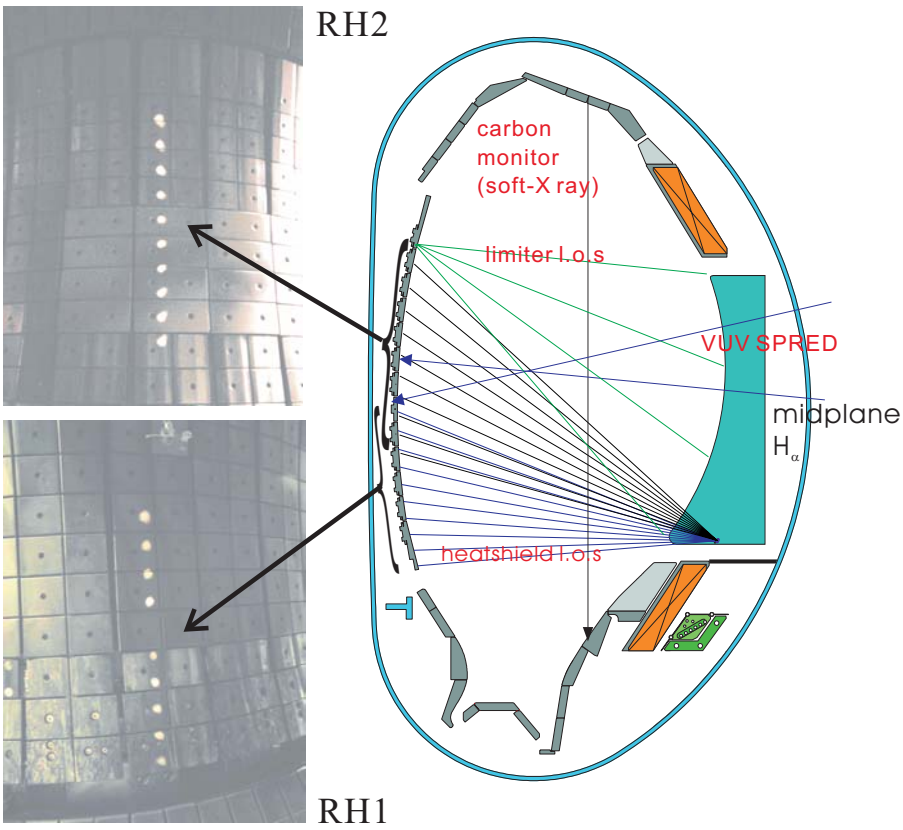

Figure 3.4: *Main-chamber radial lines of sight installed in ASDEX Upgrade. Two systems, RH1 and RH2, are available for monitoring the inner heat shield. The observed spatial regions are indicated by the spots obtained by backward illumination of the diagnostic system. Additionally, the lines of sight for the midplane H_α and the carbon monitor are shown.*

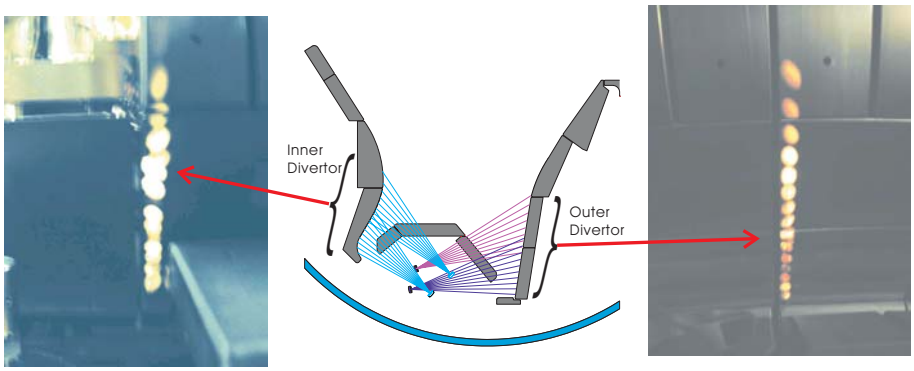

Figure 3.5: *The lower divertor radial lines of sight installed in ASDEX Upgrade. The observed spatial regions are indicated by the spots obtained by backward illumination of the diagnostic system.*

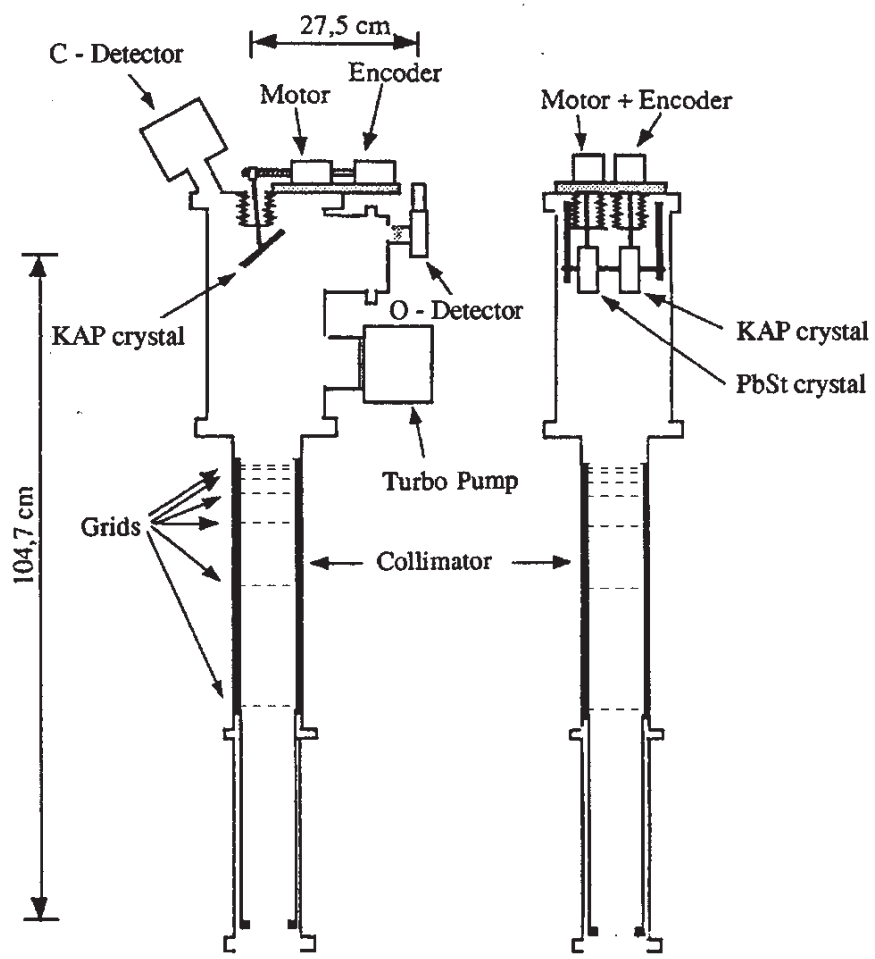

Figure 3.6: *Schematic view of the C-O monitor.*

a flat crystal for the first order Bragg reflection at the fixed angle, and the detector. A schematic view of the spectrometers is shown in fig 3.6 and the line of sight is shown in fig 3.4. A potassium acid phthalate (KAP) crystal (2d=2.658 nm) and a PbSt crystal (2d=10.04 nm) are used for first order Bragg reflection of the OVIII (λ=1.897nm) and the CVI (λ=3.374nm) Lyman-α line radiation, respectively. The X rays are detected by gas flow proportional counters of multistrip gaseous chamber type (MSGC). For the OVIII line, the absolute calibration is done with a calibrated large area X-ray tube but for CVI, no direct calibration is available due to geometrical reasons and it is cross-calibrated indirectly against carbon concentrations from other diagnostics (bremsstrahlung Z_{eff} and charge-exchange recombination spectroscopy).

For the determination of the concentrations from the measured photon intensity

(I_m),

$$I_m = \frac{1}{4\pi} \int_l h\nu n_x n_e \langle \sigma v_e \rangle \, dl \tag{3.9}$$

the coronal equilibrium is assumed without the transport effect.

$$n_x = C_{imp} \cdot f_x \cdot n_e \tag{3.10}$$

where $h\nu$ is the energy of the emitted photon, n_x is the impurity density of the H-like ionization stage, n_e is the electron density, T_e is the electron temperature, C_{imp} is the total concentration of the impurity and l denotes the length of the line of sight. $< \sigma v_e >$ is the excitation rate coefficient and f_x, which is the fraction of n_x, is dependent only on T_e when the coronal equilibrium model is assumed. C_{imp} can be estimated as follows.

$$C_{imp} = \frac{4\pi I_m}{\int_l h\nu n_x n_e^2 \langle \sigma v_e \rangle \, dl} \tag{3.11}$$

assuming that the radiation is localized in a radiation shell which is characterized by the average emission radius (r_s).

$$r_s = \frac{\int_l h\nu n_x n_e^2 \langle \sigma v_e \rangle \, r dl}{\int_l h\nu n_x n_e^2 \langle \sigma v_e \rangle \, dl} \tag{3.12}$$

The term r_s is expressed as a poloidal flux surface radius ρ_{pol}[1] and n_e and T_e are obtained from the Thomson scattering measurements (see next section).

In this study, the coronal model is bypassed using the full two-dimensional code to calculate the concentration, treating the effects from the line of sight integration and transport characteristics.

3.2.7 Electron Density and Temperature at Outer Midplane from Thomson Scattering Measurements

The measurement of n_e and T_e is critical for the interpretation of the spectroscopical measurements and the transport simulations. Here, a short description of Thomson scattering measurement will be given.

As shown in fig 3.7, the edge Thomson system consists of 6 lasers fired repeatedly to improve the temporal resolution and 16 spatial channels. Measuring the scattered light from the lasers through the incoherent scattering[17], where the wave is scattered at free, uncorrelated electrons, n_e and T_e are then calculated (n_e from the calibrated

[1] ρ_{pol} is a typical radial coordinate used in a nested flux surface configuration as a Tokamak (0:plasma center, 1:separatix). See Appendix C for its definition.

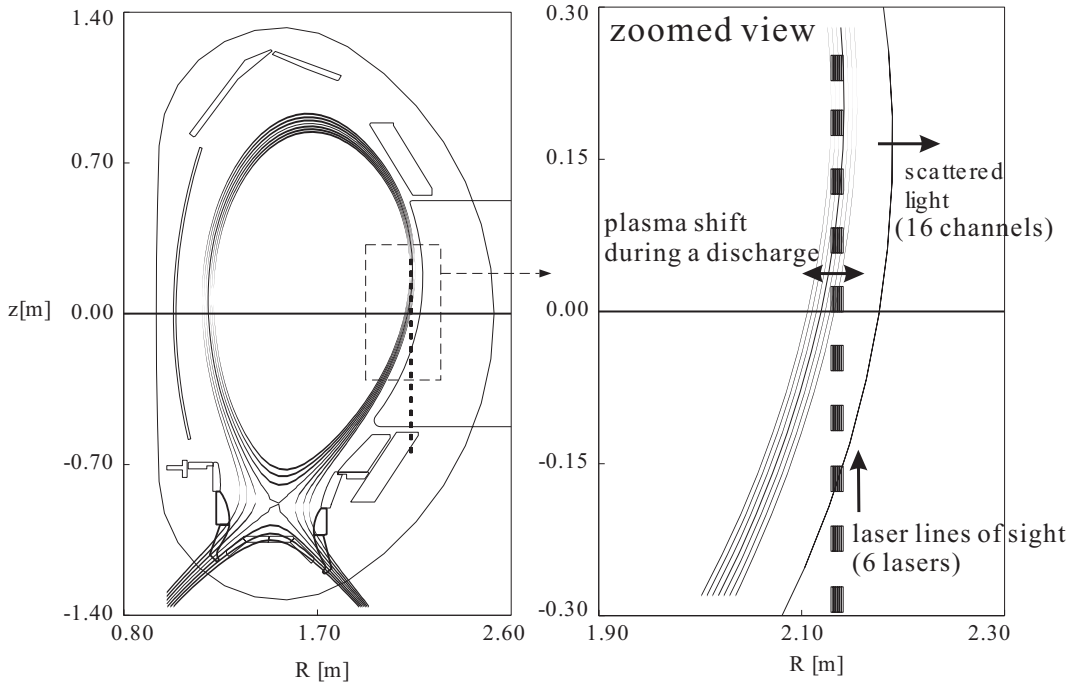

Figure 3.7: *The vertical Thomson scattering system in ASDEX Upgrade*

intensity of the scattered light and T_e from the spectrum of the scattered light)[17]. In ASDEX Upgrade, Nd:YAG lasers with $\lambda = 1.06nm$ are used, which are fired with 50Hz[38]. For a profile measurement of n_e and T_e around the narrow pedestal region (about 2cm), a special method is required to enhance the resolution of the system. To this end, the slow shift (for about 1 second) of the plasma position (about 1 cm) relative to the fixed lasers is applied during the stationary phase of a discharge where the plasma parameters are constant in time. To reduce the outlying data points which are mainly due to the turbulent nature of the plasma in this region, Bayesian statistics[39, 40] are applied and the profiles of typical H-modes are shown in fig 3.8. After Bayesian box car average of the data points, the pedestal structure can be reconstructed. For the core region, as shown in the figure, n_e profiles are flat compared to T_e profiles.

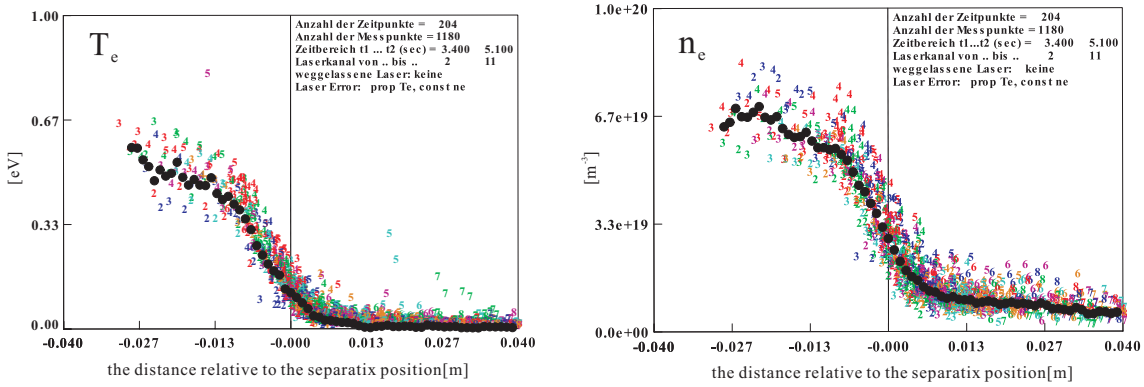

Figure 3.8: *A example of T_e and n_e profiles at the outer midplane of a typical H-mode from the edge Thomson scattering system. Using the radial plasma sweep and the Bayesian averaging, the pedestal structure of the profiles are reconstructed. The black dots are the fitted profiles and the colors label the lasers and the numbers correspond to different spatial channels of the detection system.*

4

Adaptation of the B2.5 code and the Fit Procedure

4.1 B2.5 : a Two Dimensional Fluid Plasma Edge Transport Code

4.1.1 A short Description of the B2.5 code

To take into account all the transport and atomic processes of the plasma and impurity species of edge plasma in toroidal geometry, numerical calculations are necessary. In principle, the full kinetic treatment, solving Boltzmann equations[41] for all species coupled with Maxwell equations, is possible. However, the computational effort for kinetic simulations is too demanding for the present computational technology. Typically, a fluid approximation, applying velocity moments on the kinetic equations, is widely used for edge transport simulations. A fluid description of the plasma is useful when the main interests are on the macroscopic quantities which are changing slowly compared to the relaxation process to a Maxwellian distribution. The fluid description demands less computational effort than the kinetic approach due to the reduced degree of freedom of the system in concern.

The B2.5 code is a multi-fluid edge transport code package based on the Braginskii formulation of plasma transport[41]. It solves the continuity and the momentum equations for each charge state and a single energy equation for all species which are derived from the full kinetic equations. Usually neutral transport processes are treated with the external Monte-Carlo code EIRENE [42]. However, a fluid treatment of neutrals using the Navier-Stokes equations is also available within the stand-alone version of B2.5, resulting in much faster calculations. The governing equations and boundary conditions are summarized in Appendix B. The physical geometry and computational meshes are shown in fig 4.1.

The basic particle and power balances of B2.5 simulations are illustrated in fig 4.2.

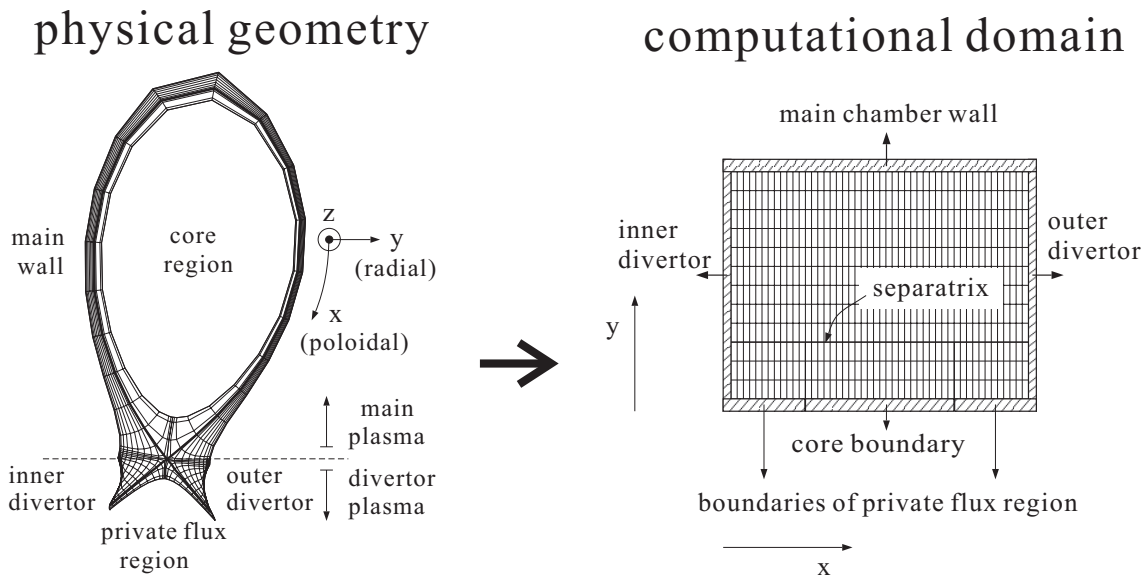

Figure 4.1: *The physical geometry and the rectangular computational meshes for B2.5. Toroidal symmetry is assumed.*

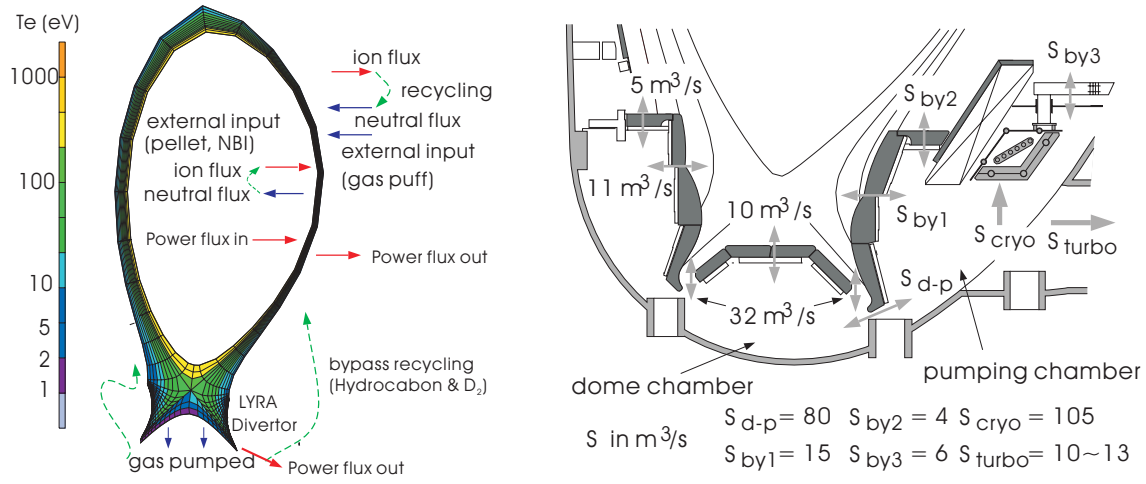

Figure 4.2: *A schematic view of the particle and power balances in B2.5 code (left). The conductance of the various valves around the lower divertors (right).*

The external electron and ion input power is introduced at the core edge boundary and mainly transported radially through diffusion and convection processes to the scrape-off layer (SOL) region and then following the open magnetic field lines to the divertors. The radial temperature profile at the midplane is determined largely by the radial heat fluxes and the thermal diffusivity in the closed magnetic surfaces. In the SOL region with the open magnetic field, both the radial and parallel transport determine

the decay length of ion and electron temperatures. Additionally, there are the internal ohmic heating and heat exchange between ions and electrons and the radiation losses from the plasma.

In case of the particle balance, the influxes from the material surfaces by the recycling process dominates the external particle inputs, such as the neutral beam fuelling in the core boundary and the gas influxes from the external valves at the boundary region. Basically the density profiles are determined by the radial transport and the ionization pattern of the recycling particle flux and the pumping rate of neutrals below the divertor region. In addition, for ASDEX Upgrade, due to the opening of the divertor baffles between the divertor and main chamber modules, the neutral flux can penetrate into the main chamber both from the in-board side and the out-board side through neutral bypasses[43], as shown in fig 4.2. In typical calculations, the bypass fluxes are neglected due to the difficulties of simulation capability and the fraction of neutral bypass fluxes to the main chamber neutral fluxes is 1/3 or below[44]. For the impurity, such as carbon, the main source of the particles is the erosion flux both from the main chamber and the divertors resulting from the plasma wall interactions as shown in fig 2.1. With the given influxes, the radial profiles are determined by the transport processes (for the core region with the closed magnetic surfaces, purely by the radial direction, and for the open magnetic surfaces, by competition of the radial and the parallel directions) and ionization and recombination processes.

4.2 Development of the Fit Routine for the Adaptive Simulations of B2.5

The standard version of B2.5 is optimized for predictive simulations with typical boundary conditions. There is no direct way to set the experimental data as the corresponding boundary conditions in combination with the other input parameters of the simulation code. For the extensive interpretation of the experimental data and matching the diagnostics with the simulations, a special interface is required. The general interpretative version of B2.5 was developed for this purpose and applied to the previous study[45, 46], based on the fluid description of neutrals. This version was aimed at the extraction of the transport coefficients at the outer midplane in ASDEX Upgrade using the outer midplane electron temperature from Thomson scattering diagnostics and density from Li beam diagnostics. However, this version has some limitations in several aspects. First, it was developed for a pure deuterium case only and impurities are not considered. Hence the impurity radiation is not included in the power balance calculation. Second, the incorporation of the line integrated spectroscopic measurements as a fit constraint was not available, which is the critical experimental data for impurity simulations. Third, radially uniform transport coefficients (D, χ) are used for simplicity. However, as discussed in chap 2 (fig2.6), for H-modes, this assump-

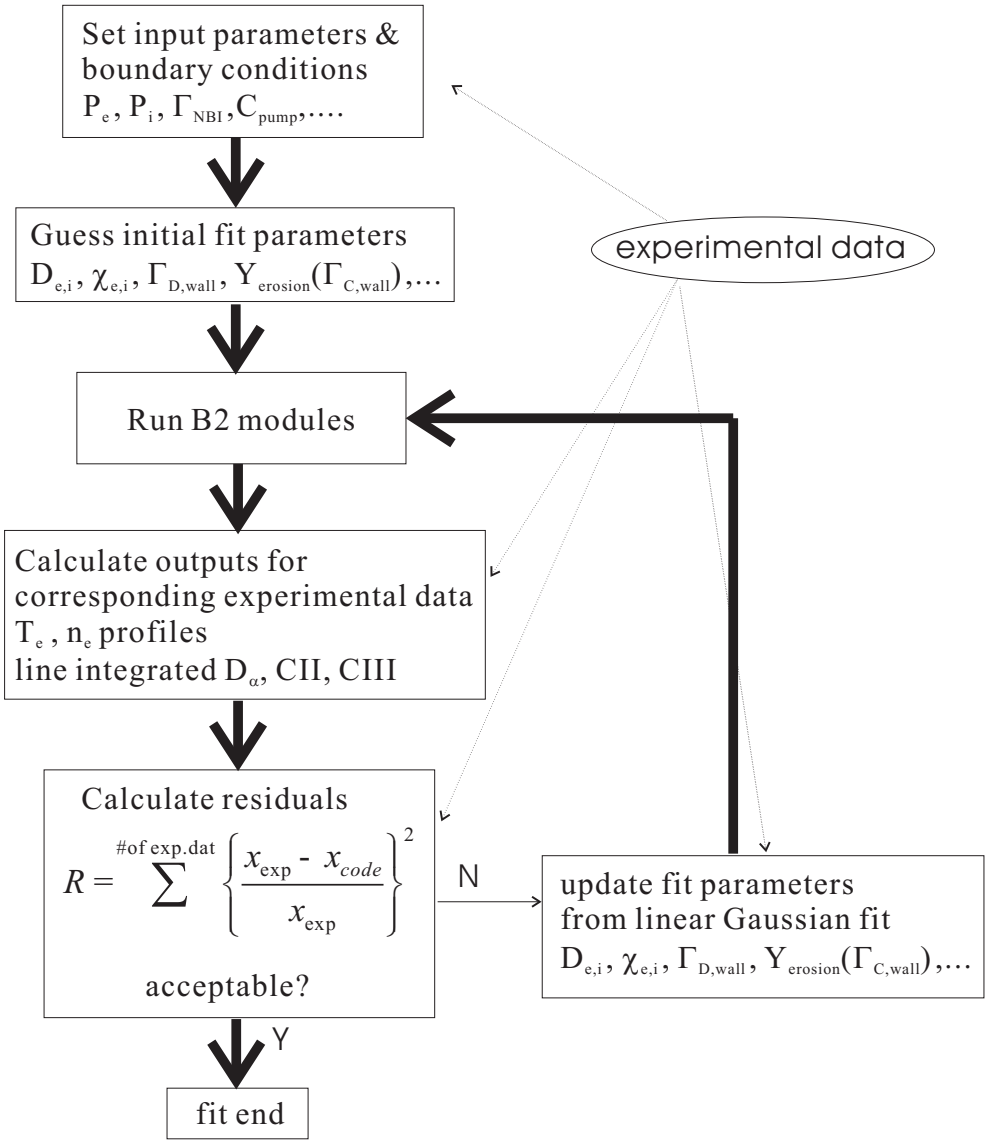

Figure 4.3: *Fit procedures for B2.5 simulations. The experimental data used are typically T_e and n_e at the outer midplane and the outer divetors, D_α, CII and CIII intensities along the midplane lines of sight, the power and the particle inputs, T_e, n_e and ion saturation current at the outer divertor. The fit parameters are $D_{e,i}$, $\chi_{e,i}$, $\Gamma_{D,wall}$ and $Y_{erosion}$.*

tion is not valid due the presence of the steep density and temperature gradients in the pedestal region. For a reasonable simulation of this pedestal structure, radially varying transport coefficients are necessary.

For this study, a new B2.5 fit routine is developed for impurity transport and

the fit procedure is illustrated in fig 4.3. For the reasonable analysis of the edge transport characteristic in H-modes, the contribution of the transport barrier will be critical, because T_e and n_e profiles are steep in this pedestal region (fig 2.6, 3.8). To simulate these transport characteristics, three radially different values of the transport coefficients are introduced in the fit procedures for the core edge region, the pedestal region and the cold edge region respectively[47]. The general scheme is as shown in fig 4.3. For the calculation of the line integrated photon fluxes with the simulated two-dimensional T_e and n_e profiles, the following formula is applied.

$$I_{pho} = \int_l \alpha\left(T_e, n_e\right) \cdot n_z \cdot n_e \, dl \tag{4.1}$$

where $I_{pho}[photons/(m^2\ sr\ s)]$ is the line integrated photon flux, $\alpha\left(T_e, n_e\right)$ is the photon emission coefficient of the spectral line from ADAS[34] and l denotes a line of sight in concern. n_z is the density of the radiating species. T_e and n_e are the density and the temperature of the electrons. For each iteration, I_{pho} for spectral lines are calculated from the T_e, n_e and n_z profiles.

The aim of fit routines are to determine the radial transport coefficients of both deuterium and carbon ions. Physical constraints are T_e and n_e profiles at the outer midplane from Thomson Scattering and also T_e and n_e at the outer divertor from Langmuir probes in ASDEX Upgrade. The D_α line radiation is used for estimating the recycling flux of the deuterium neutrals at the main chamber surface. The spectroscopic measurements of carbon influxes which are discussed in chap 3 are used to specify the carbon sources. Since no radially resolved carbon profiles are available, the CVI Lyman alpha radiation is used for core carbon concentration calculation. In this case, no coronal equilibrium is assumed and the photon intensity of CVI is used as the fit constraint directly.

The basic fit procedure will be as follows. First, the boundary conditions for the initial run are specified, such as the electron and ion power flux at the core boundary, the deuterium particle flux from the neutral beam heating, and the pumping rate at the roof baffle. Then the first run is carried out with the initial guess of the transport coefficients, the particle fluxes of the deuterium and carbon neutrals at the main chamber wall. With the calculated T_e and n_e distributions, the output of the corresponding experimental data are calculated next, such as the line integrated photon fluxes (CII, CIII, CVI, D_α). Through comparison of the experimental T_e and n_e profiles from the edge Thomsen scattering system at the outer midplane with the simulated T_e and n_e, new transport coefficients are calculated from the linear Gaussian fit algorithm. Comparing the experimental D_α intensity with the simulated intensity, the new deuterium gas influx at the main chamber wall will be calculated. For carbon, similarly, through the comparison of CII and CIII intensities, new carbon influxes at the main chamber wall will be estimated for the next run. For the estimation of the new carbon influxes, the Roth formula is used with an estimated multiplication factor based on the as-

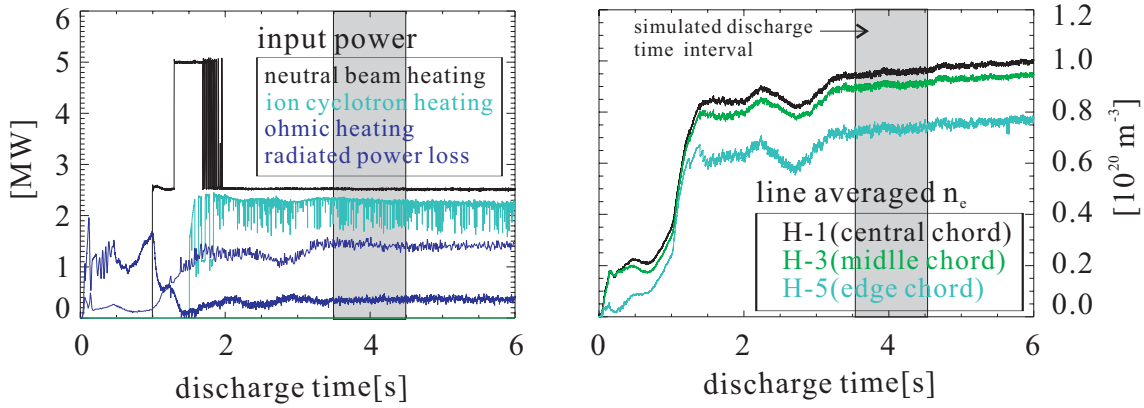

Figure 4.4: *The time trace of the power input and the line averaged densities of the discharge 15160 along the three different chords (central, middle, and edge). The selected time interval is shown as the grayed region* ($3.5[s] \leq t \leq 4.5[s]$).

sumption that the parameter dependence of Roth formula is valid. These procedure is repeated until the residuals between the measured and the simulated values fall below the prescribed level.

4.3 The Fit Results : Standard H-mode

In this section, the fit result for an H-mode discharge in ASDEX Upgrade (shot:15160) will be discussed. This discharge has the optimized magnetic configuration for the edge diagnostics, so called Edge Optimized Configuration. In fig 4.4, the time traces of the input power and the line integrated densities from the interferometry of discharge 15160 are shown for the background plasma. 2.5[MW] of neutral beam heating and 2[MW] of ion cyclotron resonance heating are applied. The time interval between 3.5[s] and 4.5[s] is selected and during this time interval, the plasma parameters are stationary. For the fit procedure, the same values of the diffusion coefficient (D) and the thermal diffusivity (χ) are assumed for deuterium and carbon ion species ($\chi_D = \chi_C$). The radial inward pinch (v_{pinch}) is assumed only for the carbon ions in the transport barrier region. For the ion temperature, no experimental data is available and therefore χ_i is assumed to be equal to χ_e.

In fig 4.5, the results of the fit procedure are compared with the experimental T_e and n_e profiles at the outer midplane. The simulation results are shown both for the deuterium only case and the deuterium-carbon case. According to the fit results, the fitted χ_e and D are similar for both cases. Three different values of the transport coefficients are fitted for the core, the pedestal, and the outer wing (the cold scrape-off layer) regions respectively. T_e and n_e profiles are well reproduced with the fitted transport coefficients. As shown in the figure, the fitted D and χ are reduced in the

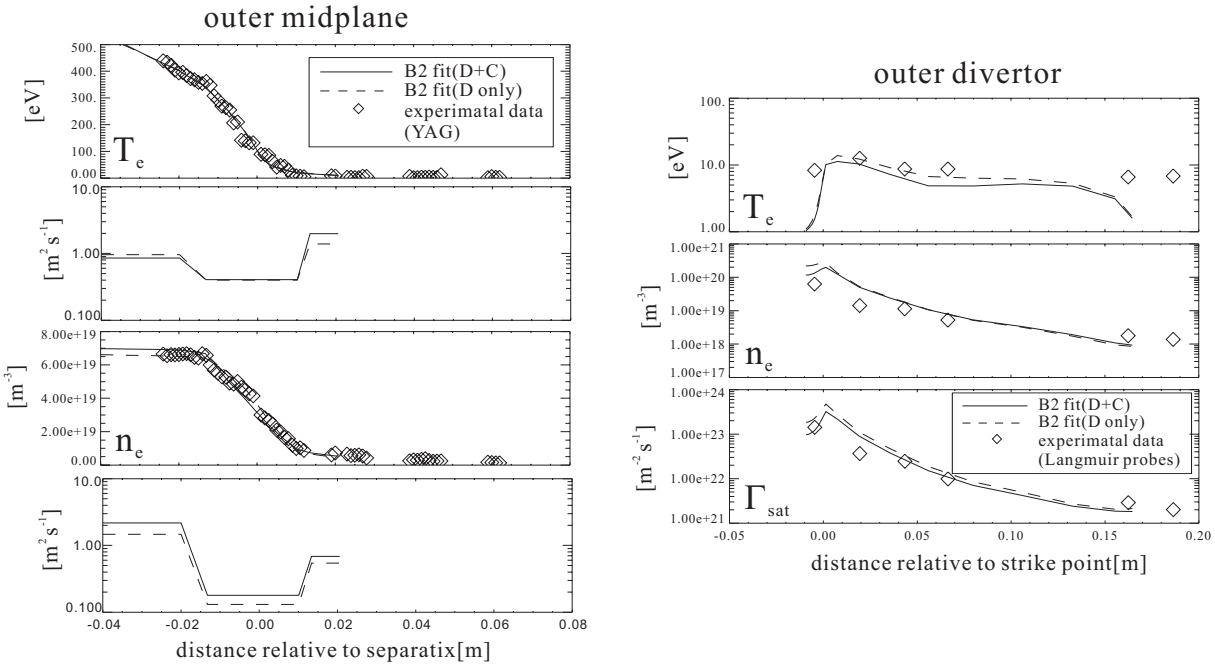

Figure 4.5: *The fitted profiles of T_e, n_e, both at the outer midplane and the outer divertor, and the transport coefficients (D, χ) of the discharge 15160. The same D and χ are assumed for both electrons and the ions (including carbon species). The fitted results are shown for two cases: the B2.5 fit with deuterium only and the B2.5 fit with both deuterium and carbon considered. the points at x=0 are the separatix for the outer midplane and the striking point for the outer divertor.*

pedestal region compared to the core and the outer wing due to the steep gradient of T_e and n_e in this region. The larger value of the fitted D and χ at the cold scrape-off layer part reveals a rapid anomalous transport towards the wall, factors above and hence in contradiction to Bohm diffusion[48] which is generally thought to be the upper limit of electrostatic turbulence[39]. The diffusion coefficient from Bohm diffusion level is:

$$D_{Bohm} = \frac{1}{16}\frac{T_e}{B} \tag{4.2}$$

where B is the magnetic field[T] and T_e is in unit of [eV]. When calculated with $T_e \simeq 20$[eV] and $B \simeq 2$[T], D_{Bohm} is $0.31[m^2/s]$, which is lower than the fitted D. This suggests a convective transport mechanism such as a strong outward drift in this region[39]. The effect of the neutral beam fuelling applied at the core boundary region on n_e is negligible compared to that of the recycling flux from the wall. Therefore, according to the B2.5 fit, the n_e profile is mainly determined by D and the recycling flux at the main chamber wall. The experimental profiles of T_e and n_e, which are the input parameters for the code, are from Thomson scattering measurements for the

outer midplane (fig 3.8) and Langmuir probes for the outer divertor.

On the right figure, the measured and the simulated profiles are compared for the outer divertor along the plate. T_e profile is in good agreement near the strike zone. The simulations predict higher n_e and the ion saturation current level at the outer divertor compared to the measurements. The Langmuir probes at the outer divertor are at a glancing angle with the magnetic field ($\leq 5°$). Therefore a shadow effect can be important for reliable analysis. To find out whether it is due to this effect or the code physics implementation, a further analysis is required.

The comparison of the measured and the fitted photon intensities are shown in fig 4.6 for the inner heat shield lines of sight. In this case, the CII and CIII photon intensities have similar values along the lines of sight which look at the tungsten tiles and the carbon tiles. As mentioned in the introduction, this implies the existence of carbon layers on top of the tungsten coating or a recycling nature of the carbon wall interaction. This will be further examined in chap 5. At the lower part of the heat shield, the discrepancy increases between measurements and simulations. This may result possibly from bypass fluxes from the inner divertor which are not considered in the simulations.

In fig 4.7, the time traces of the line integrated photon fluxes for an type-I ELM event are shown from the photomultipliers and the photodiodes. The discharge 17427 and 17428 have very similar plasma conditions. For discharge 17427, one of the channel of the photomultiplier system, looking near the inner bypass port, is equipped with a D_α filter. On the other hand, for discharge 14728, a CII (514nm) filter has been inserted. In the figure, three different lines of sight are considered, i.e., the outer divertor, the inner divertor and the bypass port between the lower part of the inner heat shield and the transition modules of the inner divertor. First, as shown in the figure, the delay of signals between the inner and the outer divertors implies the ballooning character of ELMs: Due to the larger path length from the outer midplane to the inner divertor compared to the outer divertor, the particle pulse of an ELM generated near the outer midplane reaches the inner divertor later than the outer divertor. Second, when the inner divertor and the bypass port are considered, D_α signals measured by the photomultiplier show a clear delay for the bypass port. This time delay is approximately $0.6\pm$ 0.3 [ms], which is larger than the sampling time interval of the photomultiplier. It can be understood as follows. After an ELM pulse reaches the inner divertor, the neutral flux below the roof baffle will increase. Then, through the conductance of the structure connecting the roof baffle and the bypass port between the inner heat shield and the inner divertor module, the pulse of the neutral flux will arrive at the bypass port in delayed time. Therefore, the increased intensities of D_α near the lower part of the inner heat shield can be accounted for by the bypass neutral flux. On the other hand, for carbon, as shown in the figure, there is no time delay of the signals between the inner divertor and the bypass port. The only explanation known by now would be that the CII light is caused by the fast heat pulse in the electron channel, with the

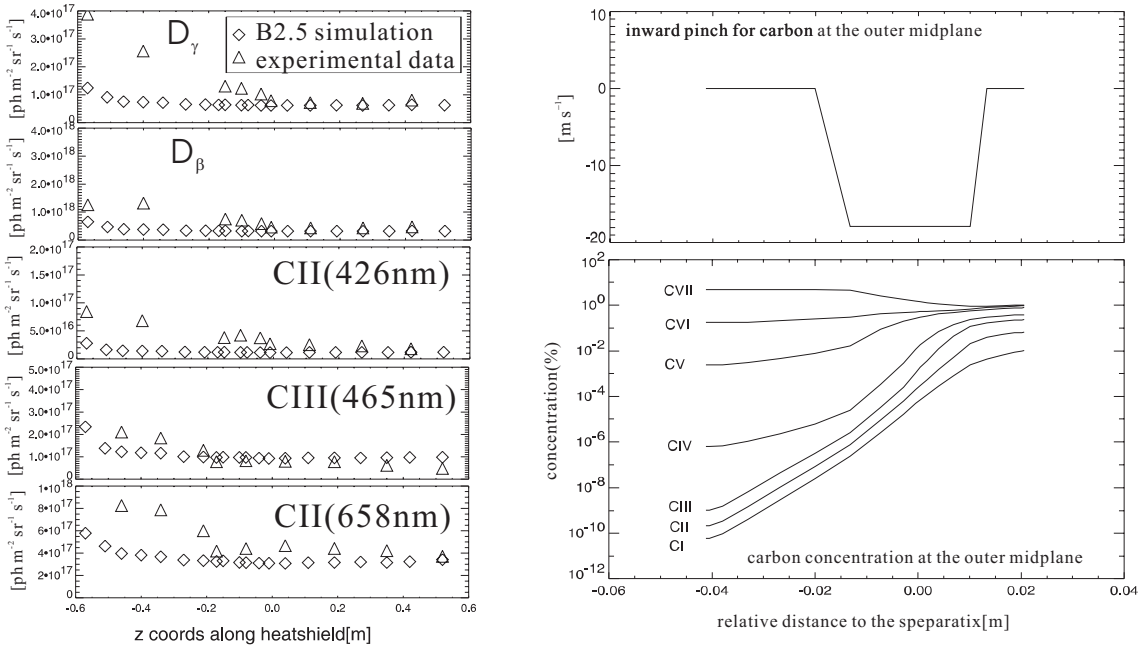

Figure 4.6: *The comparison between the measured and the fitted line integrated photon fluxes(a) of the discharge 15160 along the coordinates of the inner heat shield. Zero is at the central part of heat shield. The radial profile of the fitted inward pinch for carbon(b) at the outer midplane and the radial carbon concentration profiles at the outer midplane are shown.*

excitation of carbon already abundant in the SOL or by sputtering caused by sheath accelerated ions.

As shown in the right hand side of the fig 4.6, an inward pinch of about 15$[m/s]$ is required and this is in qualitative agreement with the previous study[13]. When compared to the coronal model, the simulations predict 30% higher concentration partly due to the transport effect which spreads carbon ions into spatial regions where their concentrations according to Saha-Boltzmann equilibrium would be very low. In addition, due to the limit of B2.5 mesh (around 4 cm inside the separatix, in this case), a part of photons in the core region is missed in the calculations. According to the simulations, the C^{6+} concentration is still higher than any other ionization stage at the scrape-off layer region and the coronal equilibrium model is not valid at this low T_e region due to the fast parallel transport to the divertor region.

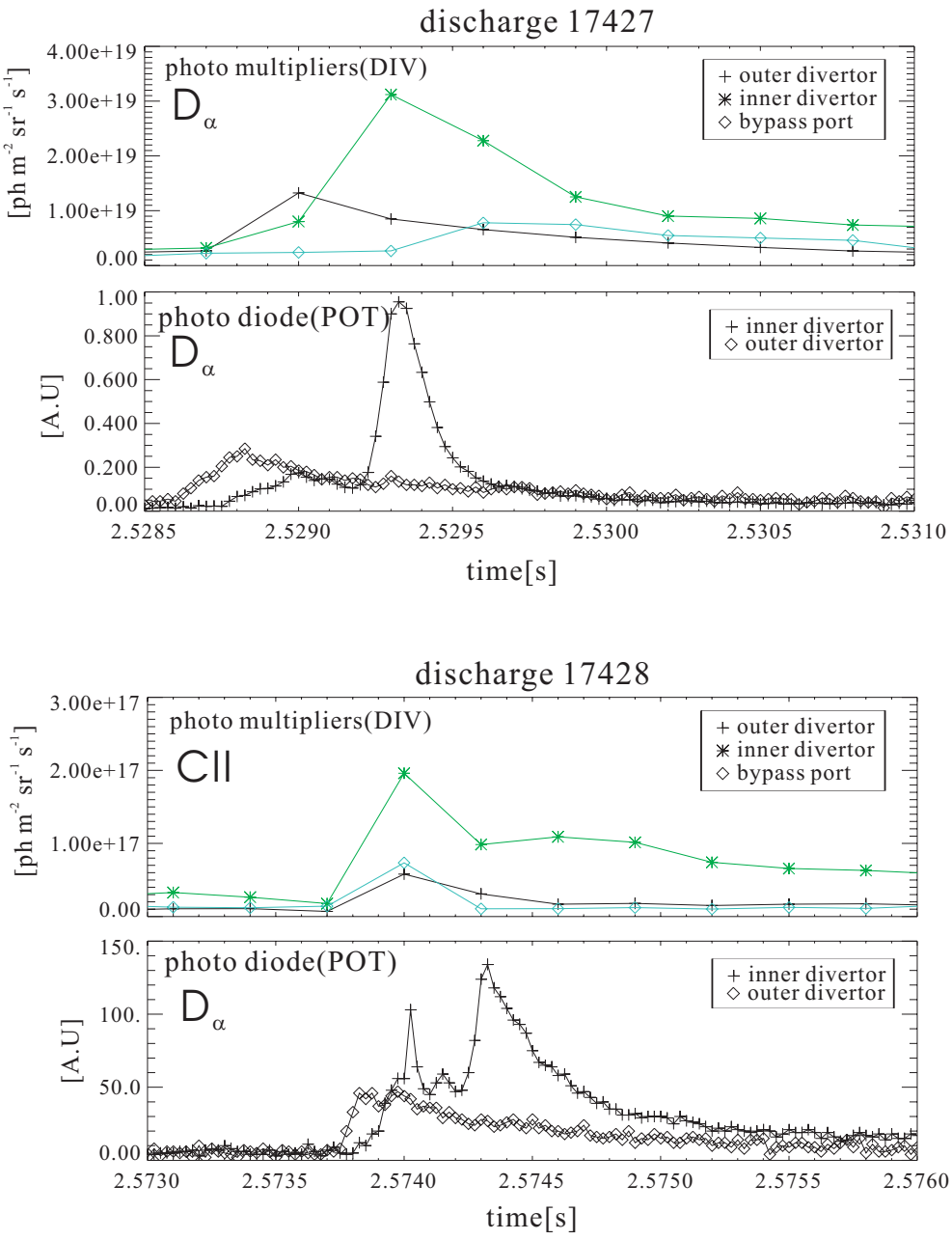

Figure 4.7: *The time traces of the line integrated photon fluxes for an type-I ELM event are shown from the photomultipliers and the photodiodes. Three different lines of sight are considered, i.e., the outer divertor, the inner divertor and the bypass port between the lower part of the inner heat shield and the transition modules of the inner divertor. The discharge 17427 and 17428 have very similar plasma conditions.*

5

Results and Discussion

In a diverted tokamak, the plasma wall interaction is highly concentrated in the divertor region. However, the relative contribution of the divertor sources to the core concentrations depends on the transport characteristics in the scrape off layer and the divertor retention. In this chapter, the experimental and computational results will be presented in detail for the carbon behavior in typical H-mode discharges with some comparison to L-mode discharges. The computations are done with the model validated transport parameter sets as described in the previous chapter.

5.1 The Relative Contribution of the Divertor and the Main Chamber Carbon Influxes to the Core Concentrations

As discussed in chap 3, according to the simple analytic model of the divertor carbon ion leakage to the main chamber and hence to the core concentration, the divertor carbon influx to the core plasma is negligible in comparison to the main chamber sources. In this section, this will be compared with the experimental database and the two-dimensional edge simulations.

With the spectroscopical database of the long-term correlation between the carbon influxes and the core carbon concentrations, the contribution of the divertor and the main chamber sources to the concentration will be described. The discharges are selected for the standard H-mode which is a routine discharge, repeated once each experimental day. The time period considered is from April 1999 to June 2000 and the low electron density phase with neutral beam heating only is chosen with similar discharge conditions. The line averaged density (n_e) is $4 - 4.5[10^{19}m^{-3}]$, input power (P_{NBI}) is approximately 5[MW], plasma current (I_p) is 1[MA], the magnetic field (B_t) is 2[T], and the safety factor at the edge ($q_9 5$) is around 3.1.

In fig 5.1, the long term trend of the CVI (3.37nm) intensities (left) and con-

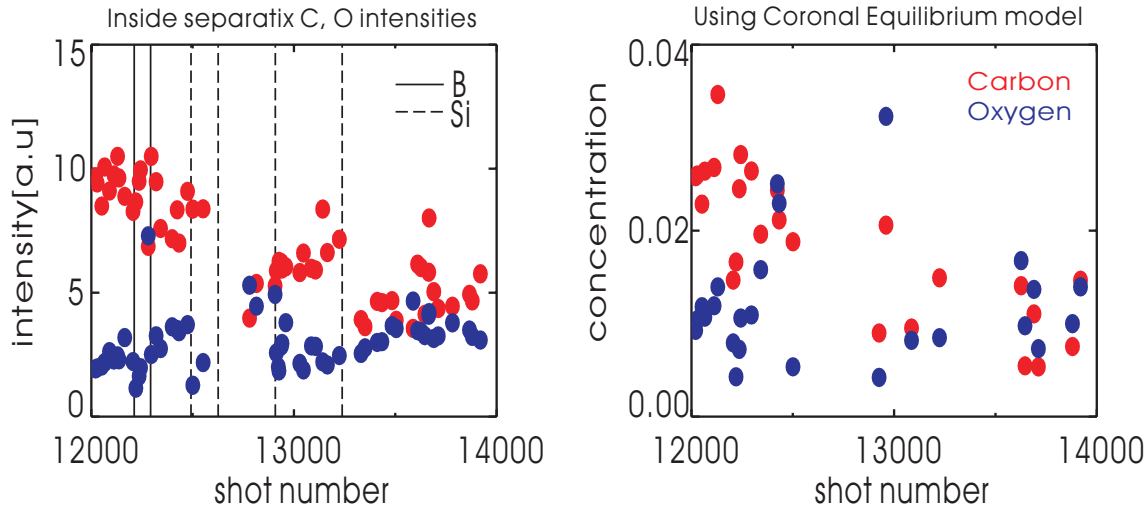

Figure 5.1: *The variation of the measured CVI photon intensities on the discharges of the standard H-mode at low density phase (left) and the corresponding concentrations (right) inside the separatix (Coronal model using the local electron temperatures). The vertical lines mark the times when the vessel conditioning has been applied via boronization or silliconization. The carbon concentrations decreased by about a factor of two over the period considered. Before the shot number 12860, no coating of tungsten is applied. After the shot number 12860, the lower part of inner heat shield ($1.2m^2$) was coated with tungsten (see Appendix E).*

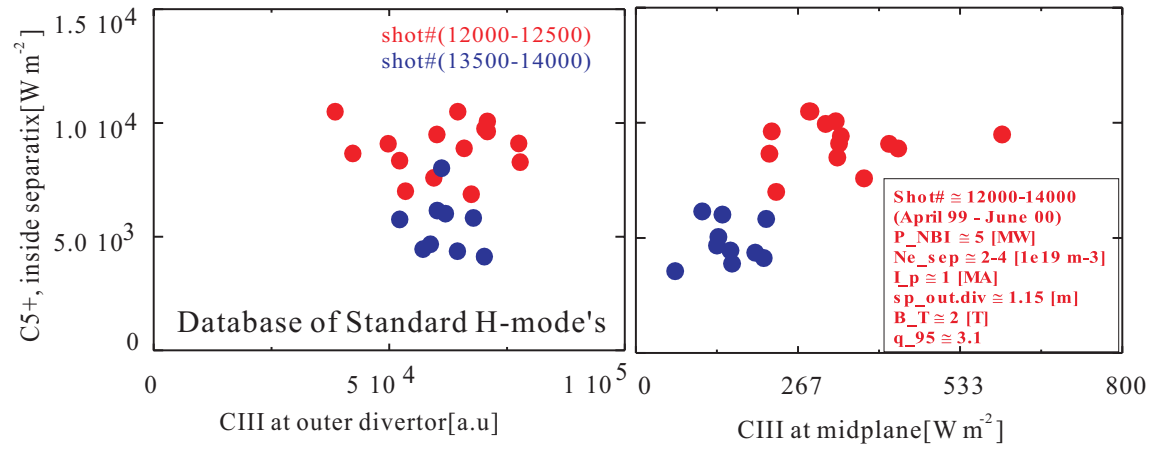

Figure 5.2: *The correlation of photon intensities and the core carbon concentrations. The left is the divertor intensities versus concentrations and the right is the main chamber intensities versus concentrations.*

centrations (right) are shown versus the discharge numbers. The spectroscopic line intensities are integrated along the vertical line of sight (carbon monitor, fig 3.4). The corresponding carbon concentrations are calculated assuming coronal equilibrium model (see section 3.2.6). The ionization layers for these lines are inside the separatix. The concentrations represent the core carbon and oxygen contents, when no strong inward pinch is present for these impurities. For comparison, oxygen intensities (OVIII, $\lambda = 1.90nm$) and concentrations are also plotted. According to the database, the core concentrations decreased by more or less a factor of two for this period, while oxygen concentrations remain relatively constant. When the same edge transport characteristics for these discharges are assumed, which is a reliable assumption with the similar T_e and n_e of the discharges considered here, these results suggest a decreasing level of carbon influx for this period. The presumed cause of this reduction of carbon concentrations is the accumulative wall conditioning and the long plasma exposure. However, the relative importance of these two mechanisms is unknown. Qualitatively similar results are reported from researchers at the other tokamaks (D3D, JET)[49, 50]. In their studies, it is also reported that no correlation is obtained between the core concentrations and the divertor influxes.

In fig 5.2, the correlation between the core CVI intensities and CIII (465nm) intensities at the outer divertor and at the main chamber is shown. In this case, to measure the characteristic photon intensities at the divertor, the line of sight is chosen just near the strike point of the outer divertor (fig 3.5). The main chamber line is along the horizontal midplane (fig 3.4, VUV SPRED). When no significant variation of local plasma parameters (i.e., similar T_e and n_e) is assumed, the photon intensity at the plasma boundary is proportional to the carbon influxes with the proportional constant S/XB as discussed in chap 3. According to the figure 5.2, the midplane carbon influxes have a better correlation with core carbon concentration than the divertor carbon influxes, although there are relatively large variations in the database partly due to the wall conditioning effect (such as boronizations and siliconizations) and the slightly varying plasma conditions. This suggests the stronger connection between the main chamber carbon sources and the core concentrations compared to the divertor sources. Yet this argument applies only for the outer divertor sources since interpretation of carbon lines in the inner divertor is very uncertain due to the low temperature and recombining conditions. available. However, due to the lower T_e and higher n_e characteristics of the inner divertor compared with those of the outer divertor, the carbon leakage from the inner divertor to the main chamber is supposed to be lower than that of the outer divertor due to the negative dependence of the retention with T_e, as considered in the analytic model in chap 2. Therefore, the inner divertor will be the weaker contributor to the core carbon concentrations.

Next, for an estimate of the relative contribution of the divertor and the main chamber carbon sources to the concentration, a series of B2.5 simulations have been carried out for typical plasma parameters of a standard H-mode discharge. To assess the

contribution of each source to the concentration, several cases are treated applying the Roth formula for the carbon erosion rates. In fig 5.3, the computational meshes and the results are presented. For the assessment of the contribution to the core concentration, the contamination efficiency is defined as the ratio of the core carbon density$[m^{-3}]$ to the total carbon influx$[s^{-1}]$, as shown in fig 5.3. This parameter suggests the relation between the source and the concentration. A higher value means higher efficiency of the sources which contribute to the core concentration. Three cases are considered, to determine the relative importance of each source to the core concentration.

- case I : carbon source only at the inner divertor
- case II : carbon source only at the outer divertor
- case III : carbon source only at the main chamber

According to the simulations, the contributions of the carbon sources in both the inner and the outer divertors to the core concentration is lower by at least an order of two compared to the main chamber carbon. It is due to the fact that the main chamber source is closer to the core region compared to the divertor sources. Total carbon influxes from the divertors ($1.3 \cdot 10^{21}[s^{-1}]$) are higher than that from the main chamber ($3.1 \cdot 10^{20}[s^{-1}]$). It is due to the fact that the higher power and particle fluxes reach the divertors and therefore compared to the main chamber, more concentrated plasma surface interactions take place. However, due to the low contamination efficiency of the divertor sources, the contribution to the core concentration (0.03%) is lower by a factor of 30 than that of the main chamber sources (0.9%). This result agrees qualitatively with the analytic model described in chap 2 and the results of the database described above. As a result, the controlling carbon source for the core carbon concentrations is the main chamber carbon source.

There are several limitations for the simulations. The outermost grid points of the computational meshes do not cover the real main chamber geometry due to the limited capability of the mesh generation scheme. The divertors and the inner heat shield are modelled reasonably due to the toroidal axisymmetry but for the protection limiters, which are inherently toroidally non-axisymmetric, the carbon influxes can be overestimated by factor of 3 from the difference of the effective plasma wetted area. On the other hand, by taking this point into account, the main chamber carbon source is still the dominant one by the factor of 10 compared to the divertor carbon sources and this result is qualitatively in agreement with the experimental database discussed previously. Early indications for this behavior are found in the ASDEX Upgrade divertor I tungsten experiments, where no significant effect of the divertor tungsten coatings on the main chamber carbon was observed[51].

As the result of this section, the main chamber carbon sources are dominant for the core carbon concentration. In next section, the separate contribution of the inner and the outer part of the main chamber will be assessed.

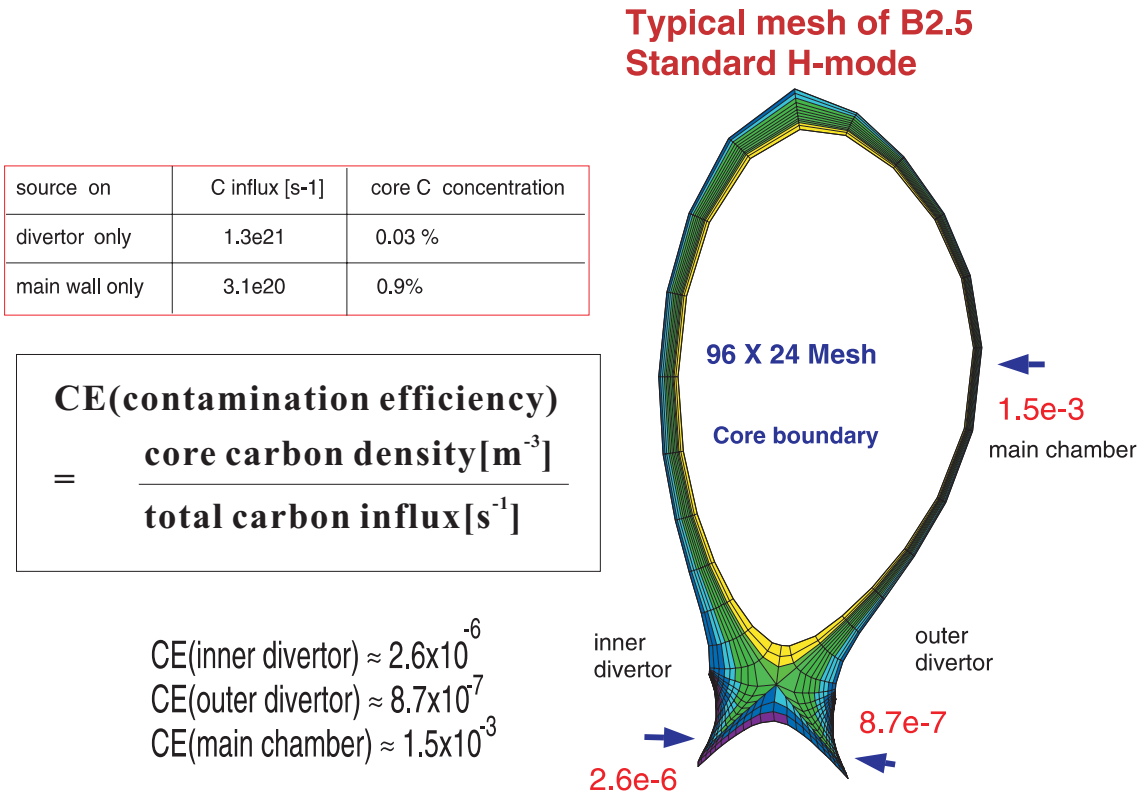

Figure 5.3: *The simulations of a standard H-mode : The contribution of the carbon influxes at the divertors and the main chamber. The results of the three separate simulations (Roth erosion rate applied only at the inner and the outer divertors and the main chamber, respectively). As shown in the table (left top), the total influxes from the divetors (the inner and the outer divertors) are higher than those from the main chamber. However, the contribution to the core concentration is higher for the main chamber carbon source.*

5.2 The Relative Contribution of the Carbon Influxes of the Inner Heat Shield and the Outer Protection Limiters to the Concentrations

As shown in the previous chapter, even in divertor tokamaks such as ASDEX Upgrade, the main chamber carbon sources are of primary concern rather than the divertor sources. This is due to the fact that the core carbon concentration is largely controlled by the main chamber sources. As mentioned in chap 2, the inner heat shield of ASDEX Upgrade is tungsten coated. However, according to the influx measurements, a significant fraction of the photon intensities comes from the heat shield. Therefore, the contribution of the carbon influx from the inner heat shield are necessary. In this

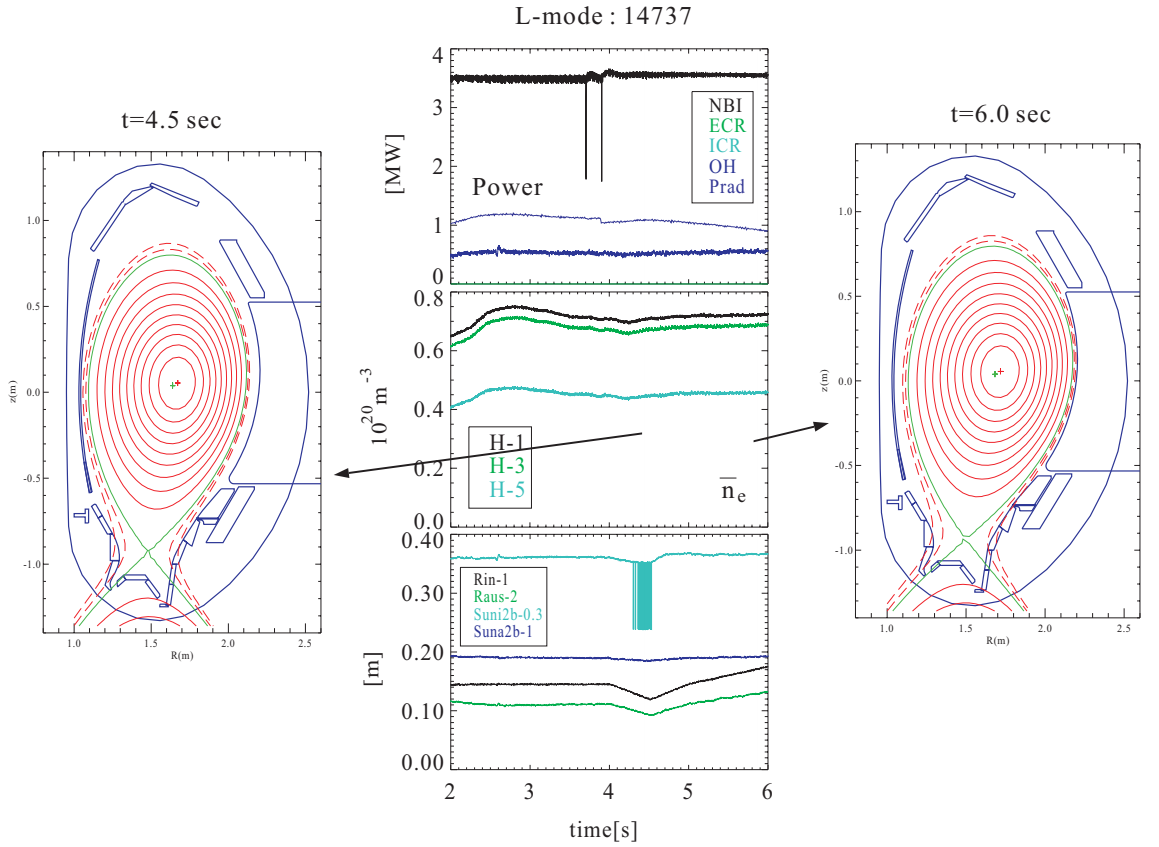

Figure 5.4: *The time trace of the plasma parameters of an L-mode (14737) discharge during the radial scans and the magnetic configurations of two extreme cases. At t=4.5[s], the plasma is shifted to the inner heat shield and at t=6.0[s], the plasma is shifted to the outer protection limiters. The input powers, the line averaged electron densities (center(H-1), middle(H-3), edge(H-5)), and the geometric parameters (R_{out}. R_{in}) are shown.*

chapter, consequently, the relation between the carbon sources from the main chamber and the core concentration are studied in more detail for typical L-mode and H-mode discharges.

The measured photon intensities are inherently line-of-sight integrated. To separate the contribution from the high field side (the inner heat shield) and the low field side (the guard or protection limiters), the radial shift of the magnetic configuration during a discharge is applied. In addition, Zeeman analysis[52] is also facilitated, when the measured spectral line permits. The actual magnetic configuration and the time trace of the plasma parameters are shown for L-mode (fig 5.4) and H-mode (fig 5.5) discharges, respectively. The plasma column is shifted along the radial direction approaching the inner heat shield and the outer protection limiters, as shown in the figures. During the

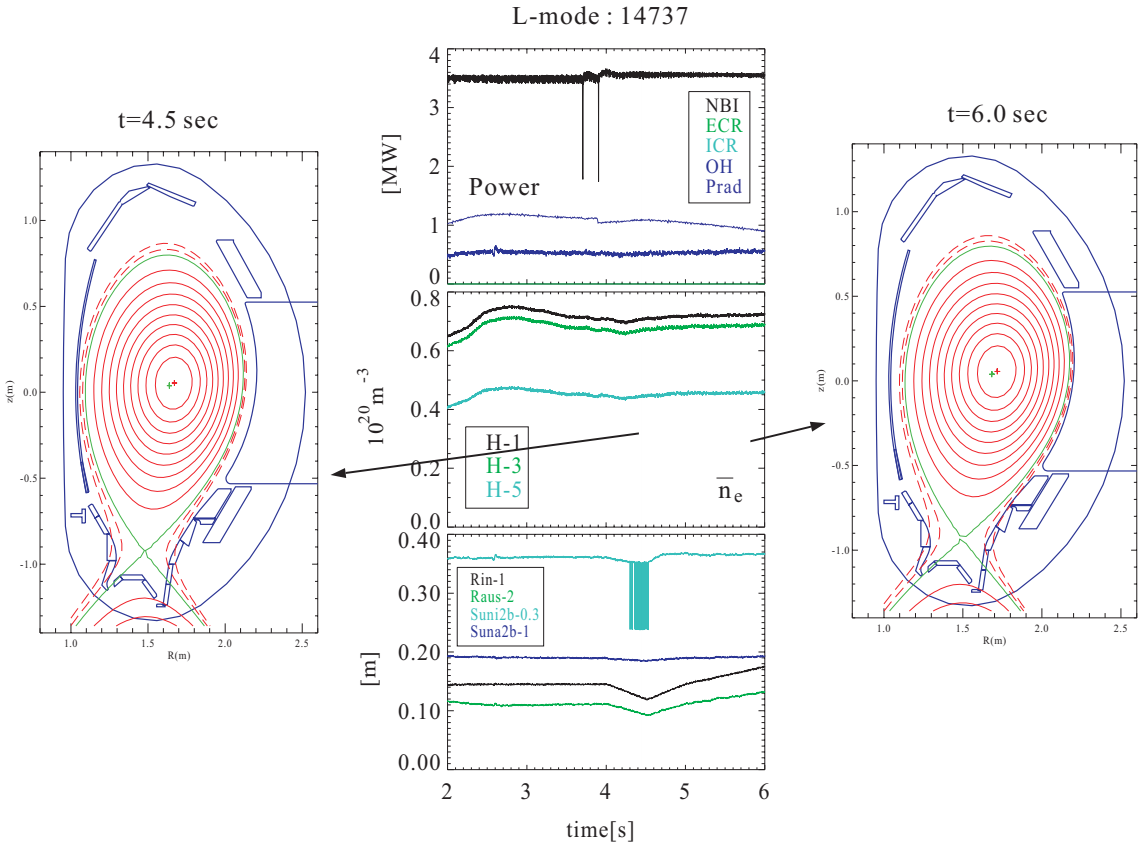

Figure 5.5: *The time traces of several plasma parameters of an H-mode (14918) discharge during the radial scans and the magnetic configurations of two extreme cases. At t=3.5[s], the plasma is shifted to the inner heat shield and at t=5.0[s], the plasma is shifted to the outer protection limiters. The input powers, the line averaged electron densities (center(H-1), middle(H-3), edge(H-5)), and the geometric parameters (R_{out}, R_{in}) are shown.*

magnetic scan, for both H-mode (from 3.5-5.0 sec) and for an L-mode (from 4.5-6.0 sec), the external heating powers and the line integrated electron densities are constant in time as shown in fig 5.4 and 5.5). Therefore, the effect of the variation of the atomic data (S/XB) on local T_e and n_e can be neglected. For both the L-mode and H-mode cases, the photon intensities of D_α and carbon lines increase linearly as the plasma is shifted to the inner heat shield.

The relation between the core carbon concentration and the influxes from the main chamber, i.e., the inner heat shield and the outer protection limiters, are shown in fig 5.6. The experimental signals are mapped to the corresponding radial coordinate (R_{out}) to identify the relative dependence of the data on the magnetic configurations. R_{out} is the position of the separatix at the outer midplane. D_α intensities are along

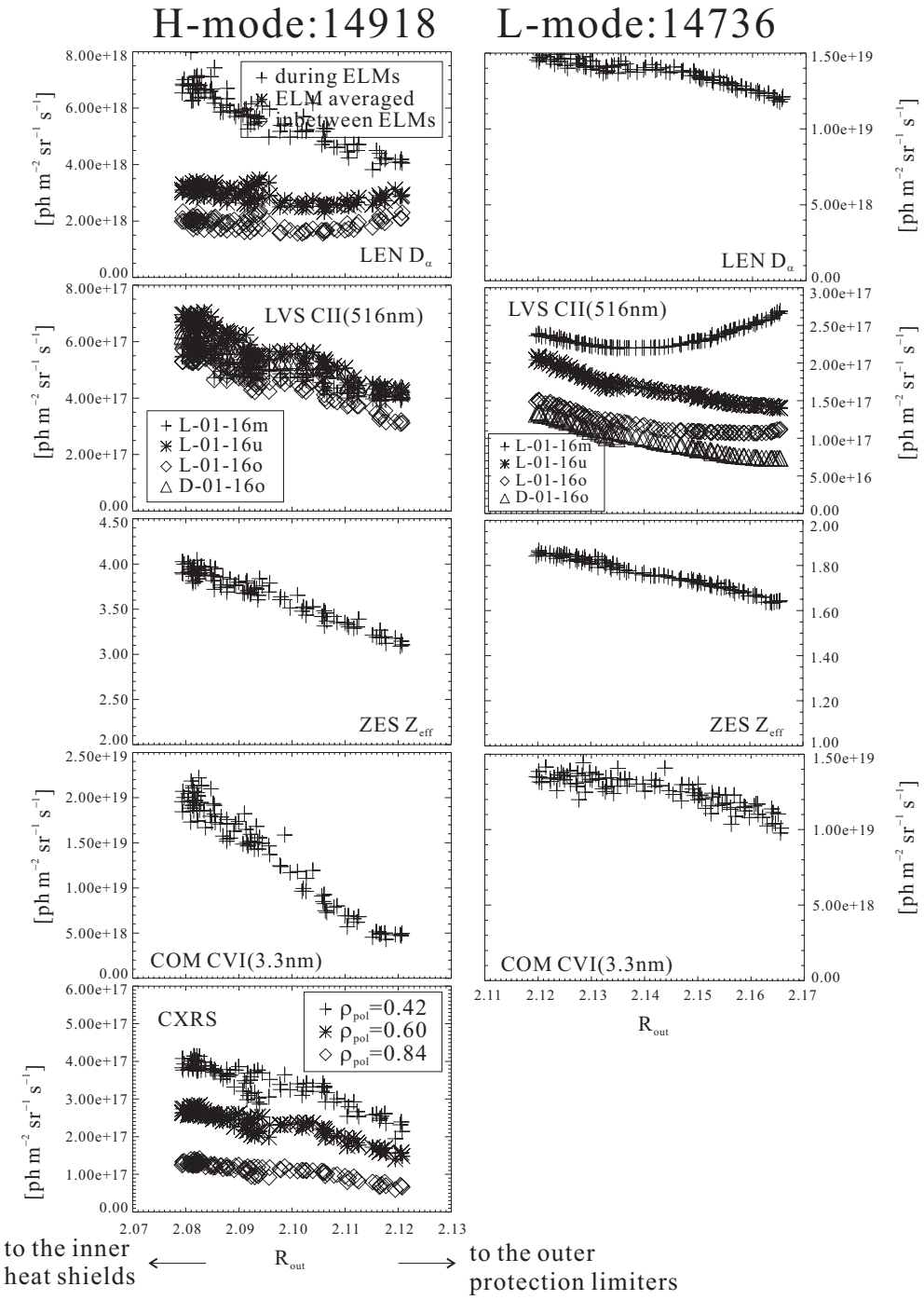

Figure 5.6: *The dependence of the photon intensities on the radial scans for both H-mode and L-mode is shown. The midplane D_α signals (for H-mode, ELM resolved), the CII (516nm) intensities along the midplane lines of sight (LVS), the Z_{eff} measurements of the core plasma, CVI (3.3nm) intensities and the charge exchange recombination spectroscopy (CXRS, CVI (529nm), n=8 to n=7) for three radial positions inside core, respectively.*

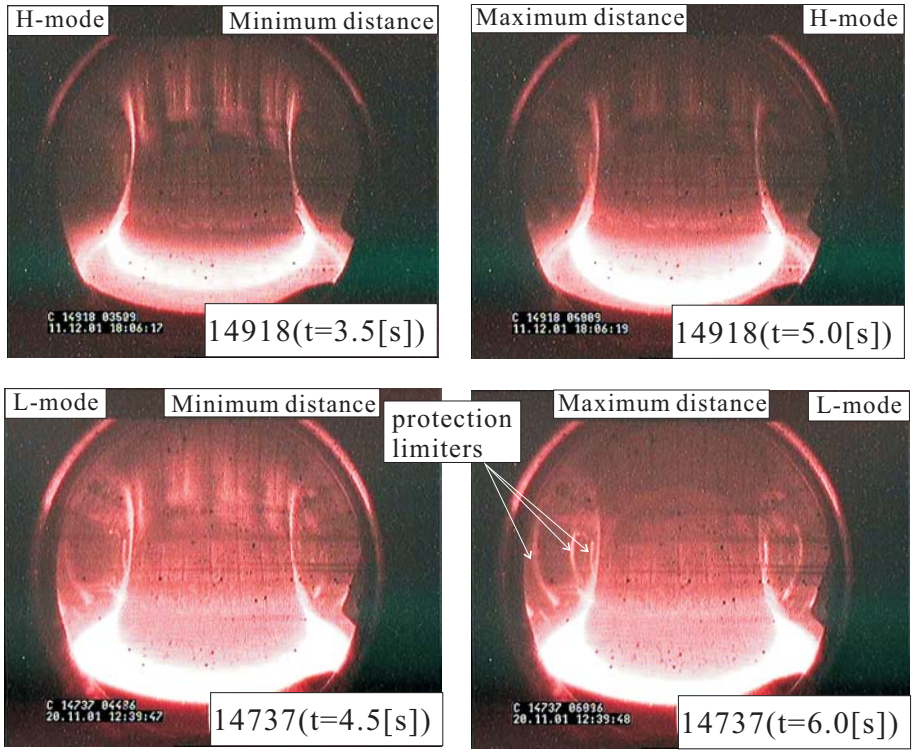

Figure 5.7: *The video CCD camera views of the discharges during the radial scans for both H-(14918) and L-modes(14737). The minimum and maximum distances are relative to the inner heat shield. These are in visible range and D_α mostly due to the fact that D_α is the most intense spectral line in the visible range.*

the midplane line of sight (3.4) and CII intensities are along the limiter lines of sight (3.4, 3.3). Z_{eff} is the effective charge of the plasma defined as

$$Z_{eff} = \sum_{z=1}^{\alpha} \frac{Z^2 n_z}{n_e} \tag{5.1}$$

where z is the index covering all ionization stages. Carbon is just one constituent and A carbon concentration of 1% increases Z_{eff} by 0.3. Z_{eff} is measured along the central part of the plasma. In case of charge exchange recombination spectroscopy (CXRS), the photon intensities are shown for three different radial coordinates in the core plasma. These intensities are proportional to the product of NBI neutral density and $C6+$ density along the line of sight. The photon intensities are emitted from the charge exchange process of $C6+$ with NBI D^0 (λ=529nm, the transition from n=8 to n=7) in this case. For a similar T_e and n_e, this photon intensity is a measure of the relative carbon density in the core plasma.

Both for H-mode and L-mode, the CII intensities along the limiter lines of sight increase as the plasma approaches the inner heat shield. With regard to the D_α signals

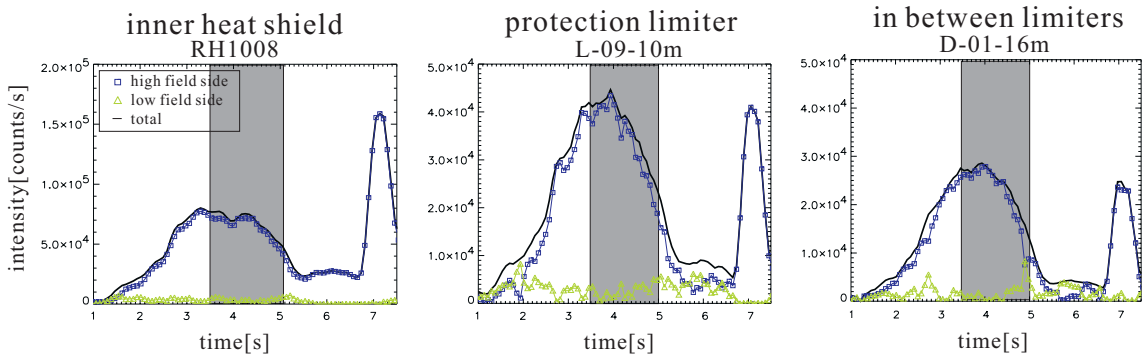

Figure 5.8: *Zeeman analysis of CIII 465nm of CDH spectrometer for discharge 14918. The grayed area is during the radial scan. For all the lines of sight, the contribution of the intensities from the low field side is negligible.*

along the midplane line of sight, there is a correlation between CII intensities and D_α intensities for the L-mode case. However, for the H-mode case, ELM averaged D_α is more or less constant during the R_{out} scans. This is due to the effect of the ELMs and will be discussed later in this chapter. As shown in fig 5.6, the CVI intensities show quite good correlations with CII intensities. Additionally, Z_{eff} and the photon intensity from charge exchange recombination spectroscopy (available only for H-mode) are shown. They follow the same dependence on R_{out} as the CVI intensities. As a result, for these discharges, the carbon influx from the inner heat shield is the dominant carbon source for the core concentrations. When the plasma approaches the outer protection limiters, the CII intensities of all midplane lines of sight decrease for H-mode. Also, for the case of L-mode, except for the middle line of sight (L-01-16m), the CII intensities decrease. The increase of CII along the sight line, L-01-16m, is probably due to the almost direct contact of the last closed surface on the middle part of the outer protection limiters, as is shown in fig 5.4.

In fig 5.7, the video CCD camera views of the plasma are shown for both H- and L-mode. For these cases, the intensities represent mainly D_α (656nm). For H-mode (14918), the change of intensities from the inboard to outboard sides during the radial sweep are negligible. The dominant fraction comes from the protection limiters for the H-mode. However, for L-mode, it can be clearly seen that the intensities from the central part of the protection limiters are increased at 6.0 sec when the plasma is moved close to the outer protection limiters, compared to the intensities at 4.5 sec when the plasma is moved close to the inner heat shield. These results are consistent with the results of the radial scan.

Also, in fig 5.8, the contribution of the intensities from the low and high field side are determined using Zeeman analysis of the CIII triplet system (465nm). The lines of sight considered are on the inner heat shield (RH1008), the middle part of the

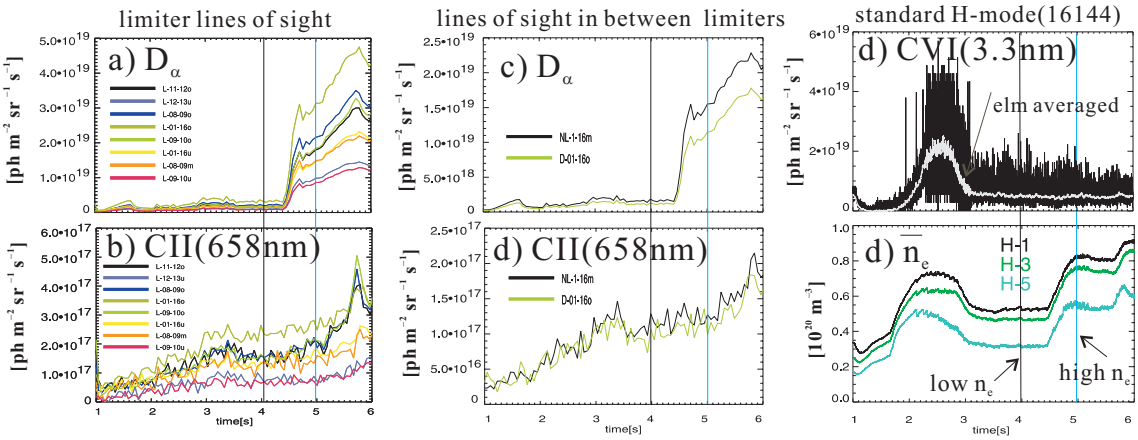

Figure 5.9: *The measured line integrated photon intensities along the limiter lines of sight (LVS) for both looking at the limiters and the areas in-between the limiters(H-mode, 16144). a)D_α and b)CII (658 nm) intensities at the lines of sights looking at the protection limiters. c)D_α and d)CII (658 nm) intensities at the lines of sights looking at the areas in-between limiters. e)CVI intensity along the vertical line of sight. ELM averaged signal is also shown for comparison. f) the line integrated electron density $\overline{n}_e$. At high density phase during the gas puff, D_α is increased at least by factor of 5 compared with the low density phase. On the other hand, CII intensities stay more or less constant.*

protection limiter (L-09-10m), and in between the limiters (D-01-16m). The positions of the lines of sight are shown in fig 3.4 and fig 3.3. As shown in fig 5.8, during the radial scan, the low field side contribution is less than 10% of the total intensities, even for the lines of sight on the protection limiter.

In summary, for typical plasma discharges, the carbon sources from the inner protection limiters are the dominant ones and exhibit good correlation with the core carbon concentrations.

5.3 The Density Dependence of the Carbon Influxes in Standard H-modes

In a standard H-mode, which is the reference discharge scenario of H-mode in ASDEX Upgrade, the carbon influxes from the inner heat shield and the protection limiters are measured along the main chamber lines of sight. In fig 5.9, the measured intensities and time traces of the plasma parameters are shown. When the low (without gas puff) and high (with gas puff) density phases are considered, the D_α intensities are increased by a factor of five at the high density phase compared to the low density phase due to the

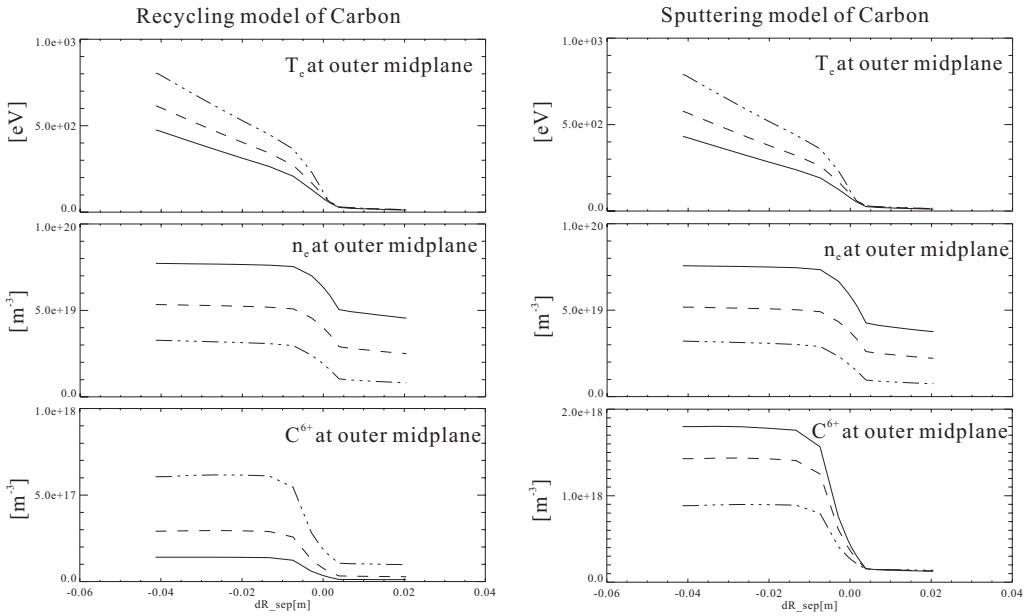

Calculated & experimental Line-integrated emissivities
along the main chamber chords(averaged)[ph m^{-2} sr^{-1} s^{-1}]

	Recycling model			Sputtering model			Experiment	
line	No gaspuff	Low gaspuff	High gaspuff	No gaspuff	Low gaspuff	High gaspuff	No gaspuff	High gaspuff
CII (658nm)	$2.2x10^{16}$	$0.7x10^{16}$	$2.5x10^{15}$	$3.9x10^{16}$	$8.5x10^{16}$	$1.5x10^{17}$	$1.0x10^{17}$	$1.2x10^{17}$
CVI (3.3nm)	$1.3x10^{18}$	$0.7x10^{18}$	$1.5x10^{17}$	$2.0x10^{18}$	$3.9x10^{18}$	$7.0x10^{18}$	$4.0x10^{18}$	$4.0x10^{18}$
D_α (656nm)	$2.3x10^{18}$	$5.9x10^{18}$	$9.5x10^{18}$	$2.3x10^{18}$	$5.9x10^{18}$	$9.5x10^{18}$	$2.2x10^{18}$	$1.3x10^{19}$

Figure 5.10: *The results of the simulations for the low and the high density phases of the standard H-mode. Three different densities are considered. Two different models are assumed for wall interactions, i.e., the recycling and sputtering models. T_e, n_e, and CVII densities are shown for three density cases. Also the line integrated photon fluxes are shown below for three density cases for two models. CII intensities are calculated along the limiter line of sight (the middle one) and D_α signals are along the midplane. Experimental data are also shown for comparison. See fig 3.4 for the detailed geometry of the lines of sight.*

increased recycling flux driven by the external deuterium gas puff. On the other hand, the CII intensities are more or less constant for both density phases. In addition, CVI intensity is also constant for both density phases. In this case, to relate these photon intensities to the corresponding influxes, it is necessary to evaluate the effect of the dependence of the atomic data (S/XB) on T_e and n_e.

To check the dependence of S/XB on the local T_e and n_e, B2.5 simulations have been carried out. Two models are considered for the wall interactions of carbon. The first model, called the recycling model in this study, is to assume that carbon sources come from the recycling process with the constant influxes from the protection limiters at the main chamber wall. This means the carbon neutral influxes are directly caused by the incident carbon ion fluxes at the inner heat shield. This situation is an approach to describe carbon sputtering on the tungsten coated inner heat shield. The second, named the sputtering model, assumes that carbon sources are from the erosion process with a fixed sputtering yield (1%). In this case, the carbon neutral influxes are caused by the background plasma ions (D^+). In fig 5.10, the results are shown for these two models. For the high density phases, according to the simulations, where n_e is increased by the gas puffing of the Deuterium neutrals at the edge, T_e is decreased inside the separatix but T_e at the outside is more or less unchanged. The change of T_e and n_e, including the increase of D^+ intensities, are the same for both models, which supposes the effect of carbon on the background plasma is negligible.

The S/XB dependence of the measured intensities are assessed as follows. As shown in fig 5.10 for the case of the sputtering model, CII intensity is increased proportionally to the increase of D_α, where carbon influxes are proportional to the deuterium outfluxes. The simulation shows the dependence of S/XB on T_e and n_e are negligible. Therefore, the measured carbon intensities at high density phase suggest similar carbon influxes compared to the influxes at the low density phase. We can rule out a strong effect of the S/XB dependence on T_e and n_e. The experimental CII intensities are quite reliably interpreted as the carbon influxes.

For the sputtering model, when the fixed sputtering yield is assumed, the simulations show an increase of the CII intensities along with D_α signals, which is inconsistent with the experimental data. The increase of CVI intensities are less pronounced compared to the CII intensities, mainly due to the increased screening effect of the high electron density. To be consistent with the experimental finding, a reduced sputtering yield during the high density phase is required with this model.

In case of the recycling model, on the other hand, a fixed influx from the protection limiters is used, where the measured value at the low density case is applied and the simulations show a decrease of the CII and the CVI intensities at the high densities, which is inconsistent with the experimental data. The simulations also underestimate the CII intensities at the main chamber compared to the experimental data. To be consistent with the experimental data, the increased influxes from the protection limiters at the high density phase are required. Yet in the low density phase, applying the

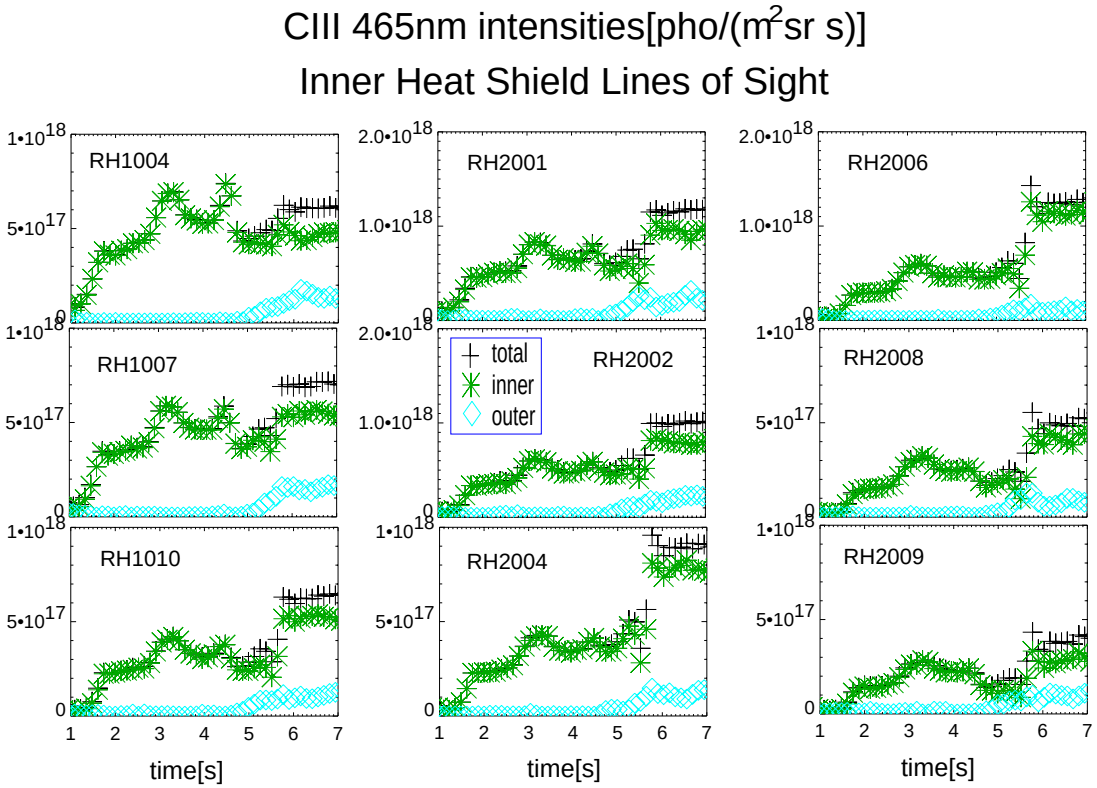

Figure 5.11: *The time trace of CIII (465nm) intensities from the inner heat shield lines of sight for H-mode (16144). The low (outer) and high (inner) field side fractions are from Zeeman analysis. The inner heat shield dominates the total intensity.*

experimental influxes from the protection limiters, 1% of core carbon concentration is predicted from the simulations, which is typical experimental level of carbon concentration. The recycling model for carbon has never been considered in the literature. However, as discussed in chap 2, the inner heat shield of ASDEX Upgrade tokamak is tungsten coated and therefore, this model seems more realistic than the sputtering model for the wall interaction at the inner heat shield.

In fig 5.11, the time traces of the CIII (465nm) intensities from the inner heat shield lines of sight for H-mode are shown. During the low density phase (t=2.0-3.5 sec), the contributions from the outer protection limiters (the low magnetic field side) are negligible compared with that of the inner heat shield (the high magnetic field side) for all lines of sight. This is the same results, discussed in the previous section. Yet, the fraction of the intensities from the low field side increases at high density phase. These lines of sight do not cover the limiter surfaces, but the increase of the intensities at the low field side suggests indirectly the increase of the intensities on the protection limiter surfaces. This means that at high density phase, the contribution of

the carbon influxes at the low field side increases. According to this experimental data, the recycling model with increased carbon influxes on the protection limiters is more favorable. The sputtering model does not match with this experimental data. But more experimental evidence is required. To understand the experimental behavior of the carbon influxes on the plasma density, a more sophisticated wall interaction model is required, assuming the recycling model for the inner heat shield and the sputtering model for the protection limiters.

In summary, it has been found that at the high plasma densities, the carbon influxes are not proportional to the deuterium influxes. This can be understood with the reduced sputtering yield for the sputtering model or the increased influxes at the protection limiters for the recycling model. However, according to the Zeeman analysis above, it can be concluded that judging from the experimental data at the high density phase, the combination of the recycling model for the inner heat shield and the sputtering model for the protection limiters is most reasonable candidate.

5.4 Effects of Edge Localized Modes on Carbon influxes

The improved confinement regime such as the H-mode is often perturbed by a quasi-periodic relaxation process involving bursts of MHD activity around the edge transport barrier and the consequent increase of D_α emission at the scrape-off layer, known as the edge localized modes (ELMs)[23, 22]. These lead to the rapid losses of energy and particles from the plasma boundary region and reduce the energy and particle confinement by 2-20%[53], depending on the type of ELM. Although these are efficient in removing plasma particles and impurities, these transient bursts of energy into the scrape-off layer can produce highly peaked heat loads at the divertor plates above the critical level the divertors can sustain. In addition, due to the high heat and particle loads at the main chamber components, the main chamber sources can be increased as well. In the following, effects of the type-I ELMs on the spectroscopic intensities, which are common type of ELMs for standard H-modes in ASDEX Upgrade, are discussed and B2.5 simulations of ELMs are carried out with simple assumptions.

As shown in fig 5.6 and 5.12, for H-mode during the radial plasma scan (discharge 14918), the ELM averaged intensities of D_α is more or less constant as the plasma moves to the protection limiters. Therefore, the ELM averaged D_α is not affected by the radial scan. However, the intensities from D_α during the ELM events follow the same trend as the ELM averaged CII intensities. Judging from this experimental result, D_α intensities during ELMs are closely correlated with the ELM averaged carbon intensities. Hence it strongly suggests the ELM averaged carbon influxes at the inner heat shield are dominated by the wall interactions during ELMs. However, the measurement of the carbon intensities with a high temporal resolution are not available at

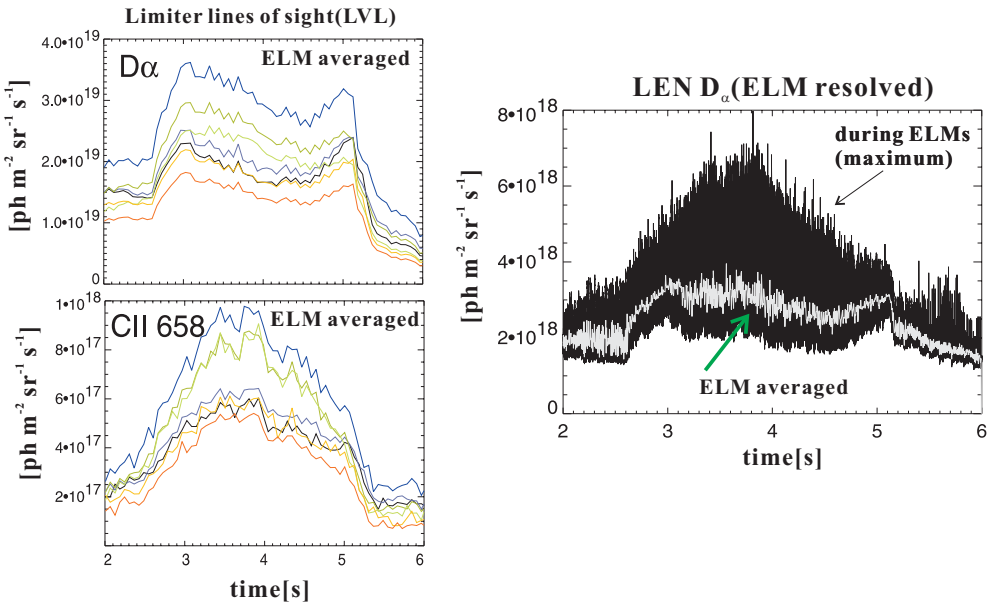

Figure 5.12: *The time traces of the spectroscopic line intensities during the radial magnetic scan in H-mode (discharge 14918). Due to the low sampling rate of the spectrometer, the intensities (D_α, CII) from the limiter lines of sight (left) are not ELM-resolved. D_α from the midplane LENA is ELM resolved (right). There is a strong correlation between the ELM resolved D_α and the ELM averaged CII (658nm) intensities.*

the main chamber due to the low intensities compared to the divertor conditions and thus a direct comparison of the intensities (D_α and CII) during ELMs will be studied in near future.

For an estimate of the intensity fractions, during and in-between ELMs, time dependent B2.5 simulations are carried out. To simulate an ELM in a typical H-mode, at the onset of an ELM event (for $100\mu s$), the transport coefficients at the pedestal region are increased by a factor of 100. Also, the computational mesh is extended further to the core region to match the collapse of T_e and n_e at the core edge correctly. For realistic simulations, the determination of the steady-state solution is prerequisite. In fig 5.13, the steady-state fits of D and χ are shown with corresponding T_e and n_e profiles. For the ELM simulation, fast reflectometry[53] is used for n_e profile at the outer midplane. The mismatch of the density data around the pedestal top, suggested by reflectometry at the high and the low field sides, is not supposed to be real in the presence of fast parallel transport. In fig 5.14, the comparison of the measured D_α and the fitted D_α are shown. In addition, the time traces of n_e profiles both at the inner and the outer midplane as a function of the radial coordinate ρ_{pol} (see Appendix C).

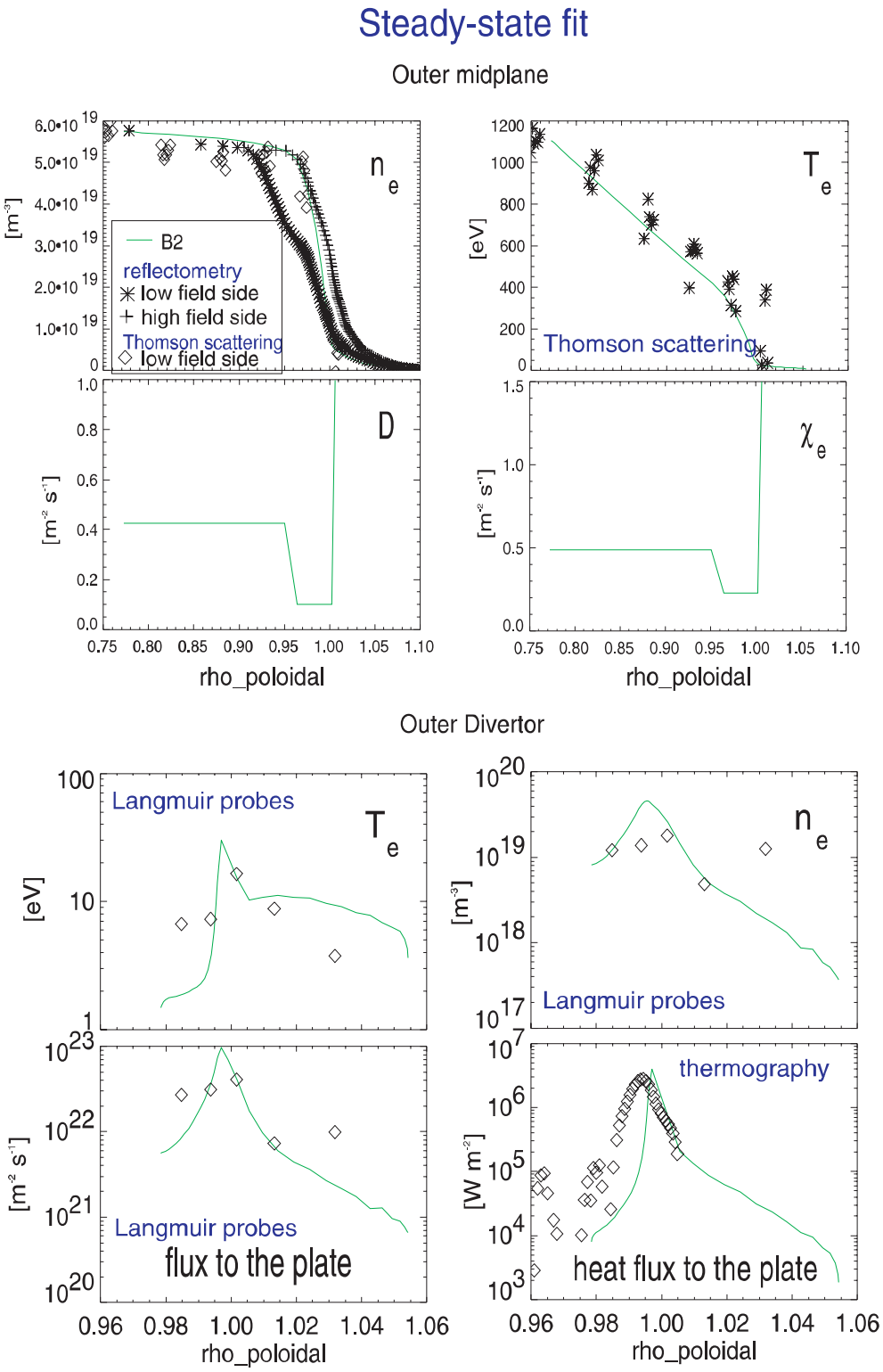

Figure 5.13: *The fit of the steady-state plasma used as the initial plasma for ELM simulations. n_e from Thomson scattering and reflectometry is compared. For the outer divertor, the Langmuir probes and thermography data are compared with the simulations. In the figure, all radial coordinates are mapped into the outer midplane (ρ_{pol}).*

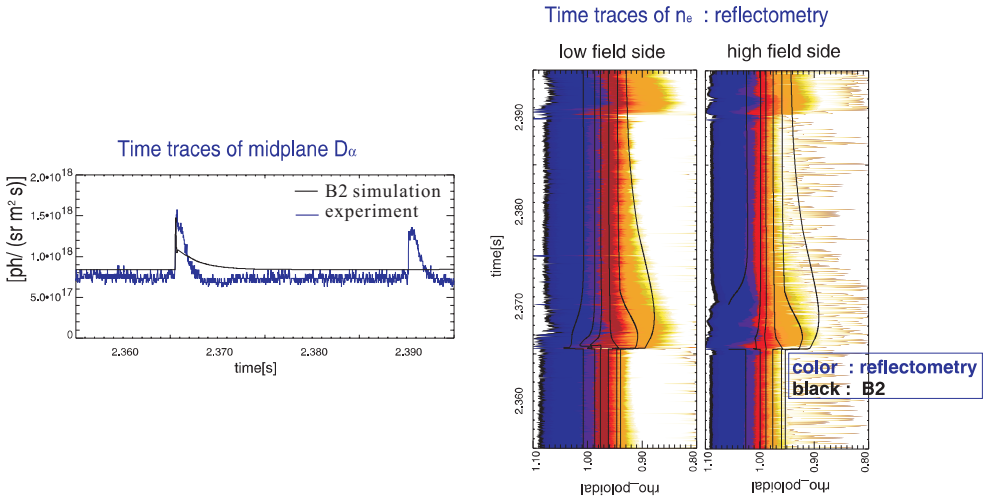

Figure 5.14: *The time dependence of n_e profiles both at the outer and the inner midplane are shown. The simulation and reflectometry data are compared on the right. The midplane D_α is also shown on the left.*

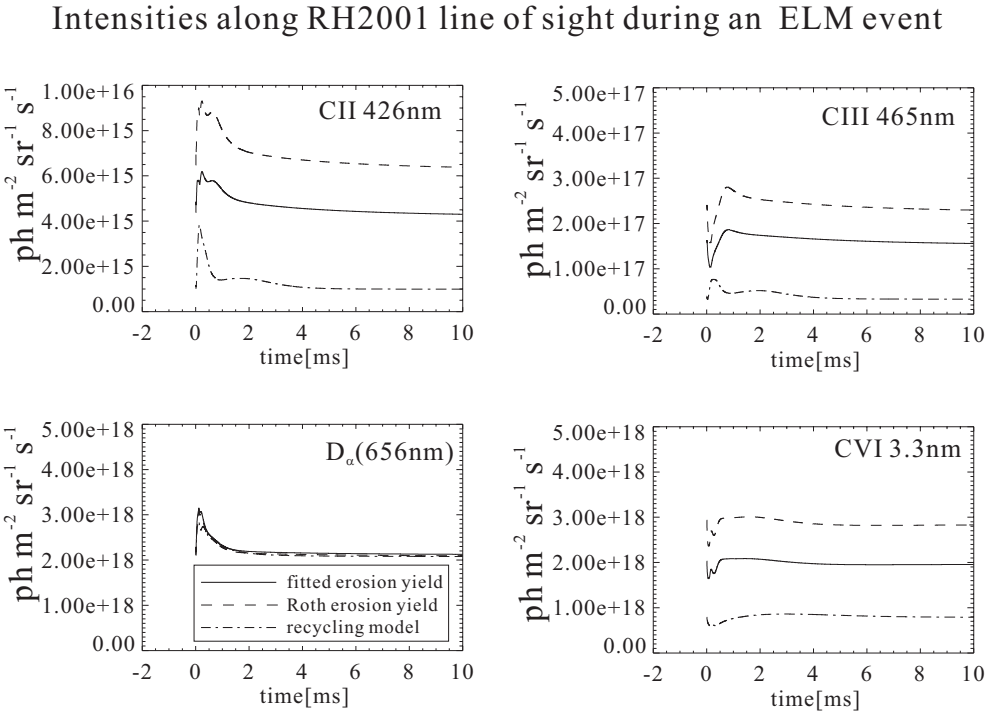

Figure 5.15: *The photon intensities along the central heat shield line of sight calculated from the simulations. Compared to D_α, CII and CIII intensities are in slow time scale to relax to the steady state levels. At time t=0[ms], ELM is triggered.*

6

Summary and Outlook

The control of impurities in a tokamak plasma is one of the critical issues for the success of a fusion reactor. Carbon is the major impurity species in present tokamaks plasma including ASDEX Upgrade. A smaller fraction of the first wall is expected to be covered with carbon in ITER. The final choice of its first wall composition will still be influenced by present day experiments and the first operational phase of ITER. Understanding carbon transport in the edge of tokamak plasmas is critical for estimations of the global carbon content in the plasma. Major carbon sources in ASDEX Upgrade are the inner heat shield, the protection limiters, and the divertors mainly via chemical erosion. In this study, the relation of the core carbon concentration and the carbon influxes at the above mentioned plasma facing components has been analyzed.
Due to the complex wall structure and the complicated particle transport in the edge of tokamak plasmas, the following methods are utilized. First, Optical emission spectroscopy is applied for characterising the sources, i.e., the influxes of carbon and the background plasma at the main chamber and the divertors. In addition, for the localization of the carbon influxes from the main chamber, Zeeman analysis is used and the contributions of the high and the low magnetic field sides are resolved. Second, soft X-ray spectroscopy and visible bremsstrahlung measurements are used to determine the core carbon concentrations. Third, the two dimensional edge plasma transport code(B2.5) is used for interpretation of the experimental data and the predictive tests of the assumed models for carbon transport. A fit routine to extract the transport coefficients has been also developed.

The core carbon concentrations correlate with the main chamber fluxes in ASDEX Upgrade. The contribution of divertor carbon sources to the core carbon concentrations is small due to the low penetration probability. This is concluded from the following analysis. First, analytic calculations of the ion parallel transport of the divertor carbon sources show that the divertor carbon influxes are effectively retained in the divertor region due to the dominance of the friction force on carbon exerted by the background deuterium plasma. Second, an experimental database has been set up for the corre-

lation between the carbon concentration and the carbon influxes. The carbon sources from the main chamber shows a better correlation with the concentrations. Third, B2.5 simulations for penetration probability of carbon are carried out. The total amount of carbon influx is higher at the divertors due to the concentrated plasma surface interactions. However, due to the very low penetration probability, the contribution of the divertor sources to the core concentration is small, less than 10%.

Among the main chamber sources, the high field side, i.e., the inner heat shield, is the major source for carbon influx in ASDEX Upgrade, despite tungsten coating. The dominance of high field side carbon erosion, obtained by Zeeman spectroscopy, is corroborated by experiments with the radial magnetic shift. The carbon influx at the high field side is interpreted as deposition and re-erosion of deposited carbon.

The radial transport coefficients in the edge plasma are determined using the developed B2.5 fit routine. Reduced transport coefficients over the edge transport barrier region are necessary to re-construct the pedestal structure in the electron temperature and density profiles at the outer midplane. When the same D and χ are assumed for the plasma and carbon species, a strong inward pinch ($\sim 15 m^2/s$) is necessary for carbon ions to match the soft-X ray measurements with the given influxes from the main chamber. This pinch velocity is expected to consist of a neoclassical contribution, based on collisions and anomalous part which mainly be a feature of drift wave turbulence in the edge plasma[54].

Based on the results of this work, further studies are suggested as follows.

- For a quantitative analysis of the edge localized mode on the erosion process, the carbon intensities (CII, CIII) have to be measured with high temporal resolution.
- Parameter dependence of the edge carbon transport: the effect of heating power, electron density, triangularity and so on.
- Comparison with the carbon transport in other tokamaks and thereby prediction of carbon concentrations in ITER tokamak.
- Refinement of the B2.5 fit routine and inclusion of other data, allowing to set up a database for the parameter dependence of edge carbon transport.
- Carbon erosion yield model for a tungsten surface.

Appendix A

Calibration Procedure for the Spectroscopic Measurement Systems

The absolute in-vessel calibrations of spectrometers are performed using visible photon sources with the known spectral radiance[$Wm^{-2}sr^{-1}nm^{-1}$], such as the lab-rod and lab-sphere. For the flexible connection of each detector system to each line of sight, all detectors can share the lines of sight using a switching board installed in the outside of the torus. The effective acceptance angle of the total measurement system is limited by the component with the narrowest acceptance angle, which is in this setup the focusing mirror of the lines of sight located inside the torus. The sensitivities of the detectors and the lines of sight are calibrated independently of each other. Hence independent calibration procedure is possible for the detectors and for the attenuation of lines of sight including the reflectivity of the mirrors installed in front of the sight line in the torus. The calibration of the systems is performed separately for the detectors and the lines of sight to allow to calculate calibration factors of different combinations of lines of sight and detectors.

A.0.1 Sensitivity of the Detectors (Spectrometers)

Sensitivity of the detectors (CDL, CDH, VSL, VSM, ...) can be determined through calibration with an intensity source in the visible range with the known spectral radiance. The sensitivity of a detector is described as a parameter, F_{cal}, the calibration factor. This is formulated as follows:

$$F_{cal} \equiv I_{sor}/C_{sor} \tag{A.1}$$

where F_{cal} is the calibration factor of the detector, I_{sor} is the spectral radiance of the source in units of $[Wm^{-2}nm^{-1}sr^{-1}]$ and C_{sor} is the actual measured counts with a background correction of the source intensity from the detector in units of $[counts\, m^{-2}\, pixel^{-1}\, s^{-1}]$. For this purpose, a lab-rod and a lab-sphere are used as the sources. A typical procedure for VSL using the lab-sphere is shown in fig A.1.

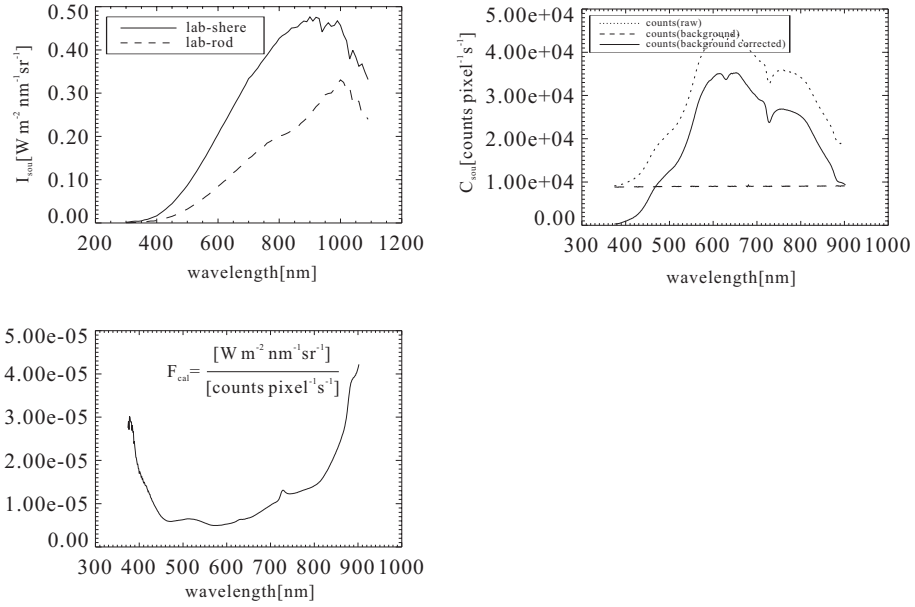

Figure A.1: *Spectral radiance of the sources (rod and sphere), the measured counts and the calculated calibration factor of VSL.*

In addition, linearity of the detectors is checked with variations of the exposure time and using attenuation filters.

A.0.2 The Attenuation of Fibers

For assessing neutron damage and the coating effect of the lines of sight systems, during every opening of the torus, the in-vessel calibration has been repeated. For convenience, the low-resolution mini-spectrometer (VSL) was used, which covers all the whole visible range with $\Delta\lambda \sim 1nm$. The basic procedure is to use a photon source with the known spectral radiance and comparing the sensitivity of both the detector only and detector plus a line of sight in concern. The attenuation level of a line of sight can be described with the attenuation factor (F_{att}), which is defined as follows:

$$F_{att} \equiv C_{board}/C_{torus} \tag{A.2}$$

where F_{att} is the dimensionless attenuation factor, C_{board} is the measured intensity ($[counts\ m^{-2}\ pixel^{-1}\ s^{-1}]$) of the sources from the switching board, and C_{torus} is the measured intensity ($[counts\ m^{-2} pixel^{-1}\ s^{-1}]$) of the sources from the torus. In fig A.2, the attenuation factors calculated with the different detectors are compared. There is a discrepancy between CDL and VSL at low wavelength range (below 430nm) probably caused by the low signal-to-noise ratio of VSL. However, for the higher wavelength range, the two factors are in agreement within 10%. Hence this confirms that the line

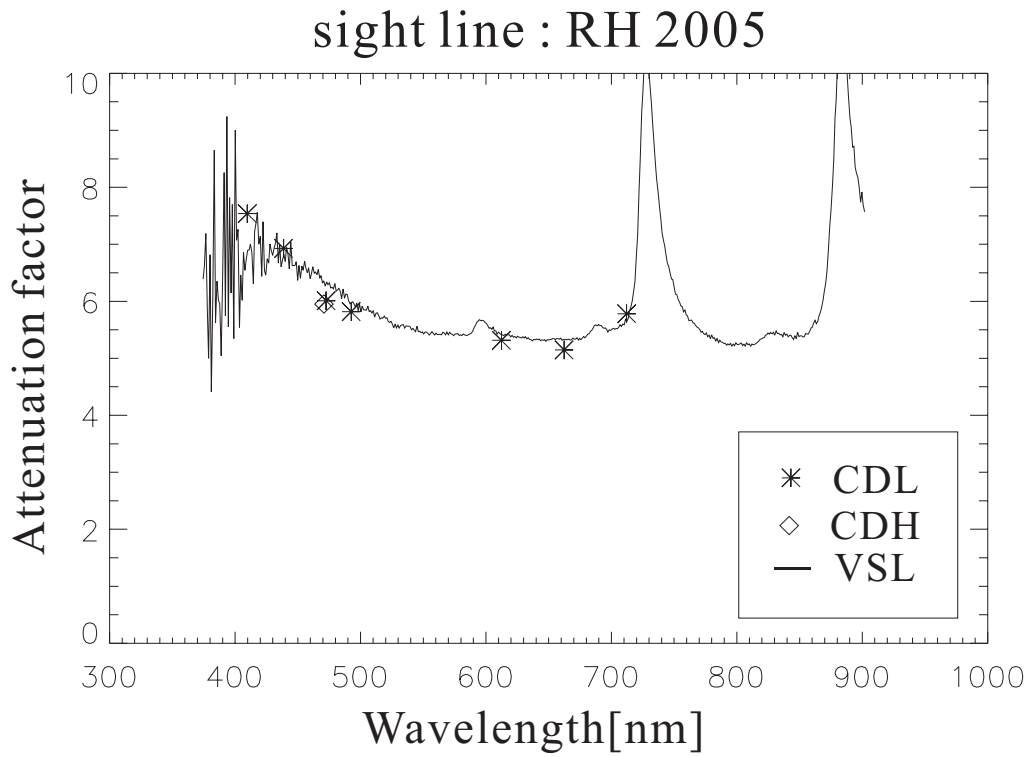

Figure A.2: *Comparison of the calculated attenuation factor for a line of sight from CDL, CDH and VSL, as a cross-check of the calibration procedure with the independent* F_{spec} *and* F_{fiber}*. The discrepancy below 430nm is supposedly due to the low signal-to-noise ratio of VSL.*

of sight causes the limiting acceptance angle and applying the same attenuation factor, independent of the detector, is reasonable.

For another test of the validity of the calibration procedure, two calibration procedures are compared. One is the separate calibration of lines of sight and detectors and the other is direct calibration of the system from the torus to the detectors. As shown fig A.0.3, the CIII photon intensities are compared for two calibration procedures in a discharge (shot number : 15013). The intensities along the two adjacent lines of sight, which is separated about 5 centimeters along the inner heat shield, is expected to be very similar. The comparison shows that the difference between two calibration procedures is small, less than 10%.

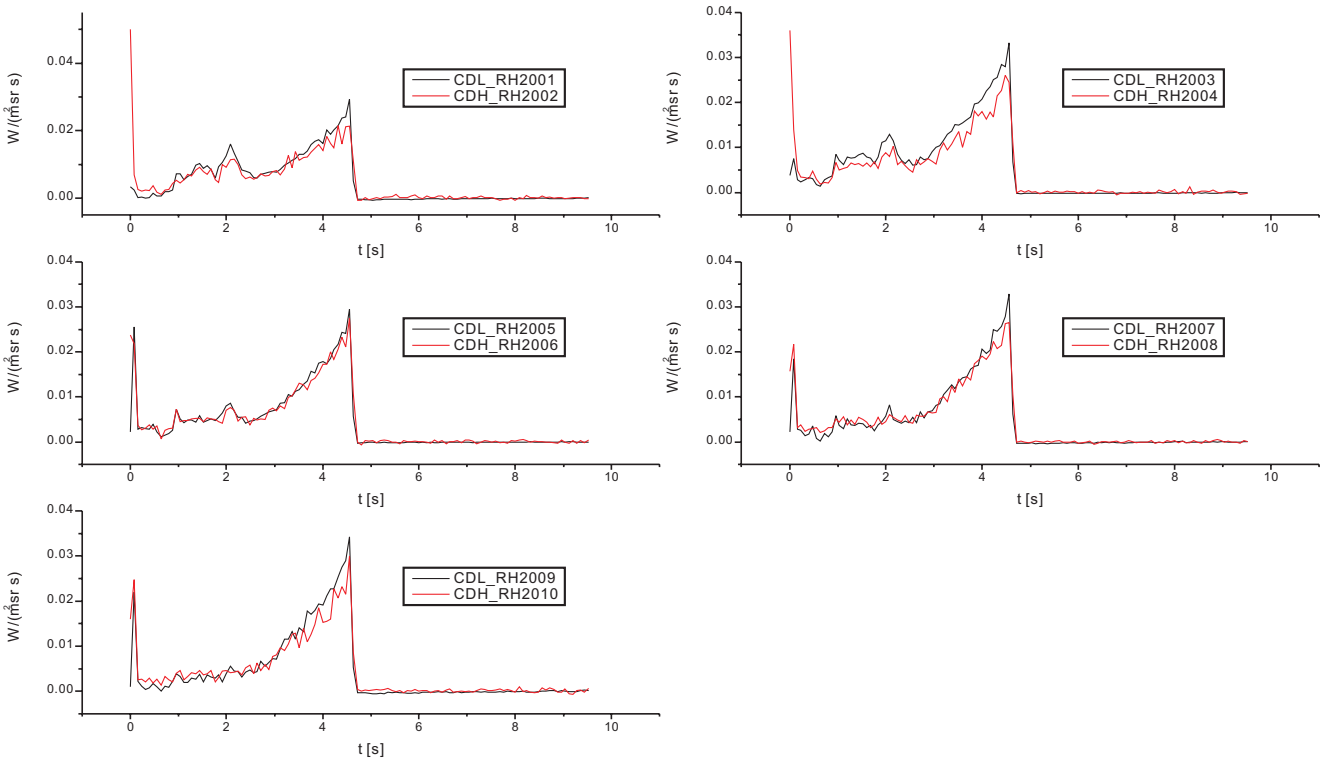

Figure A.3: *Comparison of the calibrated line intensities (CIII 465nm) measured at similar positions at the inner heat-shield from two different spectrometers, CDL and CDH, as a cross-check of calibration procedure (shot number:15013). In case of CDL, calibration factors for the lines of sight and the detector are applied separately. On the other hand, for CDH, the total calibration factor is applied, measured directly from the torus to the detector.*

A.0.3 Calibration of the Measured Photon Intensity

With the calibration factors (F_{cal}) and the attenuation factors (F_{att}), the measured experimental signal can be calibrated with the following relation:

$$I_{cal} = \int_{\lambda_1}^{\lambda_2} F_{att}(\lambda) \cdot F_{cal}(\lambda) \cdot C_m \tag{A.3}$$

where $I_{cal}[Wm^{-2}nm^{-1}sr^{-1}]$ is the calibrated photon flux of the spectral line in concern, C_m is the measured counts of a detector and λ_1,λ_2 are the wavelength range of the spectral line.

Appendix B

The governing equations of B2.5

In general, as already derived by Braginskii[55], a plasma state can be described by the Boltzmann equation coupled with Maxwell equations. For a distribution function $f = f(\mathbf{r}, \mathbf{v}, t)$ of each plasma species,

$$\frac{\partial f}{\partial t} + \mathbf{v} \cdot \frac{\partial f}{\partial \mathbf{r}} + \frac{Ze}{m} (\mathbf{E} + \mathbf{v} \times \mathbf{B}) \cdot \frac{\partial f}{\partial \mathbf{v}} = \left(\frac{\partial f}{\partial t} \right)_c \tag{B.1}$$

The first three velocity moments of this equation lead to a set of fluid equations applying the relevant closure to truncate the infinite chains of the moment equations. In this chapter, two-dimensional fluid equations of B2.5 are described for a divertor tokamak geometry (fig4.1) following Braginskii's analysis.

The general fluid formulation of the plasma can be formulated using the first three velocity moments of the kinetic equation. The following equations are for electron and ion species. For toroidal geometry, metric coefficients $h_r = 1/|\nabla r|$, $h_\theta = 1/|\nabla_\theta|$, $\sqrt{g} = 2\pi R h_r h_\theta$ are introduced where R is the local major radius of a tokamak.

The particle balance can be formulated as follows from the first moment of the kinetic equation.

$$\frac{\partial n_i}{\partial t} + \nabla \cdot (n_i \mathbf{v}_i) = K_{i-1}^{ion} n_e n_{i-1} - K_i^{rec} n_e n_i \tag{B.2}$$

where subscripts e,i are for electron and ion with ionization stage i, and n, $\mathbf{v}$ are density and velocity. The right hand side represents the source and sink terms from ionization and recombination processes, where K^{ion}, K^{rec} are the ionization and the recombination rate coefficients. For electron density, $n_e = \sum_{i=1}^{Z} n_i$ (quasi-neutrality) is assumed, which is valid for low-frequency transport time scales.

The parallel momentum balance can be formulated for ions and electron as follows:

$$\frac{\partial n_i m_i v_\parallel}{\partial t} + \nabla \cdot \left(n_i m_i v_\parallel \mathbf{v}_i \right) = -\nabla_\parallel P_i + Z e n_i E_\parallel - F_{i\parallel} - R_{i\parallel} + S_i^m \tag{B.3}$$

$$0 = -\nabla_\parallel P_e - e n_e E_\parallel - R_{e\parallel} \tag{B.4}$$

where the subscript e is the electron, $\|$ denotes the vector component parallel to the magnetic field. m,e,Z are the mass , the electron charge, and the ionization state, respectively. The pressure is $P = nT$ and $F_{i\|} = (\nabla \cdot \Pi)_{\|}$ is the viscous force parallel to the magnetic field. R, S_i^m are the friction force and the momentum source, respectively. For electrons, the equation is simplified because one may neglect the inertial terms and viscosity owing to the small electron mass. Because of the strong B-field, the velocity perpendicular to B can usually be well approximated by algebraic relations involving the other variables using reduced momentum equations that neglect inertia and viscosity. In the simplest version, which is used in this thesis, the classical diamagnetic and $\mathbf{E} \times \mathbf{B}$ plasma drifts are neglected. Thus, the poloidal ion velocity is just the projection of parallel velocity ($v_\theta = v_\| B_\theta / B$). The radial velocity is believed to be driven substantially by plasma micro-turbulence and a anomalous transport ansatz is used,

$$v_{ri,re} = -\frac{D_a}{n_{i,e}} \nabla_r n_{i,e} + v_{ai,ae} \tag{B.5}$$

where D_a, v_a are the anomalous (mainly turbulence driven) diffusion coefficient and velocity.

The energy balance for electrons and ions are given below from the third moment of the kinetic equations:

$$\begin{aligned} &\tfrac{\partial}{\partial t}\left(\tfrac{3}{2} n_{i,e} T_{i,e}\right) + \nabla \cdot \tfrac{3}{2}\left(n_{i,e} \mathbf{v}_{i,e} T_{i,e}\right) + n_{i,e} T_{i,e} \nabla \cdot \mathbf{v}_{i,e} \\ &= -\nabla \cdot \mathbf{q}_{i,e} - \Pi_{i,e} : \nabla \mathbf{v}_{i,e} + Q_{i,e} + S_{i,e}^E \end{aligned} \tag{B.6}$$

where $\mathbf{q}_{i,e}$ are heat fluxes and $Q_{i,e}$ is the heat transfer between electrons and ions.

The validity of the fluid equation description requires that the radial plasma scale length (Δr) is much larger than the ion gyro radius ($\rho_i = m_i v_{th}/eB$), where $v_{th} = (2T_i/m_i)^{1/2}$ is the ion thermal velocity. In addition, the parallel connection length ($L_\|$) between the midplane and the divertor plate or characteristic scale length must be larger compared to the collisional mean-free-path (λ_c). For a coulomb collision,

$$\lambda_c \approx T^2/n \tag{B.7}$$

where λ_c, T, and n are in units of [m], [eV], [$10^{16} m^{-3}$] respectively. Because high energy particles are the main contributors to the parallel thermal transport, the collisional thermal transport becomes inaccurate for the condition $\lambda_c \geq L_\|$. This is the most common breakdown in the validity condition for the fluid description. For the low-collisionality regime, a reasonable correction for kinetic effects is to reduce the parallel diffusive heat flux to $\alpha n v_{th} T$, where α is the flux-limiting factor and has an approximate value, 0.15, according to kinetic simulations[56]. This reduction applies for both electrons and ions.

As a consequence, the full fluid transport equations can be formulated in toroidal geometry as follows. The continuity equation for atomic species i is:

$$\frac{\partial n_i}{\partial u}+\frac{1}{\sqrt{g}}\frac{\partial}{\partial x}\left(\frac{\sqrt{g}}{h_x}\Gamma_{ix}\right)+\frac{1}{\sqrt{g}}\frac{\partial}{\partial y}\left(\frac{\sqrt{g}}{h_y}\Gamma_{iy}\right)=K_{i-1}^{ion}n_e n_{i-1}-K_i^{rec}n_e n_i \tag{B.8}$$

The expressions of the particle fluxes are

$$\begin{aligned}\Gamma_{ix}&=\left(u_{ix}^{anom}+u_{\|i}\frac{B_x}{B}\right)n_i-D_i^n\frac{1}{h_x}\frac{\partial n_i}{\partial x}-D_i^p\frac{1}{h_x}\frac{\partial p_i}{\partial x}\\ \Gamma_{iy}&=u_{iy}^{anom}n_i-D_i^n\frac{1}{h_y}\frac{\partial n_i}{\partial y}-D_i^p\frac{1}{h_y}\frac{\partial p_i}{\partial y}\end{aligned} \tag{B.9}$$

where D_i^n and D_i^p are the anomalous transport coefficients. u_{iy}^{anom} and u_{ix}^{anom} are the additional anomalous velocities.

The parallel momentum balance equation for atomic species i is:

$$\begin{aligned}&\tfrac{\partial}{\partial t}\left(m_i n_i u_{\|i}\right)+\tfrac{1}{\sqrt{g}}\tfrac{\partial}{\partial x}\left(\tfrac{\sqrt{g}}{h_x}\Gamma_{ix}^m\right)+\tfrac{1}{\sqrt{g}}\tfrac{\partial}{\partial y}\left(\tfrac{\sqrt{g}}{h_y}\Gamma_{iy}^m\right)=\\ &-\tfrac{B_x}{B}\left[\tfrac{1}{h_x}\tfrac{\partial}{\partial x}\left(n_iT_i\right)+\tfrac{Z_in_i}{n_e}\tfrac{1}{h_x}\tfrac{\partial}{\partial x}\left(n_eT_e\right)\right]+\\ &\sum_j f_{ij}\left(u_{\|j}-u_{\|j}\right)+en_e\tfrac{B_x}{B}\hat{E}_xZ_in_i\left(\tfrac{1}{n_e}-\tfrac{Z_i}{\sum_i Z_i^2n_i}\right)+S_i^m\end{aligned} \tag{B.10}$$

where f_{ij} is the classical friction coefficient. The modified electric field ($\hat{E}_x$) is

$$\hat{E}_x=\frac{1}{en_e}\frac{1}{h_x}\frac{\partial p_e}{\partial x}-\frac{1}{h_x}\frac{\partial\phi}{\partial x} \tag{B.11}$$

where ϕ is the electric potential which is governed by charge conservation equation ($\nabla\cdot J=0$). The expression of the momentum flux are

$$\begin{aligned}\Gamma_{ix}^m&=m_i\Gamma_{ix}u_{\|i}-\eta_{ix}\tfrac{1}{h_x}\tfrac{\partial u_{\|i}}{\partial x}\\ \Gamma_{iy}^m&=m_i\Gamma_{iy}u_{\|i}-\eta_{iy}\tfrac{1}{h_y}\tfrac{\partial u_{\|i}}{\partial y}\end{aligned} \tag{B.12}$$

where $\eta_{ix,iy}$ is the viscosities. The electron and ion heat balance equations are

$$\begin{aligned}&\tfrac{\partial}{\partial t}\left(\tfrac{3}{2}n_eT_e\right)+\tfrac{1}{\sqrt{g}}\tfrac{\partial}{\partial x}\left(\tfrac{\sqrt{g}}{h_x}Q_{ex}\right)+\tfrac{1}{\sqrt{g}}\tfrac{\partial}{\partial y}\left(\tfrac{\sqrt{g}}{h_y}Q_{ey}\right)=\\ &-\tfrac{1}{h_x}\tfrac{\partial u_{ex}}{\partial x}n_eT_e+J_x\hat{E}_x+J_y\hat{E}_y-k_{ei}\left(T_e-T_i\right)+S_e^H\\ &\tfrac{\partial}{\partial t}\left(\tfrac{3}{2}\sum_i n_iT_i\right)+\tfrac{1}{\sqrt{g}}\tfrac{\partial}{\partial x}\left(\tfrac{\sqrt{g}}{h_x}Q_{ix}\right)+\tfrac{1}{\sqrt{g}}\tfrac{\partial}{\partial y}\left(\tfrac{\sqrt{g}}{h_y}Q_{iy}\right)=\\ &-\sum_i\tfrac{1}{h_x}\tfrac{\partial u_{ix}}{\partial x}n_iT_i+\sum_i\eta_{i\|}\left(\partial_\|u_{\|i}\right)^2+\sum_i F_{ij}\left(u_{\|j}-u_{\|i}\right)+k_{ei}\left(T_e-T_i\right)+S_i^H\end{aligned} \tag{B.13}$$

where $k_{ei}\left(T_e-T_i\right)$ is the heat exchange and S_i^H, S_e^H are heat sources. F_{ij} is the friction force. The expression of the electron and ion heat fluxes are

$$\begin{aligned}Q_{ex}&=\tfrac{3}{2}\Gamma_{ex}T_e-\kappa_{ex}\tfrac{1}{h_x}\tfrac{\partial T_e}{\partial x}+\alpha_{ex}T_e\widehat{E_x}\\ Q_{ey}&=\tfrac{3}{2}\Gamma_{ey}T_e-\kappa_{ey}\tfrac{1}{h_y}\tfrac{\partial T_e}{\partial y}+\alpha_{ey}T_e\widehat{E_y}\\ Q_{ix}&=\tfrac{3}{2}\Gamma_{ix}T_i-\kappa_{ix}\tfrac{1}{h_x}\tfrac{\partial T_i}{\partial x}\\ Q_{iy}&=\tfrac{3}{2}\Gamma_{iy}T_i-\kappa_{iy}\tfrac{1}{h_y}\tfrac{\partial T_i}{\partial y}\end{aligned} \tag{B.14}$$

where κ and α are thermal conductivity ($\kappa = n\chi$) and the thermo-electric coefficients respectively.

The above transport equations require a set of boundary conditions in order to yield unique solutions.

B.1 Boundary Conditions

For the core-edge boundary, power flows from the core into the SOL. Because the power clearly comes from the core, the sum of the ion and electron energy flux across the core-edge boundary is equal to the sum of the ohmic, and auxiliary and α-particle heating minus the power radiated in the core. The out-flowing core power is usually divided equally between electron and ion channels. To be specific, poloidally integrated power flux is specified together with the requirement of the electron and ion temperatures to be poloidally uniform at the core boundary due to the high parallel thermal conductivity at the high temperature core boundary. The density boundary condition is more uncertain since a substantial amount of fuelling can occur through the edge region. It is customary to fix the density at the core boundary but in this case the particle flux is more or less arbitrary. Thus in this approach, the fixed ion particle flux is set from neutral beam fuelling including the recycling neutral flux. The density is then determined by the transport coefficients. For impurities, zero particle flux is used since the source of these particles is from the wall. A gradient scale-length is specified for the neutral particle flux. For the parallel velocity, a slip condition ($\frac{\partial v_\parallel}{\partial r} = 0$) is used.

For the divertor plates, the boundary conditions are dictated by the sheath[9] formation. The parallel velocity is set to $v_\parallel = c_s$, where $c_s = \left[\left(T_e + T_i\right)/m_i\right]^{1/2}$ is the ion sound speed. The ion and electron temperature conditions are determined by sheath power transmission factors ($\delta_e \approx 5$, $\delta_i \approx 2.5$) where δ_e is a combination of the electron thermal flux (a factor of two for a collisional plasma) and the sheath potential factor ($e\phi_s/T_e \approx 3$). The sheath potential is obtained from the current continuity through a sheath to a conducting wall. In the limit of negligible cross-field drift the sheath potential is given by

$$\phi_s = -\frac{T_e}{e} \ln \left[2\sqrt{\pi} \frac{env_{\parallel i} - J_\parallel}{env_{te}} \right] \tag{B.15}$$

where $v_{te} = (2T_e/m_e)^{1/2}$ is the electron thermal velocity. The neutral flux from the plates are specified as a recycling process with a recycling coefficient, whose value is close to unity for gas saturated surfaces, which is typical for the high particle fluxes conditions, such as divertors and limiters. In the code, the recycling coefficient is set to one. For the impurities, a specified sputtering yield is used.

In regard to the main chamber, specified gradient lengths (of orders of a few centimeters) are used for density and temperatures. For the impurities, a specified

sputtering yield is used and a slip condition ($\frac{\partial v_{\parallel}}{\partial r} = 0$) for the parallel velocity is set. For neutrals, the recycling coefficient is set to one.

For the private flux region, where pumping of neutrals takes place, a pumping rate is specified as a certain fraction of the recycling flux. The other conditions are identical to those in the main chamber.

B.2 Validation of Neutral Diffusion Model

The conventional treatment of neutral transport through a plasma has been done kinetically with Monte Carlo neutral transport codes, such as EIRENE, DEGAS, etc. But this approach inherently involves considerable computational effort and undesirable statistical uncertainty into the solution compared to the simple diffusion model used in this study. The diffusion model is simple enough to allow analysis toward understanding the phenomenon of recycling but not so simplistic as to lose important atomic physics, such as ionization, recombination and charge-exchange processes. The main advantage of the diffusion model comes from the numerical efficiency. The diffusion equation of the neutral transport can be efficiently finite differenced along with the plasma fluid equations and solved numerically in a coupled and self-consistent manner without the excessive computational effort. Nevertheless, for a reasonable description of neutral transport within the fluid diffusion model, several criteria must be satisfied. The particle balance equation with the diffusion model can be casted in a conservative flux form as follows:

$$\frac{\partial n_n}{\partial t} + \nabla \cdot (\Gamma_n) = -S_n \tag{B.16}$$

where the source term from recombination process is negligible compared to ionization ($S_n = n_e n_n K^{ion}$) and where $K^{ion} =< \sigma_{ion} v_e >$ is the ionization rate coefficient. The flux can be derived from Navier-Stokes type momentum equation and given by:

$$\Gamma_{n_n} \approx -\frac{1}{3}\lambda_{tr} \nabla \cdot (n_n u_n) \tag{B.17}$$

where $\lambda_{tr} = u_0/(n_e < \sigma_{ion} v_e > + n_e < \sigma_{cx} v_e >)$ is the mean free path of neutrals from charge-exchange and ionization processes. When the same temperature is assumed for ions and neutrals, u_n is the ion thermal speed and the convective flux is negligible compared to the diffusion flux from the neutral density gradient. Under these conditions, the typical diffusion equation can be derived.

$$\frac{\partial n_n}{\partial t} = \nabla \cdot (D_n \nabla_{n_n}) - S_n \tag{B.18}$$

where $D_n \equiv {u_n}^2/(3 n_e < \sigma v_e >_{tot})$. Also, for the energy equation of the neutrals, the thermal diffusivity is usually assigned the same value as the diffusion coefficients.

For the local diffusion model of neutrals to be valid, the similar conditions as the fluid approximation for electrons and ions are necessary.

$$\lambda_{cx} \ll L_T \tag{B.19}$$

where λ_{cx} is the mean free path of the charge-exchange process between ions and neutrals and L_T is the characteristic scale length of neutral density and temperature. In case of neutrals, the random walk process, which is necessary for the fluid approximation, is driven largely by the charge-exchange process. In a typical plasma condition for the edge region of a tokamak, the above condition is not well justified. Therefore, a special correction for the fluid model is required and the artificial limit of the particle and heat flux is necessary. According to the kinetic theory, the limit of the maximum flux density is given by the one-way Maxwellian random flux density,

$$\Gamma_n^{Max} = \frac{1}{4} n_n \bar{c} = \frac{1}{4} n \left(8kT_n/\pi m_n\right)^{1/2} \tag{B.20}$$

and thereby the corresponding heat flux is limited to $q_n^{Max} = 2kT_n\Gamma_n^{Max}$. To minimize the error of the fluid description, the maximum particle and heat flux is limited artificially to this level in this study.

Appendix C

Fusion Experiment : ASDEX Upgrade

This study is dealt with the divertor tokamak ASDEX Upgrade[57], which is a medium sized device for controlled fusion. In fig C.1, a poloidal view of ASDEX Upgrade is

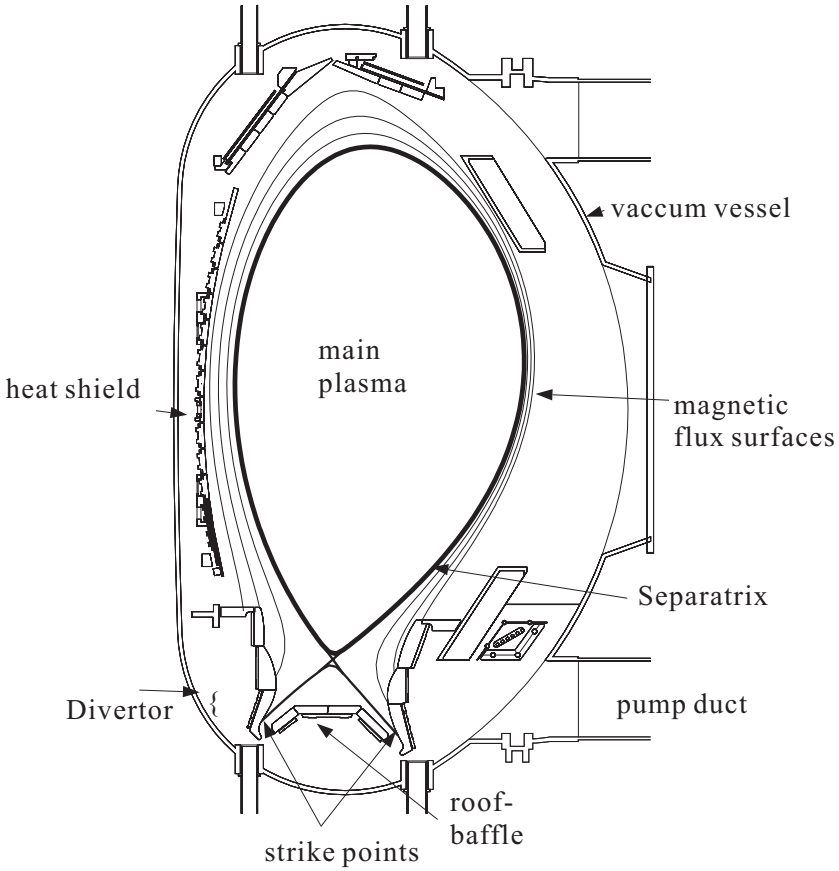

Figure C.1: *A poloidal view of ASDEX Upgrade with the important components described.*

major Radius (Torusradius)	R_0	1.65 m
minor Plasmaradius	a	0.5 m
minor Plasmaradius	b	0.8 m
aspect ratio (R/a)	A	3.3
plasma elongation (b/a)	s	1.6
triangularity	δ	0.4
vessel volume	V_G	32 m^3
plasma volume	V_P	13 m^3
plasma surface area	A_P	42 m^2
total mass of plasma		3.3 mg
maximum magnetic field at the plasma center	$B_{tor,0}$	3.0 T
maximum electric current	I_p	1.4 MA
ohmic heating	P_{OH}	$\leq$1 MW
neutral beam heating	P_{NI}	$\leq$20 MW
ion-cyclotron resonance heating	P_{ICRH}	$\leq$6 MW
electron-cyclotron resonance heating	P_{ECRH}	$\leq$2 MW
discharge duration		$\leq$10 s

Table C.1: *Major plasma parameters and the technical data of ASDEX Upgrade.*

shown with the important components. Major plasma parameters and the technical data are presented in table C.1.

Toroidal magnetic configurations have nested magnetic surfaces, where the plasma pressure and current are constant, as shown in fig 1.3. A magnetic surface is defined by an ergodic magnetic field line which forms a surface through a large number of toroidal and poloidal turns. In this case, a magnetic surface are labelled with a magnetic flux. For this purpose, the normalized poloidal magnetic flux (ρ_{pol}) is defined as follows:

$$\rho_{pol}(R) = \sqrt{\frac{\Psi(R) - \Psi(a)}{\Psi(s) - \Psi(a)}} \tag{C.1}$$

where R is the major radius at the outer midplane ($0 \leq r \leq a$), and a is the minor radius at the outer midplane, and s is the radial position of the separatix. $\Psi(R)$ is defined as:

$$\Psi(R) = \int_0^R \int_0^{2\pi} B_\theta dR d\phi \tag{C.2}$$

where π is the toroidal coordinate and B_θ is the poloidal magnetic field component.

Appendix D

Analytic Formula for the Erosion Rate

The details of analytic description of the erosion rate proposed by Roth[18, 19] is described in this section. This formula is applicable for the bombardment of Hydrogen isotopes on pure graphite and is based on the measurements for the emission of methane.

As discussed on the erosion mechanism in chap 2, The total erosion rate of graphite substrate consists of the physical and the chemical parts.

$$Y_{tot} = Y_{phys} + Y_{therm}(1 + D \cdot Y_{dam}) + Y_{surf} \tag{D.1}$$

The physical sputtering Y_{phys} can be calculated by the revised Bohdansky formula[58]

$$Y_{phys} = Q \cdot S_n(E_0) \left[1 - \left(\frac{E_{th}}{E_0}\right)^{2/3}\right] \left(1 - \frac{E_{th}}{E_0}\right)^2 \tag{D.2}$$

where E_0 is the incident energy of the hydrogen isotopes, and Q and the threshold energy E_{th} are fitting parameters. $S_n(E_0)$ is the nuclear stopping power, which can be approximated[59] by

$$S_n\left(E_0\right) = \frac{0.5 \ln\left[1 + 1.2288\left(E_0/E_{TF}\right)\right]}{E_0/E_{TF} + 0.1728\sqrt{E_0/E_{TF}} + 0.008\left(E_0/E_{TF}\right)^{0.1504}} \tag{D.3}$$

where E_{TF} is the Thomas-Fermi energy.

The thermal desorption of the hydrocarbons Y_{therm} can be determined by

$$Y_{therm} = c^{sp^3} \frac{0.033 \exp\left(-\frac{1.7}{kT}\right)}{2 \times 10^{-32}\Phi + \exp\left(-\frac{1.7}{kT}\right)} \tag{D.4}$$

where T is the substrate temperature, Φ is the particle flux of the incident hydrogen isotopes. The concentration of sp^3 bond c^{sp^3} is estimated by

$$c^{sp^3} = C \frac{\left[2 \times 10^{-32}\Phi + \exp\left(-\frac{1.7}{kT}\right)\right]}{\left\{2 \times 10^{-32}\Phi + \left[1 + \frac{2\times 10^{29}}{\Phi} \exp\left(-\frac{1.8}{kT}\right)\right] \exp\left(-\frac{1.7}{kT}\right)\right\}} \tag{D.5}$$

with the correction factor

$$C = \frac{1}{1 + 1.5 \times 10^{-23}\Phi} \tag{D.6}$$

when the influence of the hydrogenation time of sp^2 is taken into account.

The enhancement of Y_{therm} with the damage production of graphite structure DY_{dam}, which result from bond breaking and carbon displacement in the implanted layer, is

$$Y_{dam} \propto S_n(E_0)\left[1 - \left(\frac{E_{th}}{E_0}\right)^{2/3}\right]\left(1 - \frac{E_{th}}{E_0}\right)^2 \tag{D.7}$$

with the fit parameter D instead of Q, as the same energy dependence as Y_{phys} is applicable.

The surface erosion process of the hydrocarbon radicals on the surface Y_{surf} is quantified as

$$Y_{surf} = c^{sp^3}\frac{Y_{des}}{1 + \exp\left(\frac{E_0 - 65}{40}\right)} \tag{D.8}$$

with Y_{des} is the same formula as Y_{phys} with the replaced threshold energy ${E^*}_{th}$ between the incident ions and sp^3 bond.

Appendix E

The tungsten coating of the central column

The inner heat shield of ASDEX Upgrade was covered with tungsten coated graphite tiles in a step by step approach starting with experimental campaign 1999/2000 (PHASE I). The following description of tungsten coating history is after [60, 61]. There $1.2m^2$ of the low part of the central column were coated by tungsten (before shot number 12712). During PHASE II (campaign April to July 2001), a total tungsten coverage of

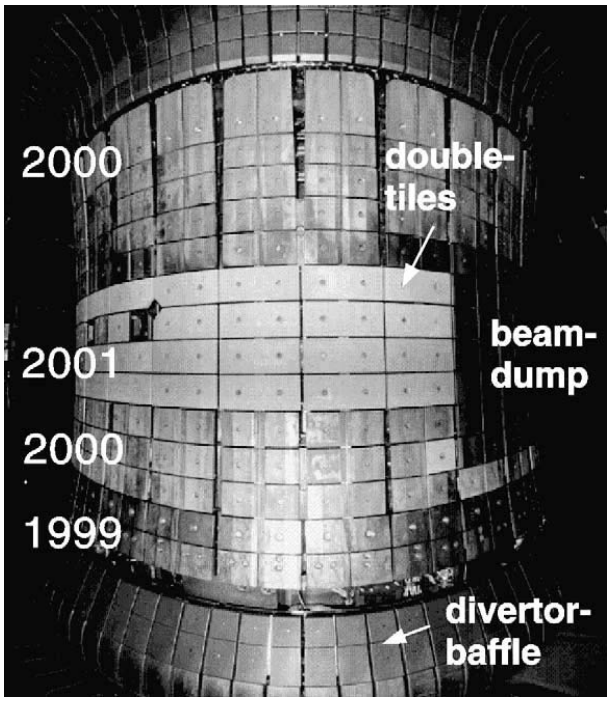

Figure E.1: *The central column of ASDEX Upgrade with the tungsten coated tiles. The four tiles in the equatorial plane are used as a limiter during plasma start-up and in dedicated limiter discharges (after [60]).*

the central column was applied ($6.4m^2$), except for regions, which may be hit directly by the shine through of the neutral beam injection (NBI) or which are used as a limiter. Finally, all the area of inner heat shield ($7.1m^2$) including the limiter region was also coated for the campaign 2001/2002 (PHASE III). In fig E.1, different positions of the W-tiles during PHASE I-III are indicated. In terms of discharge numbers, PHASE I, II, III corresponds to the shotnumbers, from 12860 to 14051 (DIV II), from 14052 to 14610, and from 14611 to date, respectively. The tiles were coated commercially by plasma arc deposition to a thickness of 1 μm. In PHASE III, most of the start-up limiter region (equatorial ring at the central column) is tungsten coated with so called double-tiles (see Fig. E.1). These tiles diminish the number of leading edges and due to an improved mount the evolution of misalignment is reduced. During the campaigns with W-coated central column, almost no negative influence on the plasma performance was found. Only during direct plasma wall contact or for reduced clearance in divertor discharges spectroscopic evidence for tungsten influx could be found.

Bibliography

[1] K Heinloth. *Die Energiefrage: Bedarf und Potentiale, Nutzung, Risiken und Kosten.* Verlag Vieweg, Braunschweig, Wiesbaden, 1997.

[2] J. Ongena and G. V. Oost. Energy for Future Centries. *Trans. Fusion Tech.*, 37:3, 2000.

[3] J. A. Wesson. *Tokamaks.* Clarendon Press, Oxford, 1997.

[4] J. P. Freidberg. *Ideal Magnetohydrodynamics.* Plenum Press, New York and London, 1987.

[5] R. A. Gross. *Fusion Energy.* John Wiley and Sons, 1984.

[6] B. B. Kadomtsev and O. P. Pogutse. Turbulence in toroidal plasmas. *In Review of Plasma Physics*, 5:249.

[7] W. K. Hagan and E. A. Frieman. Nonlinear gyrokinetic theory, the direct interation approximation, and anomalous thermal transport in tokamaks. *Phys. Fluids*, 29.

[8] B. Scott. Low frequency fluid drift turbulence in magnetized plasmas. Technical Report 5/95, IPP, Garching, Germany, 2001.

[9] P. C. Stangeby. *The Plasma Boundary of Magnetic Fusion Devices.* Institute of Physics Publishing, 2000.

[10] A. Kallenbach, R. Dux, V. Mertens, O. Gruber, G. Haas, M. Kaufmann, W. Poschenrieder, F. Ryter, H. Zohm, M. Alexander, K. Behringer, M. Bessenrodt-Weberpals, H.-S. Bosch, K. Büchl, A. R. Field, J. C. Fuchs, O. Gehre, A. Herrmann, S. Hirsch, W. Köppendörfer, K. Lackner, K. F. Mast, G. Neu, J. Neuhauser, S. De Peña Hempel, G. Raupp, K. Schönmann, A. Stäbler, K.-H. Steuer, O. Vollmer, M. Weinlich, W. P. West, T. Zehetbauer, and ASDEX Upgrade Team. H-mode discharges with feedback-controlled radiative boundary in the ASDEX Upgrade tokamak. *Nuclear Fusion*, 35(10):1231–1246, 1995.

[11] G. Federici et al. In-Vessel Tritium Retention and Removal in ITER. *Journal of Nuclear Materials*, 266-269:14 – 29, 1999.

[12] R. Aymar, V. Chuyanov, M. Huguet, Y. Shimomura, and ITER Joint Central Team and Home Teams. Iter-feat the future international burning plasma experiment overview. IAEA-CN-77/ITEROV/1, to appear in Nuclear Fusion.

[13] R. Dux, A. G. Peeters, A. Gude, A. Kallenbach, R. Neu, and ASDEX Upgrade Team. Z dependence of the core impurity transport in ASDEX Upgrade H-Mode discharges. *Nuclear Fusion*, 39(11):1509–1522, 1999.

[14] T. Sunn Pedersen, R.S. Granetz, A.E. Hubbard, I.H. Hutchinson, E.S. Marmar, J.E. Rice, and J. Terry. Radial impurity transport in the h mode transport barrier region in alcator c-mod. *Nuclear Fusion*, 40(10):1795–1804, 2000.

[15] B. Unterberg, H. Knauf, P. Lindner, V. Philipps, A. Pospieszczyk, D. Rusbiildt, U. Samm, B. Schweer, M. Rubel, T. Tanabe, Y. Ueda, and M. Wada. Experimental studies of the link between production and penetration of impurity atoms into the plasma edge and the central impurity content in textor-94. *Journal of Nuclear Materials*, 313-316:116–126, 2003.

[16] S. P. Hirshman and D. J. Sigmar. Neoclassical transport of impurities in tokamak Plasmas. *Nuclear Fusion*, 21(9):1079–1201, 1981.

[17] I. H. Hutchinson. *Principles of Plasma Diagnostics*. Cambridge University Press, 1987.

[18] J. Roth and C. Garcia-Rosales. Analytic Description of the Chemical Erosion of Graphite by Hydrogen Ions. *Nuclear Fusion*, 36(12):1647–1659, 1996.

[19] J. Roth. Chemical erosion of carbon based materials in fusion divices. *Journal of Nuclear Materials*, 266-269:51–57, 1999.

[20] A. Kallenbach, R. Neu, W. Poschenrieder, and ASDEX Upgrade Team. The contribution of chemical erosion to the carbon content in the ASDEX Upgrade tokamak. *Nuclear Fusion*, 34(12):1557–1565, 1994.

[21] F. WAGNER et al. Development of an edge transport barrier at the h-mode transition of asdex upgrade. *Physical Review Letter*, 53:1453, 1984.

[22] W. Suttrop. Physics of edge operational limits and their effect on tokamak confinement. Technical report, Habilitation thesis, Bayreuth University, Germany, 2000.

[23] J. D. Conner. A review of models for elms. *Plasma Physics and Controlled Fusion*, 40:191–213, 1998.

[24] V. Rohde, R. Neu, H. Maier, A. Geier, et al. Operation of ASDEX Upgrade with Tungsten Tiles at the Central Column. In K. Szegő, T. N. Todd, and S. Zoletnik, editors, *Europhysics Conference Abstracts (Proc. of the 24th EPS Conference on Controlled Fusion and Plasma Physics, Budapest, 2000)*, Geneva. EPS.

[25] P.C. Stangeby and J.D. Elder. Radial impurity transport in the h mode transport barrier region in alcator c-mod. *Nuclear Fusion*, 40(10):1795–1804, 2000.

[26] J. Roth, K. Krieger, and G. Fussmann. Divertor retention for recycling impurities. *Nuclear Fusion*, 32(10):1835–1844, 1992.

[27] G. Fußmann. Analytical modeling of impurity transport in toroidal devices. *Nuclear Fusion*, 26(8), 1986.

[28] F. Wagner et al. Development of an edge transport barrier at the h-mode transition of ASDEX. *Physical Review Letters*, 53(15):1453–1456, 1984.

[29] K. Behringer, H. P. Summers, B. Denne, M. Forrest, and M. Stamp. Spectroscopic determination of impurity influx from localized surfaces. *Plasma Physics and Controlled Fusion*, 31:2059–2099, 1989.

[30] A. Geier. Aspekte des verhaltens von wolfram im fusionexperiment asdex upgrade. Technical report, thesis, TU München, Germany, 2001.

[31] T. Pütterich. Messung des verunreinigungsflusses auf den schutzlimitern von asdex upgrade. Technical report, Diplomarbeit, Ausburg Universität, Germany, 2002.

[32] A. Kallenbach, G. Fussmann, H.-M. Mayer, S. Pitcher, and the ASDEX Upgrade Team. The influence of spatially and temporally varying edge conditions on the interpretation of spectroscopic flux measurements. *Plasma Physics and Controlled Fusion*, 36:1299–1306, 1994.

[33] K. Behringer. private communication, 2002.

[34] H. P. Summers. Atomic Data and Analysis Structure. *JET-IR(94)06, Abington, JET Joint Undertaking*, 1994.

[35] A. Kallenbach and H.-M. Mayer. Characteristics of a freely programmable iccd detector for multichord particle influx measurements on the asdex-upgrade tokamak. *Rev. Sci. Instrum.*, 67:1257–1262, 1996.

[36] R. Neu, K. Asmussen, G. Fussmann, P. Geltenbort, G. Janeschitz, K. Schönmann, G. Schramm, U. Schumacher, , and ASDEX Upgrade team. Monitor for the carbon and oxygen impurities in the asdex upgrade tokamak. *Rev. Sci. Instrum.*, 64:1829–1833, 1993.

[37] R. Neu et al. Influence of the Carbon and the Oxygen Concentration on the Density Limit in ASDEX Upgrade. In E. Joffrin, P. Platz, and P. E. Stott, editors, *Europhysics Conference Abstracts (Proc. of the 21th EPS Conference on Controlled Fusion and Plasma Physics, Montpellier, 1994)*, volume 18B, part 1, pages 6–9, Geneva, 1994. EPS.

[38] H. Murman, S. Götsch, H. Röhr, H. Salzmann, and K. H. Steuer. The Thomson scattering systems ot the ASDEX Upgrade tokamak. *Review of Scientific Instruments*, 63(10):4941–4943, October 1992.

[39] J. Neuhauser, D. P. Coster, V. Dose, J. W. Kim, B. Kurzan, H. Murmann, H. Salzmann, R. Schneider, W. Schneider, J. Schweinzer, R. Wunderlich, and ASDEX Upgrade Team. Analysis of High-Resolution ASDEX Upgrade Edge Plasma Profiles. *Europhysics Conference Abstracts (CD-ROM), Proc. of the 26th EPS Conference on Controlled Fusion and Plasma Physics, Maastricht, 1999 , (Ed.) Bastian, C., Nieswand, C. (EPS, Geneva, 1999)*, 23.

[40] V. Dose, J. Neuhauser, B. Kurzan, H. Murmann, H Salzmann, et al. Tokamak edge profile analysis employing bayesian statistics. *Nuclear Fusion*, 41:1671, 2001.

[41] B. J. Braams. Computational studies in tokamak equilibrium and transport. Technical report, thesis, Rijksuniversiteit, Utrecht, Nederland, 1986.

[42] D. Reiter. The eirene code, version: Jan. 92 users manual. Technical report, Technical Report Jül-2599, KFA Jülich, Germany, 1992.

[43] W. Ullrich. Helium transport in asdex upgrade. Technical report, thesis, Ausburg Universität, Germany, 1999.

[44] A. Kallenbach, R. Dux, G. Haas, L. Horton, M. Jakobi, B. Kurzan, H. W. Müller, R. Neu, J. Neuhauser, R. Pugno, T. Pütterich, V. Rohde, W. Sandmann, S.-W. Yoon, and ASDEX Upgrade Team. Edge transport and its interconnection with main chamber recycling in ASDEX Upgrade. In *Proc. of the 19th IAEA Conference, Fusion Energy, Lyon, France, October 2002, (CD-ROM)*, pages IAEA–CN–94/EX/P4–05, Vienna, 2002. IAEA.

[45] J.-W. Kim, D. P. Coster, J. Neuhauser, R. Schneider, and ASDEX Upgrade Team. Asdex upgrade edge transport scaling from the two-dimensional interpretative code b2.5-i. *Journal of Nuclear Materials*, 644:290–293, 2001.

[46] J. W. Kim. An analysis of the anomalous transport of the plasms edge in asdex upgrade. Technical report, thesis, TU München, Germany, 2002.

[47] S. W. Yoon, A. Kallenbach, R. Dux, D. Coster, R. Neu, J. W. Kim, T. Pütterich, R. Pugno, I. Nunes, and ASDEX Upgrade Team. Determination of Edge Transport Coefficients of Plasma Background and Carbon in ASDEX Upgrade using the B2.5 Package. In *9th EU-US Transport Task Force Workshop*, Cordova, Spain, September 9-12, 2002. Session II: ELM PHYSICS AND CONFINEMENT.

[48] F. F. Chen. *Introduction to Plasma Physics and Controlled Fusion*. Plenum Press, New York, 2nd edition, 1984.

[49] G. M. McCracken, R. Barnsley, H. Y. Guo, et al. Studies in jet divertors of varied geometry. iii: Intrinsic impurity behaviour. *Nuclear Fusion*, 39(1):41–60, 1999.

[50] D. G. Whyte, W. P. West, Doerner R., N. H. Brooks, R. C. Isler, G. L. Jackson, G. Porter, M. R. Wade, and Wong C. P. C. Reduction of divertor carbon sources in diii-d. *Journal of Nuclear Materials*, 290-293:356–361, 2001.

[51] R. Neu, K. Asmussen, S. Deschka, A. Thoma, M. Bessenrodt-Weberpals, R. Dux, W. Engelhardt, J. C. Fuchs, J. Gafert, C. García-Rosales, A. Herrmann, K. Krieger, F. Mast, J. Roth, V. Rohde, M. Weinlich, U. Wenzel, ASDEX Upgrade Team, and ASDEX NI Team. The tungsten experiment in ASDEX Upgrade. *Journal of Nuclear Materials*, 241–243:678–683, 1997.

[52] J. Gafert, W. Fundamenski, M. Stamp, and J. D. Strachan. Distribution of Carbon impurity sources between low and high field side measured via Zeeman-Spectroscopy in JET. *In Europhys. Conf. Abstr., European Physical Society*, 25.

[53] I. Nunes, G. D. Conway, M. Manso, M. Maraschek, F. Serra, W. Suttrop, the CFN, and ASDEX Upgrade Team. Study of ELMs on ASDEX Upgrade using Reflectometry Measurements with High Temporal and Spatial Resolution. In E. Joffrin, P. Platz, and P. E. Stott, editors, *Europhysics Conference Abstracts (CD-ROM, Proc. of the 29th EPS Conference on Controlled Fusion and Plasma Physics, Montreux, 2002)*, Geneva, 2002. EPS.

[54] F. Jenko. Particle pinch in collisionless drift-wave turbulence. *Physics of Plasmas*, 7:514, 2000.

[55] S. I. Braginskii. Transport processes in a plasma. *In Review of Plasma Physics*, 1:205–311.

[56] R. Schneider. *Plasma Edge Physics for Tokamaks*. Technical Report 12/1, IPP, Garching, Germany, 2001.

[57] W. Köppendörfer, M. Blaumoser, H. Bruhns, et al. Completion of Assembly and Start of Technical Operation of ASDEX Upgrade. In B.E. Keen, M. Huguet, and R. Hemsworth, editors, *Fusion Technology (Proc. of the 16th Symposium on Fusion Technology, London, U.K., 1990)*, volume 1, pages 208–212, Amsterdam, 1991. Elsevier.

[58] C. Garcia-Rosales. Erosion processes in plasma-wall interactions. *Journal of Nuclear Materials*, 211:202–214, 1994.

[59] W. Eckstein et al. Sputtering data. Technical Report 9/82, IPP, Garching, Germany, 1993.

[60] R. Neu, R. Dux, Geier A., H. Greuner, K. Krieger, H. Maier, R. Pugno, V. Rohde, S. W. Yoon, and ASDEX Upgrade Team. New results from the tungsten programme at asdex upgrade. *Journal of Nuclear Materials*, 211:202–214, 1994.

[61] R. Neu. private communication, 2003.